Adaptive State Prediction for Operating Point Optimization of Agricultural Machine Combinations

Zur Erlangung des akademischen Grades eines

Doktors der Ingenieurwissenschaften (Dr.-Ing.)

von der KIT-Fakultät für Maschinenbau
des Karlsruher Instituts für Technologie (KIT)

angenommene

Dissertation

von

Benjamin Kazenwadel, M.Sc.

Tag der mündlichen Prüfung: 29. Juni 2026
Erster Gutachter: Prof. Dr.-Ing. Marcus Geimer
Zweiter Gutachter: Prof. Dr. Ludger Frerichs

Abstract

With growing demand to reduce greenhouse gas emissions and operating costs, improving process efficiency is becoming increasingly relevant. One path is to optimize the operating points of the machines during use. The challenges are the variety of processes and the complexity of the machine combinations, as tractors are usually paired with various implements. In addition, holistic optimization requires understanding how resource consumption relates to harvest yields, but this relationship becomes known only at the end of the harvest season.

This thesis optimizes agricultural tasks by formulating the problem as a constrained optimization problem. A system-state definition for agricultural machine combinations is defined, and the influences on the machine state are characterized and detected to account for varying operating conditions. Based on this information, possible system states are adaptively predicted during operation. To enable an optimization of the operating point, the presented approach defines process constraints to prevent optimization from negatively affecting harvest yield, which is not directly observable during operation. These constraints allow for the formulation of explicit objective functions that can be observed and optimized during operation.

The prediction method is validated across multiple tractor-cultivator combinations, and the resulting prediction accuracy is analyzed. The optimization approach is applied to maximize energy efficiency by adapting the operating speed and engine rotations during the tillage process. The results show that an optimization based on a prediction of advantageous operating points is a promising approach to increasing the efficiency of agricultural operations.

***Keywords*:** State Prediction, Constrained Optimization, Adaptive Modeling, Interoperability, Tillage

Kurzfassung

Adaptive Zustandsprognose zur Betriebspunktoptimierung landwirtschaftlicher Maschinenkombinationen

Angesichts der steigenden Anforderungen an die Reduzierung der Treibhausgasemissionen und der Betriebskosten von Landmaschinen gewinnt die Verbesserung der Prozesseffizienz zunehmend an Bedeutung. Eine Möglichkeit besteht darin, die Betriebspunkte der Maschinen während des Einsatzes zu optimieren. Diese Aufgabe ist aufgrund der Vielfalt der Prozesse und der Komplexität der Maschinenkombinationen eine Herausforderung, da bei der Feldarbeit Traktoren in Kombination mit den verschiedensten Anbaugeräten eingesetzt werden. Darüber hinaus erfordert eine ganzheitliche Optimierung Kenntnisse über den Zusammenhang zwischen Ressourcenverbrauch und Ernteerträgen, wobei Letztere erst am Ende einer Erntesaison bekannt werden.

Diese Arbeit optimiert landwirtschaftliche Prozesse, indem sie die Problemstellung als beschränktes Optimierungsproblem formuliert. Eine Zustandsbeschreibung für landwirtschaftliche Maschinenkombinationen wird definiert, und die Einflüsse auf den Maschinenzustand werden charakterisiert und erkannt, um unterschiedliche Betriebsbedingungen zu berücksichtigen. Auf dieser Grundlage werden mögliche Systemzustände während des Betriebs adaptiv vorhergesagt. Um eine direkte Optimierung des Betriebspunkts zu ermöglichen, definiert der vorgestellte Ansatz Prozessbeschränkungen, um zu verhindern, dass sich die Optimierung negativ auf den Ernteertrag auswirkt. Diese Beschränkungen ermöglichen die Formulierung expliziter Zielfunktionen, die während des Betriebs beobachtet und optimiert werden können.

Um den praktischen Nutzen des vorgeschlagenen Ansatzes zu demonstrieren, wird die Vorhersagemethode für mehrere Traktor-Grubber-Kombinationen validiert und die daraus resultierende Vorhersagegenauigkeit analysiert. Der

Optimierungsansatz wird auf die Maximierung der Energieeffizienz durch Anpassung der Arbeitsgeschwindigkeit und der Motordrehzahl während des Bodenbearbeitungsprozesses angewendet. Die Ergebnisse zeigen, dass eine Optimierung auf der Grundlage einer Vorhersage vorteilhafter Betriebspunkte ein vielversprechender Ansatz zur Steigerung der Effizienz landwirtschaftlicher Maschinenkombinationen ist.

***Schlagworte*:** Zustandsprognose, Beschränkte Optimierung, Adaptive Modellierung, Interoperabilität, Bodenbearbeitung

Danksagung

Diese Arbeit entstand während meiner Tätigkeit als wissenschaftlicher Mitarbeiter und Doktorand am Institutsteil Mobile Arbeitsmaschinen (Mobima) des Karlsruher Instituts für Technologie (KIT). Ich möchte mich herzlich bei den Menschen bedanken, die mich in diesem Zeitraum fachlich und persönlich unterstützt haben.

Mein besonderer Dank gilt Prof. Dr.-Ing. Marcus Geimer für die Betreuung dieser Arbeit als Doktorvater sowie für die Übernahme des Hauptreferats. Seine wissenschaftliche Unterstützung sowie der gewährte Freiraum haben maßgeblich zum Gelingen dieser Arbeit beigetragen. Ebenfalls danke ich Prof. Dr. Ludger Frerichs, Leiter des Instituts für Mobile Maschinen und Nutzfahrzeuge der Technischen Universität Braunschweig, für die Übernahme des Korreferats. Prof. Dr.-Ing. Jürgen Fleischer, Leiter des Instituts für Produktionstechnik am KIT, danke ich für die Übernahme des Prüfungsvorsitzes.

Meinen Kolleginnen und Kollegen am Mobima danke ich herzlich für die Unterstützung sowie für den fachlichen wie auch den persönlichen Austausch, sowohl im Arbeitsalltag als auch "drumherum". Besonders danken möchte ich Marina Graf und Lukas Michiels für die anregenden Diskussionen im Büro 019 sowie bei gemeinsamen Konferenzbesuchen. Ein weiterer Dank gilt den wissenschaftlichen Hilfskräften sowie den Studierenden, die die Forschungsarbeiten im Rahmen ihrer Abschlussarbeiten unterstützt haben. Die Zusammenarbeit war für mich stets lehrreich und von großem Wert.

Meinen Projektpartnern bei den Firmen AGCO und LEMKEN, insbesondere Dr. Franz Fuchshumer, Lukas Icking und Stefan Haverkamp, danke ich für die wertvolle, vertrauensvolle und stets konstruktive Zusammenarbeit. Ebenso gilt mein Dank den Testfahrern für die Durchführung der Messfahrten sowie den Landwirten, die hierfür ihre Flächen zur Verfügung gestellt haben.

Ein besonderer Dank gilt meinen Eltern und meiner Familie für ihre Unterstützung während meines Studiums und meiner Promotion. Ohne ihren

Rückhalt wäre all dies nicht möglich gewesen. Von Herzen danke ich insbesondere meiner Partnerin Isabela, die mich beim Verfassen dieser Arbeit stets vor dem Verzweifeln bewahrt hat und mir die notwendige Motivation gab, weiterzumachen.

Karlsruhe, im Juli 2026 *Benjamin Kazenwadel*

Contents

Abstract i

Kurzfassung iii

Abbreviations and Symbols ix

1 Introduction 1

2 State of Research 5
2.1 Fundamentals 5
2.1.1 Agricultural Machinery 5
2.1.2 Interfaces and Standards 7
2.1.3 Soil Mechanics 9
2.1.4 Artificial Neural Networks 15
2.2 Related Work 21
2.2.1 Process Quality 24
2.2.2 Efficiency 24
2.2.3 Combining Efficiency and Process Quality 26
2.3 Research Approach 27

3 State Prediction and Optimization 29
3.1 State Description 29
3.2 State Prediction 32
3.2.1 Process Load Prediction 36
3.2.2 Drivetrain Prediction 41
3.3 Process Optimization 46

4 Experiments 53
4.1 Experiment Setup 53
4.1.1 Machine Description and Setup 53
4.1.2 Software Setup 56

4.2 Experiment Design 60
4.2.1 Prediction Accuracy Analysis 61
4.2.2 Process Load Model Validation 63
4.2.3 Drivetrain Model Validation 64
4.2.4 Optimization Analysis 65
4.3 Data Processing 68
4.3.1 Process Load Model Parametrization 70
4.3.2 Drivetrain Model Parametrization 74

5 Results 77
5.1 Prediction Accuracy Analysis 77
5.1.1 Process Load Model 80
5.1.2 Drivetrain Model 87
5.1.3 Combined Process Load and Drivetrain Model 90
5.2 Process Load Model Validation 92
5.3 Drivetrain Model Validation 95
5.4 Impact of Prediction Accuracy on Optimization 96
5.5 Optimization Analysis 97

6 Summary 101
6.1 Scientific Contribution 102
6.2 Continuing Approaches 103

A Appendix 105
A.1 Figures 105
A.2 Tables 109

List of Figures 111

List of Tables 115

Bibliography 117
Own Publications 128

Abbreviations and Symbols

Mathematical Notations

Scalar	Lower- and Uppercase Letters: a, A
Vector	Letters with Arrow Overline: $\vec{a}, \vec{B}$

Acronyms

AEF	Agricultural Industry Electronics Foundation
ANN	Artificial Neural Network
ASABE	American Society of Agricultural and Biological Engineers
ASAE	American Society of Agricultural Engineers
CAN	Controller Area Network
DLG	Deutsche Landwirtschafts-Gesellschaft
LSTM	Long Short-Term Memory
MAE	Mean Absolute Error
MAPE	Mean Absolute Percentage Error
PCA	Principal Component Analysis
SAE	Society of Automotive Engineers
TECU	Tractor ECU
TIM	Tractor-Implement-Management System
VDMA	Verband Deutscher Maschinen- und Anlagenbau e.V.

Latin Symbols

B	Fuel Rate	l/h
C_i	Cost Factor	-
c_s	Situational Parameter	-

d	Working Width	m
F	Force	N
F_{D}	Draft Force	N
F_{G}	Wheel Load	N
F_{T}	Tractive Force	N
g	Gravitational Acceleration	$\mathrm{m/s^2}$
h	Objective Function	-
h^*	Observable Objective Function	-
h_{fuel}	Productivity concerning Fuel Input	ha/l
h_{money}	Productivity concerning Monetary Input	ha/€
h_{time}	Productivity concerning Time Input	ha/h
m	Mass	kg
n	Rotational Speed	1/s
p	Process Parameter	-
s	Travel Reduction (Slip)	-
$\vec{s}$	State Vector	-
T	Torque	N m
t	Working Depth	m
$\vec{u}$	Conditional Input	-
v	Operating Speed	km/h
v_{theo}	Theoretical Speed	km/h
x	Spatial Coordinate	m
$\vec{x}$	Prediction Input	-
y	Spatial Coordinate	m
$\vec{y}$	Prediction Output	-
z	Spatial Coordinate	m
$\vec{z}$	Latent Representation	-

Greek Symbols

β	Pitch Angle	°
δ	Slope Angle	°
ϵ	Environment Parameter	-

γ	Direction	$^\circ$
κ	Traction Coefficient	-
μ_{eq}	Equality Constraint	-
μ_{ineq}	Inequality Constraint	-
ω	Angular Velocity	rad/s
$\vec{\omega}$	Controllable Variables	-
ϕ	Encoding Network	-
ψ	Decoding Network	-
σ	Standard Deviation	-
$\vec{\tau}$	Interface Variables	-
$\vec{\theta}$	Internal Variables	-
ζ	Harvest Yield Constant	yield/ha

Sub- and Superscripts

$(\cdot)_0$	Initial Value
$(\cdot)_i$	Index
$(\cdot)_j$	Index
$\hat{(\cdot)}$	Predicted Variable
$\tilde{(\cdot)}$	Filtered Variable
$(\cdot)_{\text{pl}}$	Process Load
$(\cdot)_{\text{dt}}$	Drivetrain

1 Introduction

Efficient usage of agricultural machinery is a central objective in farming practices. Machine efficiency plays a vital role in maintaining profitability and sustainability. Farmers and machine manufacturers are seeking new ways to optimize the design and usage of their machinery.

Agricultural fieldwork is energy-intensive. The use of large machinery primarily powered by diesel combustion engines leads to substantial fuel consumption [1]. With rising fuel prices, efficiency is directly linked to operating costs, putting farmers under increasing financial pressure. Alternatives to the combustion engine have not yet become established, particularly in fieldwork, due to the high energy demand and the lower energy density of other technologies [2]. The use of diesel also affects subsequent greenhouse gas emissions, a point highlighted by the current legal framework. The EU's climate targets for the coming years clearly emphasize the need to reduce greenhouse gas emissions. By 2030, greenhouse gas emissions are to be reduced by 55 % compared to 1990 levels, and by 2050, the economy as a whole is to emit net-zero emissions [3]. In Germany, these targets are implemented through national limits, aiming for reductions of at least 65 percent by 2030 and 88 percent by 2040. Greenhouse gas neutrality is to be achieved by 2045, and negative emissions are to be achieved by 2050 [4].

Increasing efficiency can significantly contribute to lower operating costs and reduce greenhouse gas emissions. Common practices include optimizing machine design and developing optimized control algorithms, such as those used to set the optimal gear ratio in the transmission. Steering control in modern machines is also highly automated, thanks to lane guidance systems that enable automatic steering. Nevertheless, some tasks require an operator. For example, the operator currently specifies the target values for longitudinal control in the form of speed specifications to the internal control units. This decision is made based on human perception of the work and individual process objectives. By adapting the control set points, efficiency can be

further optimized. However, directly optimizing these settings for efficiency conflicts with other process objectives, such as process quality. Understanding the impact of a potential adjustment to the control input on efficiency can be the first step toward simplifying this optimization problem.

During the production cycle, several operations are conducted regularly. The task requirements vary depending on the soil and location, the previous crops, and the crop to be planted. Depending on the conditions, different work steps can be carried out to ensure optimal plant growth. The tasks carried out during the production cycle can be categorized as follows [5]:

- Tillage
- Sowing
- Fertilization
- Application of Plant Protection Products
- Harvesting

The extent to which the respective process steps are carried out depends heavily on the crop and cultivation style. The machines used to conduct each process have individual characteristics, not only in terms of efficiency but also in other objectives, such as the process quality. To cope with this wide variety of machine combinations, the characteristics of each implement and tractor must be considered when selecting an appropriate operating point.

This work addresses this complexity by presenting a modular method for predicting possible system states of tractor-implement combinations. This allows for an evaluation of the effects of a change in operating point on the machine's efficiency. The information serves as a basis for informed decision-making, enabling the operator to focus on additional objectives that must also be met to complete the task. An example is the observation of process quality, which is not yet fully automated or optimized for each task in the production cycle. Until automatic monitoring systems are available for all relevant process objectives, the work presents a constraint-based optimization approach that can already automatically optimize efficiency by preventing adverse impacts on other process objectives.

The following work is structured into six chapters.

Chapter 2 analyzes the available literature on the topic. Initially, the fundamentals are discussed, including soil mechanics, and a key background on artificial neural networks. This is followed by a description of the agricultural machinery currently used in the industry, along with the relevant interfaces

for interoperability between tractors and various implements. Related work on modeling the power flow along the drivetrain and process optimization approaches is described. Afterwards, the research gap is identified, and the corresponding research hypothesis and research questions for this work are formulated.

Chapter 3 presents the method for predicting possible operating states and using them for optimization. First, an approach to describe the state of tractor-implement combinations is presented, followed by the systematic steps for predicting possible states based on measuring the current state of the system. Finally, the background to the fieldwork optimization is described. An approach is presented to adapt the optimization space to account for process boundary conditions, thereby avoiding adverse effects on unobservable objective functions.

Chapter 4 presents an exemplary application of the method to agricultural tillage tasks. First, the experimental and data-collection setups are detailed, followed by experiments evaluating the prediction accuracy of the implement and tractor models. Additional experiments to validate the models' transferability to other operating conditions and machine combinations are described. The chapter concludes with the experiment used to validate the constraint-optimization approach.

Chapter 5 presents the results of the experiments. The chapter is structured the same way as the experiments' description. First, the prediction results for the two models are presented, followed by the transferability analysis. At last, the results of the optimization approach are presented.

The summary, scientific contribution, and ongoing approaches conclude this work in Chapter 6.

Parts of this work have already been published in [120], [122], [123], [125] and [129].

2 State of Research

The following describes the scientific fundamentals and related research. Based on this, the research gap is pointed out, and a research hypothesis is formulated.

2.1 Fundamentals

The following presents the fundamentals for this work. First, the machinery used to perform the various processes throughout the production cycle is described, along with the standardized interfaces for power and information exchange. Then, focusing on tillage tasks, the mechanical principles governing the interaction between tools or tires and the soil are presented. This is followed by an introduction to neural networks, which are central to this work.

2.1.1 Agricultural Machinery

This section describes the machines used to perform tasks in agricultural fieldwork. Various machines can conduct each task during the production cycle. Specialized self-propelled vehicles are available for some tasks, such as applying plant protection products and harvesting operations. However, most processes use a specialized implement, along with a tractor that provides the necessary power and a workspace for the machine operator. This combination has the advantage that the respective implement does not require an independent primary power supply.

The process steps in the cultivation cycle are carried out in practice using a wide range of implements. This can be illustrated by the number of process steps carried out between harvesting and sowing alone. Depending on the extent of soil cultivation, the first step involves primary soil cultivation with

a plough or other soil loosening equipment, followed by seedbed preparation and then sowing. For the individual process steps, either specialized implements can be used or combinations such as a power harrow for seedbed preparation combined with a seed drill. In other cultivation approaches, the soil loosening step is omitted, and in some cases, even tillage is omitted altogether through direct sowing. The wide variety of farming approaches has led to the development of numerous, more or less specialized implements. These implements differ not only in their functionality but also in their design. For example, implements can be designed to be mounted directly on the rear power lift of the tractor, or to feature additional wheels for transport, as in semi-mounted implements. [5]

The power supply for the various implements is usually provided by a tractor. Diesel-powered tractors are still widely used for agricultural fieldwork [2]. However, more and more alternative energy sources are now being utilized, each with specific characteristics. These options include methane-powered combustion engines [6], battery-electric power supply [7], as well as the usage of hydrogen in a fuel cell [8].

The choice of energy supply influences the drive-train topology. Beneath classical power-shift gearboxes, continuous variable transmissions (CVT) provide seamless gear ratio changes without power drops. These transmissions usually use power-split configurations in various implementations. The drivetrain's structure significantly influences efficiency and optimal operating points. These power-split transmissions commonly use a mechanical-hydraulic power split. An example of a mechanical-hydraulic power-split transmission is the Fendt Vario CVT. The output-coupled design allows continuous adjustment of the gear ratio within each of the two shiftable speed groups. [9], [10]

Power-split transmission architectures are not limited to coupling the hydraulic and mechanical domains. They can also be implemented electrically and mechanically, as in John Deere eAutoPowr transmissions. This type of transmission offers the advantage that the electric power supply to external consumers can be directly accounted for in the transmission design. [6]

Alongside the ongoing development of tractor drivetrains, modern tractors are equipped with a wide range of control systems. One example of this is the optimization of the transmission control system, which ensures that the machine's internal control parameters are optimally aligned with the

driver-specified control parameters. With these systems, the rear ratio is automatically adapted to advantageous operating points.

W. J. Chancellor *et al.* developed a basic control scheme for adapting the transmission ratio and the engine speed in a standard shifted tractor to reduce fuel consumption. He observed a reduction of fuel consumption of 5-12 % compared to a good operator by applying the control scheme. [11]

M. Schrock *et al.* predicted the fuel rate for different gear settings as a driver aid for selecting the optimal gear. The prediction was based on empirical equations and performed on microchips. [12]

These automated transmission controls are a standard feature in today's continuous variable transmissions and can enhance the efficiency of the machine setup while eliminating the need for the driver to adjust transmission settings manually. [9]

In summary, the drivetrains used in modern agricultural machinery vary significantly in design, complexity, and degree of automation.

2.1.2 Interfaces and Standards

The tractor supplies the required energy to the implements. Therefore, several interfaces are available to mount implements to tractors and establish power transfer and communication between them. The following first describes the physical interfaces, followed by the currently available data exchange interfaces between the tractor and the implements.

Physical Interfaces Standardized interfaces on tractors provide the required power for the implement. Table 2.1 gives an overview of the standardized interfaces for power exchange.

The overview does neither include pneumatic interfaces, primarily used for braking systems and tire inflation control, nor specialized hydraulic interfaces for braking power transmission. As shown in the Table, there is a wide variety of interfaces for mechanically connecting implements and transmitting power via mechanical, hydrostatic, and electrical connections. This variety of connectivity options provides a high level of flexibility for attaching implements to the tractor. Therefore, the implements themselves do not require

Table 2.1: Standardized tractor implement interfaces for power transfer [9], [13]–[15].

Mechanic	
3-point hitch	ISO 730
Front 3-point hitch	ISO 8759-4
Hitch hook	ISO 6489-1
Clevis 40 coupler	ISO 6489-2
Drawbar	ISO 6489-3
Piton fix	ISO 6489-4
Clevis, non-swiveling	ISO 6489-5
80 mm ball	ISO 24347
Rear PTO	ISO 500
Front PTO	ISO 8759-3
Hydrostatic	
Standard quick-action couplings	ISO 10448, ISO 5675, ISO 16028
Power-beyond couplings	ISO 17567
Electric	
7-pole connector 12 V	ISO 1724
ISOBUS 12 V connector	ISO 11783
High-power interface 700 V DC / 400 V AC	ISO 23316

separate power supplies, and features such as an ergonomic workstation are only necessary on the tractor itself.

Data Interfaces With the rise of digitization in agricultural machinery, the objective to enable data transmission between tractors and implements became coherent [16]. The ISOBUS standard (ISO 11783) simplified and standardized data exchange between tractors and implements. The J1939-based communication standard allows the sensor data exchange between tractors and implements. Furthermore, graphical interfaces from implements can be loaded onto the standard tractor terminal using the specified exchange interface. The standard also includes a hardware interface for connecting different modules. [17]

The supported messages can vary across machines depending on the internal tractor ECU (TECU) class. TECU Class 1 devices provide only basic tractor

internal measurements, whereas Class 2 devices additionally support speed, direction, and rear draft information. Class 3 devices support control messages from the implement to the tractor in addition to the provided signals for information and sensor data exchange. [18]

TECU Class 3 features are commonly known as the Tractor-Implement-Management System (TIM), which specifies the functionality that the implement controls the tractor for process-specific controls. Applications include the operating speed control during the baling process and the automation of the tillage process. [19]–[21]

The VDMA Fachverband Landtechnik hosts a database of interchangeable information via ISOBUS. The database includes transmittable parameters via ISOBUS, in accordance with the underlying J1939 protocol. In addition to signals for information and sensor data exchange, control messages from the implement to the tractor are specified [22]. The ISOBUS Data Dictionary [22] contains a specified signal list for data exchange between tractor and implements. The availability of these signals depends on the manufacturer and the TECU version. Therefore, these signals are not available in all machines [23].

In response to the rise of these data-exchange technologies and the resulting complexity, the Agricultural Industry Electronics Foundation (AEF) was founded. The AEF ISOBUS database lists the respective features of each certified component, including the data that can be requested from the TECU according to ISO 11783-9 [24]. It provides information on the compatibility of various ISOBUS- and TIM-certified devices for users, dealers, service personnel, and manufacturers. [23]

2.1.3 Soil Mechanics

Interactions with the environment play a major role in the various steps of the agricultural process chain. Among these, the interaction between the machine and the soil is particularly important. The specific characteristics of this interaction significantly impact power demand, especially during tillage tasks, and are therefore crucial to the process's efficiency.

During tillage, soil structures are broken up, and the soil is mixed or turned. Here, two primary influences of the soil can be observed: friction, which causes a portion of the shear strength to be proportional to the pressure at the

point of interaction, and cohesion, which affects the shear strength. The total material strength can be described by combining these effects. The resistance of the soil results in a draft force demand and is influenced by the respective properties of the two effects and by the type of interaction with the soil. These types can be classified as cutting, pulling, or shearing, with each operation exhibiting a specific resistance. [25]

Many early attempts have been made to describe breaking and mixing soil. The influence of the soil type and moisture was detected early. Some researchers investigated the forces on the individual engaging tools of the implement [26], [27].

Gorjatschkin's rational formula provided one of the earliest scientific approaches to mathematically correlating the draft force demand with operating speed during plowing. He determined that the operating speed v significantly impacts the draft force demand F_D required to operate the implement. This relationship is shown in Equation 2.1. [28]

$$F_\mathrm{D} = c \cdot v^2 \tag{2.1}$$

The equation yields a quadratic increase in force demand with increased operating speed. The parameter c describes the influence of the operating conditions.
Harrigan *et al.* researched the power demand of different implements and came up with an equation that includes a single soil-specific parameter c_soil, along with the working width d and depth t [29]. The American Society of Agricultural and Biological Engineers (ASABE), formerly the American Society of Agricultural Engineers (ASAE), consolidated these findings into the unified standard ASAE D497.7 as presented in Equation (2.2). The standard includes parameter sets for the implement-specific parameters a_0, a_1, and a_2 for various implements. [30]

$$F_\mathrm{D} = c_\mathrm{soil} \cdot d \cdot t \cdot (a_0 + a_1 \cdot v + a_2 \cdot v^2) \tag{2.2}$$

For cultivators, a linear increase in draft force with operating speed ($a_2 = 0$) is proposed, whereas a quadratic increase is proposed for plows ($a_1 = 0$). [30]

Hank *et al.* researched whether draft forces at constant operating speeds can be used as a parameter to describe soil behavior. They concluded that a

constant operating speed is required to observe changes in soil behavior, given the relationship between draft forces and changes in operating speed. [31]

Schutte researched whether draft force measurements can be used to detect changes in soil parameters. He used the relationship to filter draft data and to predict different soil types from geographically mapped force measurements of a cultivator. He concluded that there is a strong spatial correlation in draft force measurements in the field. These spatial correlations can be attributed to changes in environmental conditions. [32], [33]

Rösler et al. investigated various implements to convert available power demand models into online parameterizable formats. The influential factors on the draft and torque demand were thereby categorized into operating parameters, equipment parameters, and soil parameters. The cultivator was among the investigated implements, as determined by Equation (2.2). They derived Equation 2.3, which includes the parameter q, derived from the implement parameter set in ASAE D497.4, and a single parameter c_s that can be identified by measuring the other contained parameters. [34], [35]

$$F_{\mathrm{D}} = c_s \cdot t^2 \cdot (q + v) \tag{2.3}$$

Bögel researched the possibility of adapting the geometry of tillage tools to increase the overall process efficiency. He established a quadratic relationship between the working depth and the required draft force in his experiments. He also demonstrated that specific tool parameters significantly affect the required draft force and the resulting work outcome. A quadratic increase in draft force with increasing operating speed could not be determined. He concluded that adaptable equipment geometries could be used to react to changes in environmental conditions. [36]

The forces required to move implements are often provided by tires. Hereby, soil-specific effects occur during the interaction between the tires and the soil. The characteristic can be described when looking at the forces acting on a single tire, as in Figure 2.1.

In the stationary case, the horizontal and vertical tire forces ($F_{\mathrm{soil},h}$ and $F_{\mathrm{soil},v}$) and ground forces (F_{T} and F_{G}) respectively yield an equilibrium.

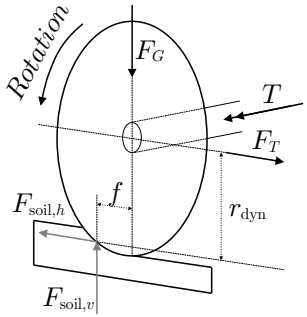

Figure 2.1: Illustrations of the forces acting on a tire (inspired by [10], [37]).

$$F_{\text{T}} = F_{\text{soil},h} \tag{2.4}$$

$$F_{\text{G}} = F_{\text{soil},v} \tag{2.5}$$

The input wheel torque results in a torque equilibrium between the horizontal and vertical forces acting on the tire with the respective lever arms r_{dyn} and f.

$$T = F_{\text{T}} \cdot r_{\text{dyn}} + F_{\text{G}} \cdot f \tag{2.6}$$

Several coefficients are commonly used to describe the traction behavior. The traction coefficient κ describes the relationship between the traction force F_{T}, and the wheel load F_{G} [10].

$$\kappa = \frac{F_{\text{T}}}{F_{\text{G}}} \tag{2.7}$$

Another fundamental criterion for the description of the tractive behaviour is the definition of the dynamic wheel radius r_{dyn}. This parameter is required to calculate the slip rate. Given a deformable ground and a deformable tire, this parameter cannot be measured directly but must be determined using a zero-slip definition. Several possible definitions are available in the literature [10],

[38]. Given a dynamic wheel radius, the theoretical distance traveled by a single rotation of the wheel l_0 can be calculated.

$$l_0 = 2 \cdot \pi \cdot r_{\text{dyn}} \tag{2.8}$$

Based on this value, the longitudinal slip (s) is defined as follows by the relationship between the theoretical distance travelled l_0 and the actual distance l.

$$s = \frac{l_0 - l}{l_0} \tag{2.9}$$

Given a dynamic radius, the theoretical speed v_{theo} of the wheel can be calculated using the rotational speed of the drive shaft. Therefore, the slip rate can also be expressed as the ratio of the theoretical speed to the operating speed v, which is typically derived from radar or GNSS measurements.

$$s = \frac{v_{\text{theo}} - v}{v_{\text{theo}}} \tag{2.10}$$

Traction characteristics significantly impact the efficiency of agricultural machinery. Numerous studies have investigated tire behavior. These studies include the modeling for simulations and simpler models for traction prediction and control, for universal usage as well as specifically for the agricultural context.

Pacejkas *Magic Formula* allows modeling various traction settings. The four customizable parameters in the model affect the curve's shape and must be parametrized for the model to be used. [39]

Kobelski *et al.* used an adaptive unscented Kalman filter to extract information about ground conditions and map them using a modification of Pacejka's traction model. A simulation shows that traction characteristics can be identified and mapped using the proposed approach. [40]

Some traction models are designed for deformable surfaces, such as in an agricultural setting.

Bekker researched the traction characteristics for vehicles driving on deformable soil and derived the first traction prediction models. [41], [42]

Schreiber *et al.*'s model assumes that the traction behavior can be represented by four parameters that describe the tire and the soil characteristics [38]. In [43] and [44], a method for parameterizing these equations was proposed with respective parameter sets for a tire on different soil types.

Meiners *et al.* conducted further experiments on the topic and developed empirical correction factors for the representation of modern tires within the model. [45]

Wismer *et al.* published a mathematical model for predicting the soil-tire interaction. The model relates the traction characteristics to the penetration resistance of the soil as defined in ASAE S313 [46]–[48]. Brixius revised and modified these equations for a better prediction accuracy [49].

Al-Hamed *et al.* incorporated these findings into a program to simulate the traction performance of different machine setups. For radial tires, they suggest using the mean values of the ranges presented by Brixius. [50]

Zoz *et al.* conducted further experiments for radial tires and received new coefficients for radial tires. [51]

Dwyer researched traction characteristics of tires and simplified modeling equations. He concluded that unquantifiable parameters, such as rubber compound and tread type, have a greater impact on traction performance than tire dimensions and deflection. He raised the question of whether these parameters must necessarily be taken into account in traction modeling, or whether a simple model might suffice. For non-deformable surfaces, consequently, he proposes formula (2.11). [52]

$$\kappa = 1 - e^{-20 \cdot s} \tag{2.11}$$

These models describe traction characteristics by relating the traction coefficient κ to the slip rate s. As described in section 2.1, the traction coefficient κ requires a specification of the wheel load.

For wheels with independent suspension, the wheel load can be calculated from the suspension forces [53]. However, the rear axle is often installed without suspension, making this calculation method unfeasible for most standard tractors.

Research has been conducted to develop sensors to measure this load directly. Peeters researched the development of an integrated wheel load sensor for

rigid axles [54]. These sensors are not yet available on most tractors, making it more challenging to assess traction effects.

In a standard tractor, the rear wheels pass over soil previously compacted by the front wheels. The compression caused by the first interaction with soft surfaces affects the traction characteristics of subsequent passes, changing tractive performance. [9]

James H. Taylor *et al.* found that there is a significant difference in pull ratio and tractive efficiency during sequential passes of tires on the same soil. [55]

Holm researched the multipass behavior of tires of equal sizes. In his studies, he determined that multi-axle vehicles are advantageous on deformable soils [56]. Furthermore, he concluded that the multipass effect can be described by the traction coefficients and rolling resistances of the subsequent passes. His research was conducted on tires of equal size. [57]

Another commonly used assumption relates the traction coefficients of subsequent passes directly to the respective traction coefficients. [9]

2.1.4 Artificial Neural Networks

Artificial neural networks (ANNs) can describe various complex systems and relationships. In the agricultural sector, these networks are used for image classification tasks, including plant classification, as well as for growth and yield prediction. [58], [59]

The basic idea behind ANNs is the structure of the human brain. Artificial neurons hereby reproduce the individual synapses. Figure 2.2 visualizes a single artificial neuron.

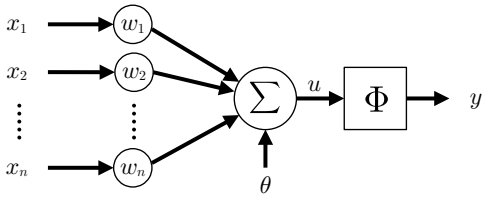

Figure 2.2: Visualization of an artificial neuron (inspired by [60]).

The neuron processes the input values x_i by multiplying them each by a weight w_i and summing them up. The bias θ allows the addition of an independent offset to the summed-up inputs. This calculation principle is shown in Equation (2.12).

$$u = \sum_{i=0}^{n} (x_i \cdot w_i) + \theta \tag{2.12}$$

To include the possibility of representing nonlinear functions, activation functions Φ are used on the combined inputs. Frequently used functions include the sigmoid function and the ReLU function. [60]

Arranging multiple neurons in patterns can replicate various nonlinear functions, provided that the weights and biases of each neuron are defined. The specific method of computing these adjustable parameters enables ANNs to have a wide range of applications. This process is referred to as learning or training. During training, each trainable parameter is optimized according to its influence on the overall prediction error. A commonly used method for this is gradient descent, where the weights are updated based on the gradient of the prediction error. The gradient of the error is typically computed by propagating the prediction loss of the overall network backward through the network to determine the influence of each parameter on the overall error. By iteratively adapting the parameters, the loss is reduced. [60], [61]

The key component in the training process is, therefore, defining a loss function L. This function calculates the network's prediction error, e.g., the difference between the predicted value $\hat{y}$ and the actual value from the training dataset y. An example of such a loss function is the mean absolute error (MAE), as defined in equation (2.13). Here, the absolute difference between the prediction $\hat{y}$ and the ground truth y is evaluated.

$$L_{\text{MAE}} = \frac{1}{n} \sum_{i=1}^{n} ||y - \hat{y}|| \tag{2.13}$$

The loss function can also be applied to batches of input data.

Several methods are applied during the training of neural networks to enhance prediction performance. The relevant principles are outlined below.

Removing Scaling Effects ANNs are affected by the scaling of the respective input signals. This is particularly important if the numerical ranges of the individual input variables differ by several orders of magnitude.

It is usually practical to scale the network inputs to the numerical range of the activation function to avoid the associated issues and to improve training efficiency. Several techniques can be used to achieve this result. [60]

One common technique is input standardization, where each signal is assumed to follow a Gaussian distribution in the dataset. With this method, each input signal is standardized based on the distribution of the training dataset with the mean μ and the standard deviation σ.

$$\tilde{x} = \frac{x - \mu}{\sigma} \tag{2.14}$$

The method has been shown to accelerate convergence during training, but it relies on the assumption that the input data follows a Gaussian distribution. Another method is input normalization, also known as min-max normalization, where each signal is subtracted its minimum value $x_{\min}$ and then divided by its norm $x_{\max} - x_{\min}$.

$$\overline{x} = \frac{x - x_{\min}}{x_{\max} - x_{\min}} \tag{2.15}$$

The method is vulnerable to outliers since only the minimum and maximum values of the data range determine the scaling range. However, in contrast to input standardization, it does not rely on a specified data distribution to remove scaling effects.

Training Validation During training, the network's predictive performance must be closely monitored to ensure its applicability. Therefore, the available dataset is typically divided into distinct subsets:

- Training Dataset
- Validation Dataset
- Test Dataset

The training dataset is used to adapt the network's trainable parameters to minimize the given loss function. During training, the validation dataset is

used to assess performance and prevent overfitting to the training data. If a divergence between the loss on the training dataset and the validation dataset is detected, the training process is usually stopped. This procedure is also known as Early Stopping [60]. After training is complete, performance is evaluated on an independent test dataset to ensure there is no data leakage.

The distribution of data between the training and validation datasets can significantly affect the generalization of the trained network, especially with small training datasets. Cross-validation strategies that use different dataset distributions can reduce these distributional effects [62]. A widely used approach is a fold-based cross-validation strategy, as illustrated in Figure 2.3, where Δ denotes the prediction error.

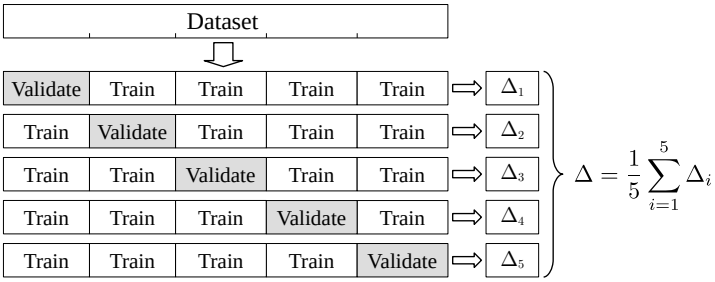

Figure 2.3: Cross-validation example for five folds (inspired by [63]).

The dataset is split into training and validation sets, and the network is trained on each combination. This approach mitigates the effects of overfitting to a specific training data distribution, and comparing the results across folds provides insights into the overall generalization of the training process.

Hyperparameter Search The neural network's architecture significantly influences the prediction error. A network that is too small may not capture the complexity of the predicted behavior, and a network that is too large may not generalize well to the training data. These structural parameters, such as the width of each layer and the number of layers, together with relevant parameters for the training procedure, including the learning rate, the rate at which individual parameters are adapted with each training iteration, are called hyperparameters [62]. These parameters can interact, making manual optimization challenging.

Hyperparameter search algorithms provide a solution for optimizing network architectures. These algorithms randomly iterate through possible configurations or follow a specific schedule to find advantageous hyperparameter combinations. The process usually involves training multiple networks with different architectures to identify suitable parameter combinations.

One common approach for hyperparameter search is the so-called grid search, in which possible combinations of hyperparameters are evaluated systematically. This option is commonly applied but requires high computational resources due to the large number of evaluated parameter configurations, which is determined by the number of hyperparameter combinations. Furthermore, solutions between the specified grid values cannot be explored and selected due to the given discrete parameter grid.

Another commonly used approach is a random parameter search, in which parameter combinations are randomly selected from the search space. In theory, this option can find the best configuration, but it heavily depends on the number of search evaluations conducted. [64]

Other options, such as genetic algorithms and hyperband search, can incorporate relationships between the performance of similar parameter configurations to find appropriate network architectures more efficiently. [65], [66]

Encoder and Decoder Architectures Structural adaptations in neural networks can be used not only to increase mapping accuracy but also to introduce an artificial information bottleneck to extract specific information from datasets. The fundamental idea, that two neural networks can be used in conjunction to extract information and obtain efficient data representations, has been applied frequently [67]. The concept is visualized in Figure 2.4.

In these approaches, one neural network, the encoder, extracts information from an input $\vec{x}$ to a dimensionally reduced latent representation $\vec{z}$ at the bottleneck.

$$\vec{z} = \phi(\vec{x}) \tag{2.16}$$

This latent representation is then entered into the second network, the decoder, to reconstruct the original input.

$$\hat{\vec{x}} = \chi(\vec{z}) \tag{2.17}$$

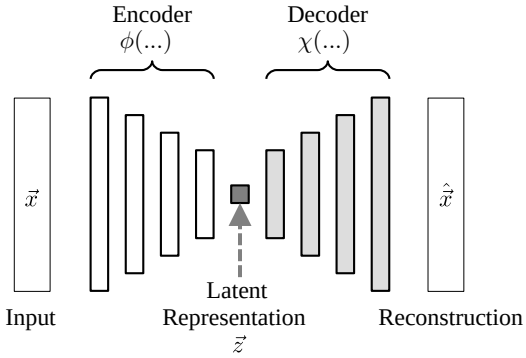

Figure 2.4: Visualization of an autoencoder.

Kramer researched whether artificial bottlenecks in neural network structure can be used to extract information for multivariate datasets. He proposed using mapping layers that compress the input to a bottleneck layer, and remapping layers that then reproduce the output. His findings include that, for extracting nonlinear features, a minimum of three hidden layers is essential. His results show that the method is more effective in reducing nonlinear data than the commonly used principal component analyses (PCA). [68]

Cho *et al.* used the same principle idea with a recursive neural network for sequence generation. In their approach, the mapping layers are called encoding layers, and the remapping layers are decoding layers. They demonstrate the qualitative functionality of the encoder-decoder architecture on language translation. They conclude that the model can capture linguistic regularities at multiple levels. [69]

Sutskever *et al.* applied the approach with Long Short-Term Memory (LSTM) networks to map word sequences to other word sequences. They used an LSTM network to encode the data to a fixed dimension, and another LSTM to decode it to the output sequence. Their results show that the approach can effectively encode and decode very long sequences. [70]

Nowadays, the approach is used in various fields and applications. Mienye *et al.* provide an overview of the various architectures that utilize a combination of an encoding and a decoding network, collectively referred to as an autoencoder. [71]

Conditional autoencoders are a special form of the autoencoder principle that are adaptable to external conditions. In addition to the regular input, conditional autoencoders use additional conditional input $\vec{u}$ to enable the model to learn based on specific given conditions. The original equations are hereby adapted as follows. [71]

$$\vec{z} = \phi(\vec{x}, \vec{u}) \tag{2.18}$$

$$\hat{\vec{x}} = \chi(\vec{z}, \vec{u}) \tag{2.19}$$

2.2 Related Work

Optimizing the efficiency of agricultural production requires considering each process throughout the entire production cycle. As research on construction machinery has shown, a detailed analysis of the elements required for each task is useful for identifying potential areas for optimization [72].

Several of these areas are directly applicable to agricultural processes, including the need for efficient machinery, optimized energy sources, optimized processes, and efficient operating strategies. Considerable progress has already been made, for example, through more efficient drivetrains and new forms of energy supply (see Section 2.1.1). In particular, systems designed to optimize the interaction between the machine and its environment, such as tire pressure monitoring systems, have become established in the market [73]. Furthermore, process adjustments, such as reducing energy-intensive soil processing steps through reduced tillage strategies, have shown potential for optimization [74].

Despite technological and organizational advances, there remains potential to optimize and automate the operating strategies for the multitude of machines used throughout the process chain. It is important to note that the work processes and, therefore, the optimization approaches during fieldwork differ fundamentally from those of other mobile machines, such as the cyclical processes typical of construction machinery.

From a regulatory perspective, the automation of agricultural machinery can be compared to the automotive industry, which has already described the tasks of a machine operator in detail [75], [76]. Several levels were defined

to classify the state of automation. These levels were incorporated into SAE J3016, which characterizes the state of automation from 0 to 5, from where the driver operates all driving tasks to where longitudinal and lateral control is taken over, followed by the removal of the need for a driver fallback. [77]

Streitberger *et al.* transferred these levels to the agricultural sector. Hereby, they note that, in addition to the driving task, which is comparable to the task in the automotive industry, a crucial part of agricultural fieldwork is process control. Therefore, the functions that must be automated at the respective levels are divided into driving and process control subtasks. [78]

Schmidt researched the assessment of the work task of an operator who handles an agricultural tractor-implement combination with the focus on the work quality. Similar to [78], in addition to the driving task, which is the focus of the automotive industry, additional tasks must be considered for the automation of agricultural fieldwork. The operator's overall task is separated into the driving and process control tasks. Based on this task separation, a model was developed to describe the operator's relevant functions during agricultural fieldwork. The model is visualized in Figure 2.5. [79], [80]

For the driving subtask (Subtask II), most machine manufacturers already offer solutions in the form of track planning software and the associated GNSS-based steering control in the field. Some manufacturers provide this not only for individual lanes but also for turning maneuvers.

Schmidt separates the work process control task (Subtask I) into three layers. The work process planning, which occurs before conducting the actual task, involves process optimization to ensure the optimal execution of the task, and process stabilization, which performs low-level control, taking into account the requirements of the previous two layers. [79]

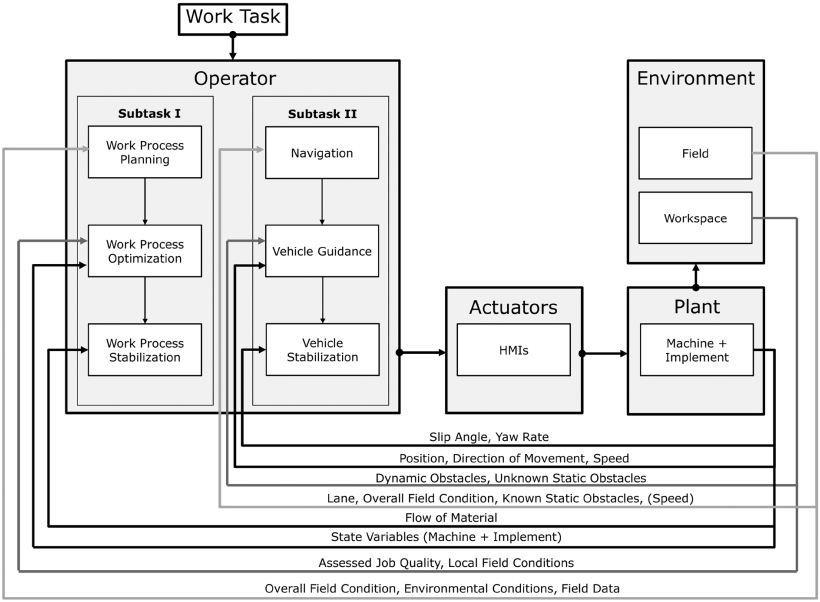

Figure 2.5: 3-layer model for automation of agricultural fieldwork by Schmidt [80].

Work process optimization is a central part of agricultural fieldwork. The operator must supervise various process targets and limitations within this task. Renius defined the possible process objectives as follows [9]:

- Performance
- Process Quality
- Energy Consumption
- Environmental Protection
- Comfort
- Safety
- Economy

Some of these individual objectives have been researched intensively.

Scherer investigated the assessment of mobile machinery's efficiency and defined general productivity metrics for mobile working machines following the definition of productivity indicators for services by Möller *et al.* [81].

In the work, the productivity of a machine is described as the relationship between the result of the work and the required resource input. [82]

$$\text{Productivity} = \frac{\text{Work Result}}{\text{Resource Input}} \tag{2.20}$$

These metrics can be applied to the calculation of productivity with monetary, energy, or time-based resources [82].

In the agricultural context, the process efficiency of the task conducted highly influences the resource input. The primary focus of current research lies in observing and optimizing process quality and efficiency.

2.2.1 Process Quality

Riegler-Nurscher *et al.* researched the automated assessment of soil and plant properties using camera systems on a power-harrow. They further investigated the possibility of using these measurements to actively control tillage quality. [83], [84]

To showcase the functionality of the previously described 3-layer model, Schmidt researched the depth control of a cultivator based on process quality measurements. As a process quality characteristic, the degree of straw coverage was measured with a camera and analyzed using a CNN model. This information was then used to automatically control the working depth of the implement. [79]

2.2.2 Efficiency

Regarding energy efficiency, extensive research has been conducted not only to model and simulate the performance of agricultural machinery, but also to actively optimize its efficiency.

Some studies focus on analyzing the optimization potential through efficiency improvements by changes in control input.

Schreiber combined an empirical traction model, as described in detail in [38] and [43], with an engine and transmission model in a simulation. Using the draft model proposed in ASAE D497.4 [34], he conducted a unified simulation

to evaluate potential reductions in fuel consumption and CO_2 emissions during agricultural fieldwork. The simulation model was verified with field experiments. He concluded that an intelligent adaptation of the operating speed could lead to an increase in efficiency of up to 8 %, and an appropriate choice of gear settings or transmission ratio to up to 20 % [44].

Meiners extended Schreibers model and developed a universal simulation model based on it, the *Hohenheimer Maschinenmodell*, which has a modular structure and can be parameterized for the individual machine. For this purpose, several characteristic maps are stored in the simulation model, which describe the efficiency of the individual components in the drivetrain. The model can be used in combination with various predefined loads of implements, based on which multiple strategies for increasing efficiency, with a focus on grain harvesting, were derived. [85]

Denker *et al.* states that optimized engine management can increase fuel efficiency by up to 15 % [86].

With the assistance system *CEMOS*, the tractor manufacturer Claas offers a system that helps the driver improve the machine's state. While the system helps the operator select the correct machine settings before operation, during operation, the operator can request optimization regarding power output and efficiency. The system then adapts the machine's internal settings, and the driver can retain or revise these changed settings. [87]

Li *et al.* proposed to improve these control strategies by integrating the implement characteristics into the algorithm. The proposed method includes a combined tractor-implement model based on the respective forces acting on the tractor and implement. The method uses upshift and downshift conditions on a traditional manual gearbox. [88]

Kautzmann *et al.* suggested the use of organic computing algorithms to improve the holistic efficiency of tractor-implement combinations. They developed a simulation model to describe the tractor drivetrain's characteristics, its interactions with the environment, and its working cycle. Using the PowerMix cycles [90] published by the Deutsche Landwirtschafts-Gesellschaft (DLG) as a reference, control strategies were developed to improve the efficiency. As a result, they conclude that observer/controller architectures are capable of optimizing the operating point of a tractor-implement combination. [89], [91], [92]

Becker *et al.* suggested the usage of model-free reinforcement learning algorithms for automating the operating speed for the plowing task. The network used was a deep Q network (DQN) that was first trained offline on a recorded dataset to mimic a human operator and subsequently trained in a natural testing environment to further improve. Due to the algorithm in use, the method is limited to discrete action spaces. In the experiments, the adaptation of the operating speed was selected as the action variable. The specified actions were decelerating by 0.2 km/h, keeping the current speed, and accelerating by 0.4 km/h. The algorithm improved both fuel efficiency and area output. This result is based on a single lane per target function and a single reference lane. [93]

The author researched the usage of offline reinforcement learning algorithms for tillage. The investigated algorithm, a conservative Q-learning algorithm (CQL), supports continuous action spaces and is suited for offline training. Training was performed on a previously collected dataset without retraining on the field. To showcase the model's interchangeability, the evaluation was conducted with a different cultivator than during training. The algorithm achieved an average increase in fuel efficiency of 9.7 % compared to a professional reference driver. [123]

2.2.3 Combining Efficiency and Process Quality

Boysen *et al.* researched the possibility of training a deep learning model to predict the soil-machine response for secondary tillage. The model was trained to extract features from a stereo-camera image and machine data to predict soil roughness coefficients, fuel rate, and engine torque utilization. They conclude that a data-driven architecture can predict these features and furthermore note that the data-driven model depends highly on the composition of the input data. [94]
In [95], they compare different approaches for AI-assisted control of tractors paired with a seeding combination. Multiple objective functions are measured and optimized, including process quality (soil roughness), area output, and fuel consumption. They propose a decision-time planning agent that predicts the outcome of a state transition and evaluates it within a unified utility function that weights and combines the different targets. They conclude that the decision-time planning agent can significantly improve performance and fuel consumption. [95]

Steinhaus conducted research to quantify effectiveness and efficiency for agricultural processes. He developed a method for evaluating the entire agricultural process chain. Here, the fulfillment of the respective process steps is calculated using evaluation functions for each relevant parameter in each step, and the results are then combined into the evaluation variable for the entire process chain using weighting factors. He demonstrated the approach on tillage tasks. [96], [97]

2.3 Research Approach

The state of research indicates that optimization approaches have been developed across several areas of agricultural fieldwork. The optimization of machine design for improved efficiency, as well as the optimization enabled by assistance systems such as automatic steering systems, is already widely applied.

Optimizing the control input shows promise for further increasing efficiency. This concept has been researched in several studies described in Section 2.2.2. Most of these approaches to optimizing energy efficiency by adjusting control inputs neglect their impact on other process objectives. While approaches for integrating multiple process targets exist, as listed in Section 2.2.3, they rely on combining multiple process measurements into a single objective function. This requires the process objectives to be weighted against each other, for which there is as yet no clear basis for calculation from an agronomic point of view. This problem is illustrated by the fact that, for the process quality, the connection with already measurable process parameters and subsequent harvest success has not yet been universally established.

In contrast to directly optimizing a given process target, predicting possible states of an agricultural machine combination can provide the necessary insight into potential advantageous operating points. Compared to a direct optimization approach, which would require feedback from the machine, optimization iterations can be performed in the virtual machine model by predicting multiple states. This approach would eliminate the need for iteration loops to find the optimum operating point.

The presented research lacks a uniform method to accurately and modularly predict the state of an agricultural tractor-implement combination for adapt-

ing the operating point while considering the surrounding environment and the requirement for interchangeability of tractors with implements. The availability of sensor data and the complexity of the drivetrains suggest the usage of ANN-driven modeling approaches. Another challenge lies in applying such a prediction model to optimize the state of the machine combination while considering other process objectives of agricultural tasks, such as process quality, which has yet to be explored.

To summarize the research gap, the following hypothesis is formulated:

«*The prediction of system states enables optimizing the operating point of an agricultural tractor-implement combination.*»

Four research questions were posed to answer the research hypothesis:

- *How can the operational state of an agricultural tractor-implement combination be described?*
- *How can the load of an agricultural implement be predicted, considering the interaction with the environment?*
- *How can artificial neural networks be used to estimate the internal state of a tractor drivetrain based on the load of the attached implements?*
- *How can the operating point of a tractor-implement combination be optimized under agronomic constraints?*

The following chapters will address these research questions.

3 State Prediction and Optimization

This chapter presents the developed method for predicting feasible operating points of agricultural machine combinations and using them for operating-point optimization. Firstly, a definition of the state of agricultural machine combinations is formulated, and influences on the state are described and characterized. Secondly, the method for predicting feasible machine states is derived, followed by a detailed description of each required step in the prediction procedure. The chapter concludes with a specification of a constrained control approach that accounts for additional process objectives during optimization.

3.1 State Description

As described in Chapter 2, agricultural machinery is usually set up into implements and tractors. The implements are specialized to perform one or more specific tasks during the cultivation cycle, and the tractor delivers the required power through traction and additional power outlets.

According to Kautzmann, quasi-stationary conditions can be assumed for agricultural fieldwork [92]. This means that acceleration phases are not considered in this context.

In the quasi-stationary case, the state of an agricultural tractor-implement combination at time t is defined by the vector $\vec{s}$.

$$\vec{s} = \begin{pmatrix} \vec{\omega} \\ \vec{\tau} \\ \vec{\theta} \end{pmatrix} \tag{3.1}$$

This vector can be segmented into three subsets which are the following:

- Controllable Variables $\vec{\omega}$: Variables that can be actively adjusted during operation to change the machine combination's operating point.
- Interface Variables $\vec{\tau}$: Variables that describe the power and force exchange between the tractor and the mounted implements.
- Internal Variables $\vec{\theta}$: Variables that describe the internal state of the tractor.

Figure 3.1 visualizes the state description of the machine combination with a tractor with a weight mounted at the front and a cultivator mounted at the rear.

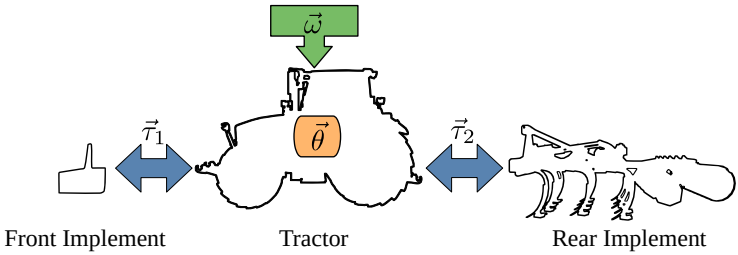

Figure 3.1: Illustration of the state description.

The specification of the variables at the interface between the tractor and the implement describes the state of the combination, which remains valid regardless of the attached implement. Multiple implements can be mounted at the tractor's available interfaces. Therefore, the state description includes the interface variables for each available mounting point. This power can be delivered as forces or using mechanical PTO shafts, hydraulics, electric, or pneumatics. Standardized interfaces are available for each of these possibilities. The tractor supplies the required power to all connected implements at its interfaces.

Table 3.1 lists the respective flow and effort variables for mechanical and hydraulic energy exchange after Isermann. [98]

Table 3.1: Flow-effort depition of energy exchange [98].

Domain	Flow Variables	Effort Variables
Mechanic Translatory	v	F
Mechanic Rotatory	ω	T
Hydraulic	Q	p

For the most commonly used interfaces, the energy transfer within each domain depends on the settings of the respective flow variable, which are controlled from within the tractor. This results in a variation in the load of the implement and in the corresponding load variables for each domain. In these cases, the flow variables are clearly identifiable and are therefore assigned to the controllable variables rather than to the interface variables. In the mechanical translatory domain, specifying an operating speed yields a force demand at the interface. In the rotary domain, this is represented by the specified rotational speed, which results in torque. The hydraulic domain is split into two since multiple types of hydraulic interfaces are available: In the standard case, the volume flow is controlled using tractor-internal valves, and in the other, raw access in the form of power beyond, where the implement can directly access the pressure, tank, and load-sensing lines from the tractor. In the second option, the valve controlling the volume flow is located in the implement. Therefore, the flow variable at the connecting interface of the tractor and implement is not directly the controllable variable of the process and thus part of the interface variables instead. In the electrical domain, the characteristics of energy exchange also depend on the application and implementation.

The controllable variables $\vec{\omega}$ are not the only factors influencing the process's energy demand. In addition, the load demand depends on the machine's operating conditions and, therefore, on the given situation. These situational influences include all external effects on the machine state that cannot be directly adapted or controlled. Therefore, these influences have to be considered separately from the controllable variables $\vec{\omega}$. The situational influences are divided into two categories: the environment parameters $\vec{\epsilon}$ and the process parameters $\vec{p}$.

These two parameter sets can be defined as follows.

- Environment Parameters $\vec{\epsilon}$: Parameters that influence the machine state and are predetermined by external conditions. These parameters are not directly controllable and can change dynamically.
- Process Parameters $\vec{p}$: Parameters that describe the characteristics of the current machine combination. These parameters are typically determined during the setup phase or are set to a specific value to ensure the process is carried out effectively.

Depending on the machine combination and the process being performed, various environmental factors affecting the system state must be considered. Some influences affect all machines, such as gravitational effects on a slope, which result in a draft force demand and changes in weight distribution. Other effects must be explicitly considered concerning the process. For example, soil moisture level plays a crucial role in tillage tasks, whereas in process steps involving material application, the specific material properties must be considered.

The process parameters are predefined parameters that affect the system state. Because of the predefinition, these parameters are not used in dynamic optimization. Some process parameters can be measured directly, while others are difficult to quantify. These parameters may include the working depth of the implement, defined by the process to be executed, or specific settings, such as the roller height of a cultivator, which require a standstill and manual configuration.

3.2 State Prediction

In agricultural machinery, controllable variables are used to control the process and, therefore, the power exchange between the tractor and implements. For the basic case, these variables are the operating speed v, and for each interface i, the rotational speed of the PTO output shafts n_i, and the hydraulic flow rates Q_i. Regarding operating speed, it is worth noting that the input variable in current agricultural machinery is usually the vehicle's theoretical speed rather than the operating speed. Because operating speed directly affects the implement power demand, this approach chooses it as the controllable variable rather than the theoretical speed.

The prediction of a possible machine state $\hat{\vec{s}}$ takes controllable variables $\vec{\omega}$ as input, but must also consider the environment parameters $\vec{\epsilon}$ and process parameters $\vec{p}$ of the current situation.

Mathematically formulated, this leads to the following equation, with $f(\,)$ as the prediction model:

$$\hat{\vec{s}} = f(\vec{\omega}, \vec{\epsilon}, \vec{p}) \tag{3.2}$$

As previously described, tractors can be combined with the implements required for the various tasks in the agricultural process chain. This interoperability can also be incorporated into the prediction process by decoupling the prediction of the process load from that of the drivetrain characteristics. The process is visualized in Figure 3.2.

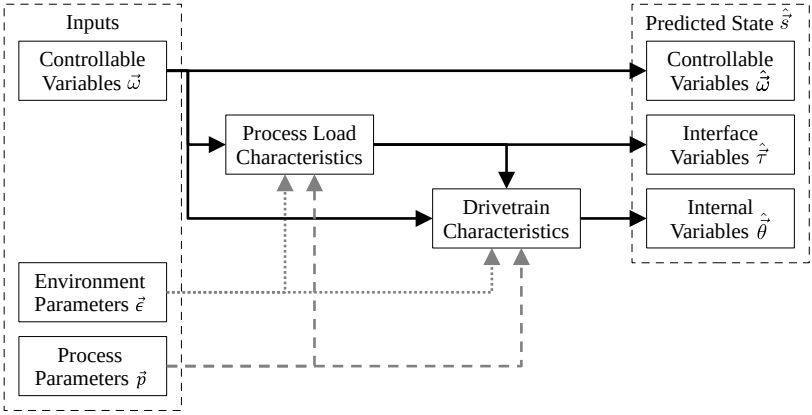

Figure 3.2: Illustration of the prediction architecture (adapted from [125]).

In the first step, a set of controllable variables is selected for which the interface variables and internal variables are unknown. Furthermore, the relevant environment and process parameters are incorporated in the prediction input in accordance with the process.
Then, the resulting process load is predicted using a model that incorporates the characteristics of the implement, along with controllable variables, environment parameters, and process parameters, as inputs. This process is described in detail in Section 3.2.1. The resulting process load is expressed

as the load at the interface between the tractor and the implement, which defines the corresponding interface variables.
In the final prediction step, described in detail in Section 3.2.2, all previously determined information is used to predict the tractor's internal variables, accounting for energy losses along the drivetrain and assessing the feasibility of the state. The output is, therefore, whether the tractor can supply the required power demand and, if so, what primary energy consumption would be coherent.

As a result of the prediction process, a state description for the machine combination is derived by combining the controllable variables, the interface variables, and the internal variables.

The state of an agricultural tractor-implement combination is influenced by various situational parameters, like the environment and the process the machine is working on, as described in Section 3.1. These parameters must, therefore, also be considered to predict the state of an agricultural tractor-implement combination accurately. Each module in the prediction architecture considers both the process and the environment parameters. Since not all situational influences can be measured during operation, the prediction approach described below uses spatial autocorrelation to incorporate current machine measurements into the prediction model, thereby improving accuracy. This concept is used several times in the following sections of this work. The approach assumes that the situation's influence on the machine state can be described by a conditional vector $\vec{c}_s$ that combines elements from the environmental parameters $\vec{\epsilon}$ and the process parameters $\vec{p}$.

Using this conditional input as an additional prediction input $\vec{x}$ in a prediction model $f_j(\,)$ to predict a prediction output $\hat{\vec{y}}$, the prediction of the resulting state from an interaction of the machine with its environment is described as

$$\hat{\vec{y}} = f_j(\vec{x}, \vec{c}_s) \tag{3.3}$$

It is assumed that a function $g(\,)$ exists to describe the situational influences based on a given input and output of a measured state.

$$\vec{c}_s = g_j(\vec{x}, \vec{y}) \tag{3.4}$$

Figure 3.3 visualizes the standard way of working in parallel lines during agricultural fieldwork, and the fundamental idea of using the spatial correla-

tions of points close to each other. The points a_i and b_i each represent a set of measurements at spatially close locations.

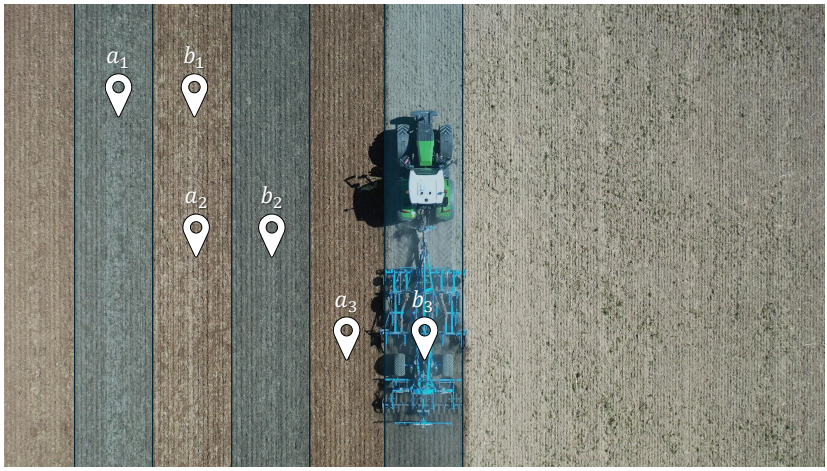

Figure 3.3: Clustering of spatially close measurement locations in a field (adapted from [129]).

It is assumed that the implement configuration is not changed during a single operation and that environmental influences, such as soil type and moisture, are spatially distributed. Given the general approach of working in parallel lanes in agricultural fieldwork, this spatial correlation is applied to neighboring points in parallel lines.

Therefore, it should be possible to extract information about two points a, b that are closely located to each other. Based on this assumption, the situational effects on the machine state are approximated as equal for points a, b.

$$\vec{c}_{s,b} \approx \vec{c}_{s,a} \tag{3.5}$$

This approach can only account for spatially correlated characteristics. Fluctuations occurring at a distance less than the distance between the reference and target points cannot be accounted for by this approach and lead to an approximation error.

Using the previously formulated equations, the situational influence should be detectable using equation 3.4. By incorporating this information into

equation 3.3 and assuming spatial correlation of the environment, additional information is derived to improve the prediction accuracy.

$$\hat{\vec{y}}_b = f_j\left(\vec{x}_b, \vec{c}_{s,b}\right) = f_j\left(\vec{x}_b, \vec{c}_{s,a}\right) = f_j\left(\vec{x}_b, g_j\left(\vec{x}_a, \vec{y}_a\right)\right) \tag{3.6}$$

The structure of the prediction process focuses on two sub-points. The first is the load resulting from the work process, and the second is the prediction of the tractor's internal state, which will be described individually in the following sections.

As some of the models introduced in the following are expressed using explicit coordinate directions, the local tractor coordinate system described in Figure 3.4 is used for all applications. Hereby, the origin is defined at the center point of the rear axle, and the x-axis is defined as parallel to the surface in the direction the tractor is heading and therefore depends on the slope angle δ. The angle β denotes the pitch angle of the tractor.

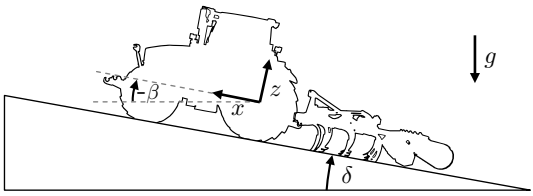

Figure 3.4: Schematic representation of the coordinate system definition.

3.2.1 Process Load Prediction

This chapter describes the process of predicting the load of agricultural processes. Due to the segmentation of the machine into the implement and the tractor, the prediction inputs and outputs for the process load prediction are reformulated for the respective values at the mounting interfaces between tractor and implement.

This prediction process for the process load takes the relevant controllable variables $\vec{\omega}$ as input, along with the given environment parameters $\vec{\epsilon}$ and process parameters $\vec{p}$.

$$\hat{\vec{\tau}} = f_{\text{pl}}\left(\vec{\omega}, \vec{\epsilon}, \vec{p}\right) \tag{3.7}$$

The load of the implement depends on the process conducted and, therefore, on the specific characteristics of the implement and its interaction with the environment.

The tractor-implement combination is moving over a surface that can be inclined upward or downward. This results in gravitational forces acting on the implement. The implement with the mass m requires propelling forces $F_{G,x}$ depending on the gravitational acceleration g when driving on a slope δ.

$$F_{G,x} = m \cdot g \cdot sin(\delta) \tag{3.8}$$

Furthermore, the implement requires support forces from the tractor transmitted vertically to the soil surface.

$$F_{G,z} = m \cdot g \cdot cos(\delta) \tag{3.9}$$

These characteristics can be described as the influence of the environment $\vec{\epsilon}$, the influence of the process $\vec{p}$, and the influence of the control input $\vec{\omega}$. Gravitational acceleration and the field's slope depend on the environment. They cannot be adjusted, as it is assumed that navigation and path selection are predetermined and cannot be optimized. The mass of the implement is a process-specific constant, as some implements can change their weight by distributing products, such as fertilizer, during operation. Furthermore, the weight can be adjusted in advance to optimize the weight distribution.

$$\vec{\epsilon}_{\text{weight}} = \begin{pmatrix} g \\ \delta \end{pmatrix}, \quad \vec{p}_{\text{weight}} = \begin{pmatrix} m_{\text{weight}} \end{pmatrix}, \quad \hat{\vec{\tau}}_{\text{weight}} = \begin{pmatrix} F_{G,x} \\ F_{G,z} \end{pmatrix} \tag{3.10}$$

In addition to gravitational forces, the load of the implement depends on the task and type of implement. One purpose of an agricultural implement is to work the soil, for example, to prepare it for future sowing, to apply seeds, pesticides, or fertilizers. Another purpose is to work on the vegetation, such as during mechanical crop protection, mowing, or harvesting. All these tasks involve interaction with the applied product, the soil, or the plants. This is

also crucial for predicting the process load demand since these interactions must be considered. Many of the parameters needed to describe interactions between the machine and the environment cannot be directly measured during operation, thereby reducing the accuracy of the prediction. However, the current state could be integrated to determine relevant situational parameters and incorporate them into the prediction model.

In the following, two process load prediction models are described that integrate a measured reference state in the prediction process. The first approach is a reformulation of a draft force model originally designed to approximate the draft force demand. The model is modified to be used adaptively by detecting and incorporating situational parameters into the force demand prediction. As a second approach, a fully data-driven method for capturing situational influences based on spatial correlations with an ANN is described. This second approach does not require knowledge of the process, but aims to extract the necessary correlations directly from measurement data.

Adaptive Draft Force Model based on ASAE D497.7 The first prediction approach is a reformulation of the ASAE D497.7 standard [30], which models draft forces for various agricultural implements. The standard allows an approximation of the draft force demand for various implements and operating conditions. It furthermore lists parameter sets for the implement-specific parameters $a_0 - a_2$ for multiple implements. [30]

According to the standard, the draft force demand for agricultural implements F_D can be described universally in terms of the working width d, the depth t, the soil resistance c_soil, the operating speed v, and machine-specific parameters $a_0 - a_2$. [30]

$$F_\mathrm{D} = c_\mathrm{soil} \cdot d \cdot t \cdot \left(a_0 + a_1 \cdot v + a_2 \cdot v^2\right) \tag{3.11}$$

The use of a separate soil parameter in the equation allows for the adaptive recognition of the environment's influence based on a currently measured system state, as proposed by Rößler *et al.* [35].

$$c_\mathrm{soil} = \frac{F_\mathrm{D}}{d \cdot t \cdot (a_0 + a_1 \cdot v + a_2 \cdot v^2)} \tag{3.12}$$

Upon determination of the soil parameter, the updated value is included in equation 3.11, which allows for an approximation of F_D for a given t, d, v and c_{soil} combination.

Since these equations only express the force required to move the implement on a horizontal surface, the gravitational influence has to be considered to express the overall load of the implement to consider inclinations of the soil surface. This leads to the following equation:

$$F_x = c_{soil} \cdot d \cdot t \cdot \left(a_0 + a_1 \cdot v + a_2 \cdot v^2\right) + m_{imp} \cdot g \cdot sin(\delta) \tag{3.13}$$

The parameters contained in the formula can be assigned to the categories described for the state description in Section 3.1.

$$\vec{\epsilon}_{imp} = \begin{pmatrix} g \\ \delta \\ c_{soil} \end{pmatrix}, \quad \vec{p}_{imp} = \begin{pmatrix} m_{imp} \\ d \\ t \end{pmatrix}, \quad \hat{\vec{\tau}}_{imp} = \left(F_x\right) \tag{3.14}$$

The conditional parameter must not only describe the environment's effect, but can also be used to combine all situational influences. Considering a constant working depth t and width d, the equation can be further simplified by incorporating them together with the soil parameter c_{soil} into the conditional process load parameter c_{pl}. This avoids the need to determine these parameters separately.

$$F_x = c_{s,pl} \cdot \left(a_0 + a_1 \cdot v + a_2 \cdot v^2\right) + m_{imp} \cdot g \cdot sin(\delta) \tag{3.15}$$

Upon determination of $c_{s,pl}$, the equation can be used to adaptively predict the draft force demand of the agricultural implements.

ANN-based Approach The ANN-based approach is based on the fundamental idea of neural network-based encoder architectures. As described in Chapter 2, a bottleneck structure in neural networks can be used to extract information from an input $\vec{x}$ by encoding the information in a dimensionally reduced latent form $\vec{z}$ using a decoding function $\phi(\ )$. This characteristic can be used to extract situational information from measured machine state data. By enforcing the network to encode this information in a dimensionally reduced

form, the resulting representation can be used to analyze the information extraction process.

$$\vec{z} = \phi(\vec{x}, \vec{c}_{\text{cond}}) \tag{3.16}$$

$$\hat{\vec{x}} = \chi(\vec{z}, \vec{c}_{\text{cond}}) \tag{3.17}$$

The proposed approach leverages the spatial correlation of environmental parameters in agriculture, as previously described. In contrast to reconstructing the same input y_a in the decoder as entered in the encoder, the decoder is trained to deconstruct an output at a spatially close location y_b. The original prediction input x_i, is entered as a conditional input for both the reference point a and the target point b. This second network is therefore named the predictor function $\psi(\ )$ since it does not reproduce the input as in a decoder, but rather predicts another datapoint.

$$\vec{c}_{\text{s,pl}} = \phi(\vec{y}_a, \vec{x}_a) \tag{3.18}$$

$$\hat{\vec{y}}_b = \psi(\vec{c}_{\text{s,pl}}, \vec{x}_b) \tag{3.19}$$

The network thus implicitly learns these environmental correlations, as it must reproduce them based on a separate spatially close state measurement.

For the process load prediction, the input of the prediction model includes the controllable variables $\vec{\omega}$, directly measurable environment prameters $\vec{\epsilon}$ and process parameters $\vec{p}$, and the output is the interface variables $\vec{\tau}$ as described in Equation (3.7). The input and output of the model can therefore also be described in the form of the input vector $\vec{x}$ (Equation (3.20)) and the output vector $\vec{y}$ (Equation (3.21)) at a given position i.

$$\vec{x}_i = \begin{pmatrix} \vec{\omega}_i \\ \vec{\epsilon}_i \\ \vec{p}_i \end{pmatrix} \tag{3.20}$$

$$\vec{y}_i = \vec{\tau}_i \tag{3.21}$$

Figure 3.5 visualizes the proposed prediction architecture. The encoder (see Equation (3.4)) takes the input and output from the current state measurement of point *a* and, due to the architecture's artificial bottleneck, compresses the information into a lower-dimensional latent representation. Then the predictor (see Equation (3.3)) uses this situational input as an additional input together with the actual prediction input from point *b*.

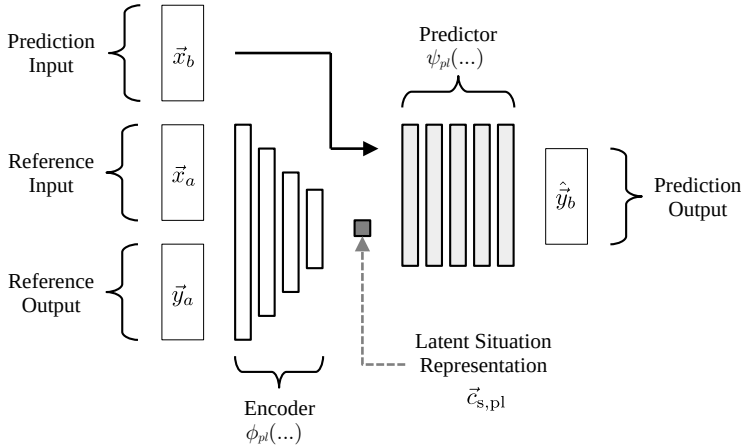

Figure 3.5: ANN-based architecture for process load prediction (adapted from [129]).

The key requirement of the architecture is a training dataset that contains pairs of datapoints, where the situational influences are the same and the prediction input differs, allowing the network to learn the relationships introduced by the process and the environment.

3.2.2 Drivetrain Prediction

The central point of the state prediction is to predict the drivetrain's internal state $\hat{\vec{\theta}}$ for a given controllable variable set $\vec{\omega}$. The load vector of the implements $\vec{\tau}$ introduced to separate the process load prediction from the drivetrain prediction (Figure 3.2) is already determined by the process load prediction and therefore included as an additional input in the drivetrain model. In

additon to this, the environment parameters $\vec{\epsilon}$ and process parameters $\vec{p}$ are considered.

$$\hat{\vec{\theta}} = f_{\mathrm{dt}}\left(\vec{\omega}, \vec{\tau}, \vec{\epsilon}, \vec{p}\right) \tag{3.22}$$

Modern tractor drivetrains can be complex to model. This complexity is not solely due to the wide variety of transmission types, but also to the frequently chosen hydrostatic-mechanical power-splitting approach. The efficiencies of the hydrostats used in these designs are difficult to model analytically, which is why characteristic maps are often used. Furthermore, to predict energy losses along the drive train, the control of the various components must also be considered, as different combinations of engine speed and gear ratio can yield the same operating speed, as with CVTs. This control is usually automatic in modern tractors, with the driver only specifying the target speed for pure traction work.

At the same time, agricultural machinery is equipped with a variety of sensors for both required inputs and outputs. This is underlined by the messages already included in the standardized ISOBUS protocol [22]. Table 3.2 lists the respective available messages for some of the state variables, e.g., inputs and outputs of the drivetrain model. Each signal is assigned a unique suspect parameter number (SPN) according to the underlying J1939 protocol.

Table 3.2: Interface Measurements on the ISOBUS [22].

SPN	Signal Name
1859	Ground-based machine speed
190	Engine Speed
1878	Front Draft
1882	Front PTO output shaft speed
1879	Rear Draft
1883	Rear PTO output shaft speed
183	Engine Fuel Rate
513	Actual Engine - Percent Torque

The list shows that, for the mechanical interfaces for information transfer between the tractor and the implement, the ISOBUS standard already provides a basis for information exchange and data availability. This enables

the collection of vast datasets and the deployment of machine learning techniques to approximate the relationship between the input and output of the prediction.

These characteristics of this basic problem closely match the fundamental requirements for using artificial neural networks in these modeling applications. On the one hand, the problem is complex, implying a high modeling effort for conventional approaches. On the other hand, there is high data availability. In contrast to other applications, such as image recognition, the prediction target can be determined directly from recorded internal sensor signals.

Influential situational factors, including environmental conditions and losses along the energy transmission chain between components, must also be accounted for in the drivetrain model.

The prediction input vector $\vec{x}_i$ includes the controllable variables $\vec{\omega}$, the interface variables $\vec{\tau}$, and directly measurable situational influences $\vec{\epsilon}$ and $\vec{p}$ as in Equation (3.23). The prediction outputs $\vec{y}_i$ are the internal variables $\vec{\theta}$ (Equation (3.24)).

$$\vec{x}_i = \begin{pmatrix} \vec{\omega}_i \\ \vec{\tau}_i \\ \vec{\epsilon}_i \\ \vec{p}_i \end{pmatrix} \tag{3.23}$$

$$\vec{y}_i = \vec{\theta}_i \tag{3.24}$$

Because the environmental impact on the drive train is mainly caused by traction effects, it is separated into two parts. Due to the high level of sensor technology in the drive train itself, most situation-dependent influences can be detected by sensors. Traction characteristics are an exception here, as it is difficult to directly measure traction parameters that are independent of the control input and therefore constant for various sets of controllable variables in a given situation. Thus, as with the process load prediction model, a spatially close measuring point is used to determine these variables.

Figure 3.6 visualizes the proposed drivetrain prediction approach. The current input is directly fed into the neural network, whereas a reference input/output pair is used to detect the current situation and predict traction characteristics. These findings are integrated into a traction prediction model upstream of the neural network. This means that the neural network only has to learn the

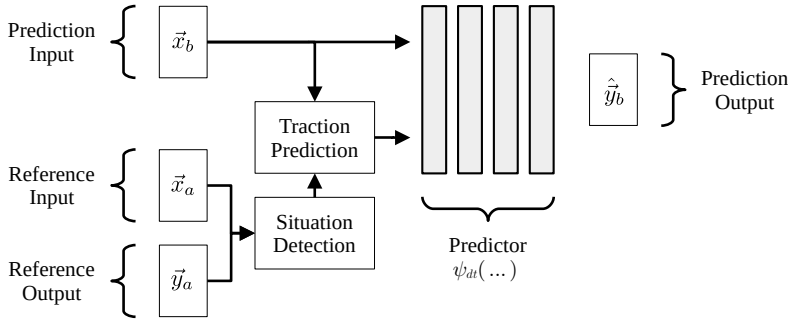

Figure 3.6: Schematic representation of the drivetrain prediction model.

relationship between the inputs and outputs of individual measured points and does not need to extract spatial correlations, unlike the ANN-based process load model.

Traction Prediction As with the process load prediction, external influences and energy losses must be considered when predicting the tractor's internal state, including traction losses. Therefore, information about the current situation and current traction characteristics is required as input in addition to the interface loads.

Traction relationships can be incorporated through feature engineering, where additional inputs for a neural network are specifically designed to enhance prediction accuracy. In this case, the tractive behaviour of a spatially close point is thereby incorporated in the form of an additional prediction input.

Similar to the approach for incorporating situational influence on process load demand, tractive behavior can be detected by measuring a system state during operation.

$$c_{\mathrm{s,dt}} = g_{\mathrm{dt}}\left(\vec{s}\right) \tag{3.25}$$

Many traction models in the literature include such an environment parameter. However, most traction models in the literature aim to represent the tractive effects as closely as possible in the complete range from standstill to complete

tire spinning, whereas the complete slip spectrum is not required in regular fieldwork.
Some tire manufacturers specify slip ranges for heavy fieldwork where the operation should occur. Bridgestone specifies 12 to 15 % as the optimum slip range and points out that at a slip of 30 %, severe soil damage can occur and the risk of seizure increases significantly [99]. Firestone states 15 % as the upper limit and points out that at higher slip rates, it is recommended to wait for the field to dry before tilling [100]. Michelin considers the range between 8 and 15 % as acceptable, and points out that from 15 % onwards, urgent measures should be taken to reduce it [101]. Maxam lists slip rates in between 8 % and 10 % as optimal for four-wheel drive tractors [102]. The German Agricultural Society (DLG) lists in one of their tire test reports that the typical slip rates in practice are between 5 % and 15 % [103]. This suggests that, for practical applications, it is sufficient to consider only a portion of the slip range, rather than the entire range.

While there are many traction models available, the model by Dwyer was selected due to its small number of input parameters and can therefore be easily adapted to different machines. Nevertheless, the model can capture the characteristic reduction of the increase of the tractive force coefficient at high slip rates. The traction characteristics of an agricultural tire are hereby described by Equation 3.26 [52].

$$\kappa = c_1 \cdot (1 - e^{-c_2 \cdot s}) \tag{3.26}$$

Similar to the proposed relationship for a tire on concrete surfaces in [52], the equation is simplified by setting the parameter c_1 to 1. This simplification reduces the accuracy of the equation but means that only a single parameter, c_{dt}, needs to be parameterized.

$$\kappa = 1 - e^{-c_{\mathrm{s,dt}} \cdot s} \tag{3.27}$$

The equation can be rearranged to determine $c_{\mathrm{s,dt}}$ from κ and s. Both required variables can be obtained from a measured system state vector $\vec{s}$.

$$c_{\mathrm{s,dt}} = -\frac{\ln(1-\kappa)}{s} \tag{3.28}$$

With the derived parameter $c_{\mathrm{s,dt}}$, the slip behavior of the overall machine is described within the relevant function space. By measuring the state of a spatially close system, this parameter can be used to determine the vehicle's theoretical speed.

This parameter can then approximate the slip rate s at another close location b by assuming $c_{\mathrm{s,dt},b} = c_{\mathrm{s,dt},a}$.

$$s_b = -\frac{\ln(1-\kappa_b)}{c_{\mathrm{s,dt},b}} = -\frac{\ln(1-\kappa_b)}{c_{\mathrm{s,dt},a}} = \frac{\ln(1-\kappa_b)}{\ln(1-\kappa_a)} \cdot s_a \tag{3.29}$$

3.3 Process Optimization

Theoretically, any optimization of a machine state can be described with the maximization of a given objective function $h(\vec{s})$. This can be achieved by adapting one or more controllable variables of the machine $\vec{\omega}$, resulting in the following equation:

$$\arg\max_{\vec{\omega}} \quad h(\vec{s}) \tag{3.30}$$

Agricultural fieldwork aims to maximize harvest yield with as few resources as possible.

$$h(\vec{s}) = \frac{\text{Harvest Yield}}{\text{Resource Input}} \tag{3.31}$$

This fundamental optimization objective raises the issue that each specific task along the agricultural process chain impacts the harvest yield for the specific type of plant that is cultivated. This means that for optimization, the effects of the environment on machine load and efficiency, as well as on plant growth and health, must also be considered. Alongside the type of plant, the composition and moisture of the soil, and external effects like the weather have to be considered. Furthermore, the yield depends on the process quality of each step, and for many of those, there is still no proven way to determine the quality of work. Moreover, linking and quantifying the relationship between the quality of work of each step to the overall harvest yield is another issue that has yet to be solved.

The example of stubble cultivation can demonstrate this problem. Figure 3.7 visualizes the result of three different theoretical speed settings (5, 10, 15 km/h) driven with a cultivator at the same working depth of 8 cm with photos of the result after each of the different passes.

(a) 5 km/h **(b)** 10 km/h **(c)** 15 km/h

Figure 3.7: Visual inspection of the result for fixed working depth of 8 cm and variation of operating speed with a cultivator.

The different speed settings influence the visual appearance of the result. The degree of straw coverage changes significantly from slow to high operating speeds. At the 5 km/h speed setting, much straw remains at the surface, whereas with increasing speeds, the straw coverage decreases. While the amount of straw left on the surface is measurable [79], [84], the issue here is that the connection between the amount of straw left and the actual harvest yield of the upcoming cultivation cycle is hardly quantifiable.

As a result, the fundamental objective function cannot be observed during operation and, therefore, cannot be directly optimized.

However, a human operator can use his experience to define constraints for the optimization space that, according to his knowledge, have the greatest impact on harvest yield. As a result, the objective function $h(\vec{s})$ can be optimized within these constraints.

According to Martins *et al.*, optimization constraints can take multiple forms and vary depending on the task at hand [104]. The first option is to restrict the optimization space to a specific combination of state variables. This can be

expressed by an equality constraint $\mu_{\text{eq},i}(\vec{s})$, which must always be maintained. An example of this is restricting the depth to a specific setting, which is usually relatively shallow during stubble cultivation and deeper during primary tillage. The second option for restricting the optimization space is to deploy inequality constraints $\mu_{\text{ineq},j}(\vec{s})$, which enforce the inclusion of specific state variables or variable combinations within a specified optimization scope. An example is the use of minimum or maximum speed settings during tillage to ensure the implement is working correctly during the task. For instance, during stubble cultivation, low speeds can result in insufficient soil acceleration and, consequently, inadequate mixing of the straw cover with the soil. This effect was previously visualized in Figure 3.7.

Figure 3.8 visualizes these two constraint possibilities in a simplified manner on the example of two of the state vector variables. In Figure 3.8a, the combination of these two variables must strictly be enforced during operation due to the equality constraint posed, whereas in 3.8b, the inequality constraint limits the optimization space.

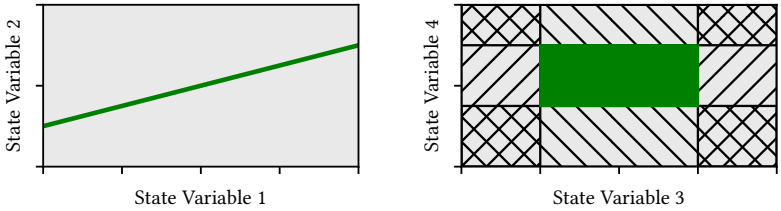

(a) Equality Constraints **(b)** Inequality Constraints

Figure 3.8: Types of Optimization Constraints. The gray space resembles invalid operating points due to active process constraints, whereas the green space resembles valid ones (adapted from [125]).

These constraints can be included in the optimization process. Equation 3.32 visualizes the optimization problem under consideration of constraints mathematically as in [104].

$$\begin{aligned} &\text{maximize} && h(\vec{s}) \\ &\text{by varying} && \vec{s} \\ &\text{subject to} && \mu_{\text{eq},i}(\vec{s}) = 0 \quad \text{for} \quad i = 1, \ldots, n \\ & && \mu_{\text{ineq},j}(\vec{s}) \geq 0 \quad \text{for} \quad j = 1, \ldots, m \end{aligned} \tag{3.32}$$

This approach ensures that the harvest yield is not affected within the defined optimization space, so the influence of a change in operating point within this scope is treated as constant ζ with respect to the resulting harvest yield per area. This means that the function $h(\vec{s})$ can be expressed by an observable target function $h^*(\vec{s})$ multiplied by ζ to consider the impact on the harvest yield.

$$h(\vec{s}) = \zeta \cdot h^*(\vec{s}) \tag{3.33}$$

Many objective functions can be observed during operation. Examples are the productivity functions proposed by Scherer [82]. These functions can be adapted for agricultural fieldwork by relating them directly to the processed area.

Productivity with respect to time is a pure function of the operating speed v and the width d. The function is expressed in ha/h.

$$h^*_{\text{time}}(\vec{s}) = v \cdot d \tag{3.34}$$

Another productivity function is energy efficiency, also known as productivity in terms of energy use. The function expresses the cultivated area in relation to the required energy demand, which for a combustion engine-powered machine would be the fuel consumption B. The function is expressed in ha/l.

$$h^*_{\text{energy}}(\vec{s}) = \frac{v \cdot d}{B} \tag{3.35}$$

The third crucial objective function combines the other two aspects by expressing the costs per hectare. The function, called monetary productivity, incorporates operational costs such as fuel costs per liter C_{fuel}, machine costs

per area C_{area}, and time-specific costs C_{time}, often used for wages and tractor rental costs [105].

$$h^*_{\text{money}}(\vec{s}) = \frac{v \cdot d}{C_{\text{fuel}} \cdot B + C_{\text{area}} \cdot v \cdot d + C_{\text{time}}} \tag{3.36}$$

Each of these productivity functions can be directly observed from the variables in the machine state description. For 3.36, the farm-specific cost rates are also required. This means that these functions can be used to compare the derived states of a state prediction model and select the most advantageous set, thereby setting the respective set of controllable variables as a new control input for the machine.

Together with the proposed method for machine-state prediction, the overall optimization scheme is shown in Figure 3.9 for one optimization cycle.

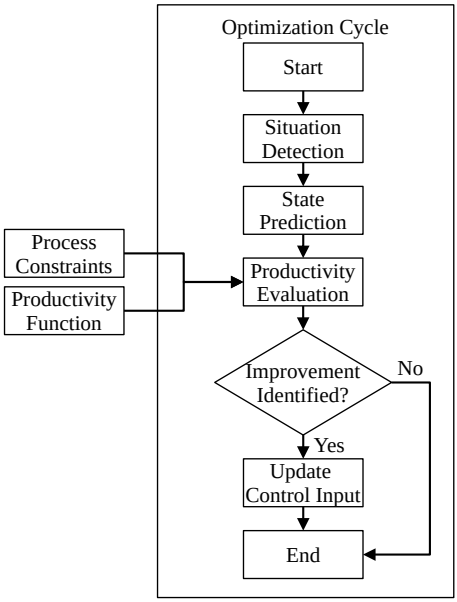

Figure 3.9: Conceptual representation of the optimization procedure.

As input, a definition of process constraints and a productivity function are required, based on which the optimization is carried out. With this informa-

tion, the optimization cycle can be initialized. In the first step, the machine's state is detected, and the situational influences in the prediction models, both for the process load and the drivetrain characteristics, are parameterized. Then, for one or multiple controllable variable sets, the resulting states are predicted. This step includes calculating the resulting process load and the tractor's internal state. Afterwards, the predicted states are evaluated with the selected productivity function. States that violate the specified process constraints are identified and excluded.

If improvement potential is identified in comparison to the current operating point, the control input for the machine combination is adjusted accordingly. If not, the current control input is retained. The optimization cycles can be performed iteratively over time, allowing the consideration of situational changes in the optimization process.

4 Experiments

Experiments were conducted to evaluate the method's applicability. The chapter is structured as follows: First, the experimental setup is described, and then the individual experiments are detailed. Finally, the data processing pipeline is described along with the details of the training of the included artificial neural networks.

4.1 Experiment Setup

This section outlines the technical setup for data acquisition and model evaluation. Because multiple tractors and cultivators were used in different combinations during the experiments, the tractors and implements are first described, along with the combinations used. The section concludes with a description of the measurement software and the data processing pipeline used to generate training and evaluation datasets.

4.1.1 Machine Description and Setup

Two tractors and two implements were used in the experiments and are described below. Section A.2 lists additional technical data on the machines.

The Fendt 724 Gen 6 features a hydraulic-mechanical powersplit drivetrain. For all-wheel-drive, which is frequently used in heavy fieldwork, the front axle of this tractor is rigidly coupled to the rear axle via an all-wheel drive shaft, so that the rotational speeds of the front and rear axles are in a fixed ratio.

In contrast, the Fendt 728 Gen 7 has a higher power output and greater weight. The tractor also features a CVT with a hydraulic-mechanical powersplit. However, the hydraulic transmission branch is connected to two separate

hydraulic motors, one on the front and one on the rear axle. In all-wheel-drive, the separate hydraulic motors and the therefore decoupled front axle allow the drivetrain to be operated without tension, enabling small turning circles and flexible power distribution during fieldwork. With the help of the mechanical all-wheel-drive coupling, the rear and front axles can be speed-coupled during heavy fieldwork. The tractor automatically switches among the different all-wheel-drive modes [106].

The Lemken Karat 10 KUA is a semi-mounted cultivator with three beams and a working width of four meters, on which the working depth can be adjusted hydraulically. However, because the actual working depth also depends on the cultivator's sinking and thus on environmental conditions, the operator must manually verify the set working depth at regular intervals.

As a second implement, a Köckerling Allrounder 600 with a working width of six meters was used. The cultivator is designed for shallower working depths, for example, during stubble cultivation, and therefore has different characteristics.

The tractors and implements were used in different combinations to demonstrate the functionality of the proposed approach as visualized in Figure 4.1.

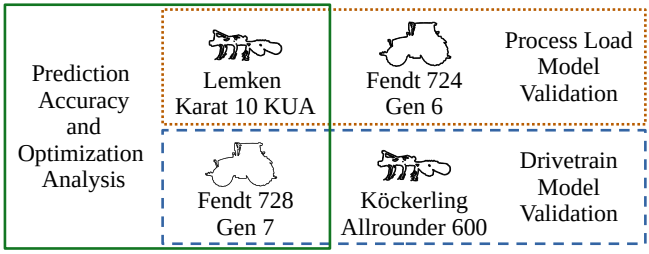

Figure 4.1: Overview of the experiments and corresponding machine combinations.

The experiments evaluate the accuracy of the algorithm's predictions, demonstrate the optimization approach, and validate the transferability of tractor and implement models to other machine combinations. The individual procedure for each experiment is explained later in detail in Section 4.2.

The first combination was the Fendt 728 Gen 7 with the Lemken Karat 10 KUA cultivator, which served as the primary machine combination. It was used to collect the training dataset for the included neural networks, to evaluate

prediction accuracy, and, in the last experiment, to demonstrate the proof of concept of the optimization approach. The machine combination is visualized in Figure 4.2.

Figure 4.2: Primary combination: Fendt 728 with Lemken Karat 10 KUA.

To validate the transferability of the process load model and to showcase that the model can derive generalizable results when used in combination with different tractors, the Lemken Karat 10 KUA of the main experiment was paired with the Fendt 724 as visualized in Figure 4.3.

Figure 4.3: Process load model validation: Fendt 724 with Lemken Karat 10 KUA (adapted from [125]).

The last setup consisted of the Fendt 728 from the main experiment paired with the Köckerling Allrounder 600, which was used to validate the drivetrain models universal functionality when paired with a new implement with new parameters. The combination is visualized in Figure 4.4.

Figure 4.4: Drivetrain model validation: Fendt 728 with Köckerling Allrounder 600.

4.1.2 Software Setup

A Cincoze GM-1000 industrial PC (IPC) with an Intel Xeon E-2278GEL (16 x 2.0 GHz) processor and 64 GB of memory was installed in both tractors to record data from their internal sensors, along with an additional screen for displaying information. The IPCs were equipped with a PCI-CAN card, enabling direct access to the tractor's internal signals. The IPCs were powered by the tractor's onboard 12V power supply, and the PCI-CAN card was connected to the tractor's internal CAN buses. Network connectivity was established via an LTE router. On the IPC, Linux Ubuntu 22.04.4 LTS was chosen as the operating system. To simplify network communication, all code was developed to be compatible with the Robot Operating System 2 (ROS2). With ROS2, communication and data exchange between different programs, also referred to as nodes, are standardized and simplified. Nodes can dynamically access information topics, for example, by subscribing to a topic and receiving all messages published to it. The data types sent on each topic are standardized, simplifying data processing. Information can also be exchanged using a request-response procedure. Here, a node can request

specific information from another node by sending the relevant information context and receive the corresponding response. [107], [108]

The implementation of numerous nodes increases the software architecture's complexity. To counteract this problem, a modular software architecture was developed to run the nodes and supervise the process. Figure 4.5 visualizes the software setup used in the experiments.

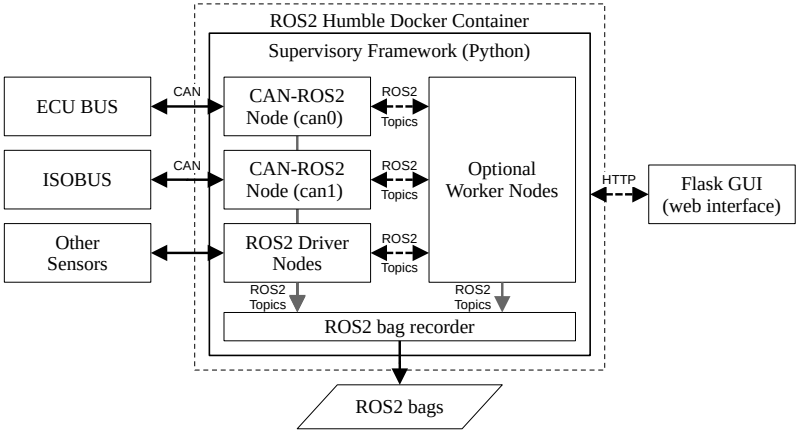

Figure 4.5: Visualization of the software setup.

All software tools were run in a Docker environment to encapsulate them for easy installation and debugging across various hosts. The Docker container hosts a ROS2 installation and a central supervisory framework that runs all software nodes. This has the advantage that each process can be monitored, and errors of individual nodes can be detected and logged to improve debugging and reliability. A central software configuration is predefined for each test setup and then loaded dynamically into the Docker container on the machine. The software packages are also dynamically integrated, so the container itself remains static and does not need to be rebuilt when the software packages it uses are changed. Within the software framework, ROS2 nodes are deployed to access the machine's internal information channels, and depending on the experiment, additional worker nodes are executed, for example, to control the machine in optimization trials or to process measurement data.

A Python-Flask GUI application, developed in HTML and JavaScript, was created to visualize the information of the supervisory framework for the operator. The web interface is accessible through a browser on devices connected to the tractor's local network. It can be used simultaneously on multiple devices, such as separate smartphones or tablets. The graphical interface is visualized in Figure 4.6.

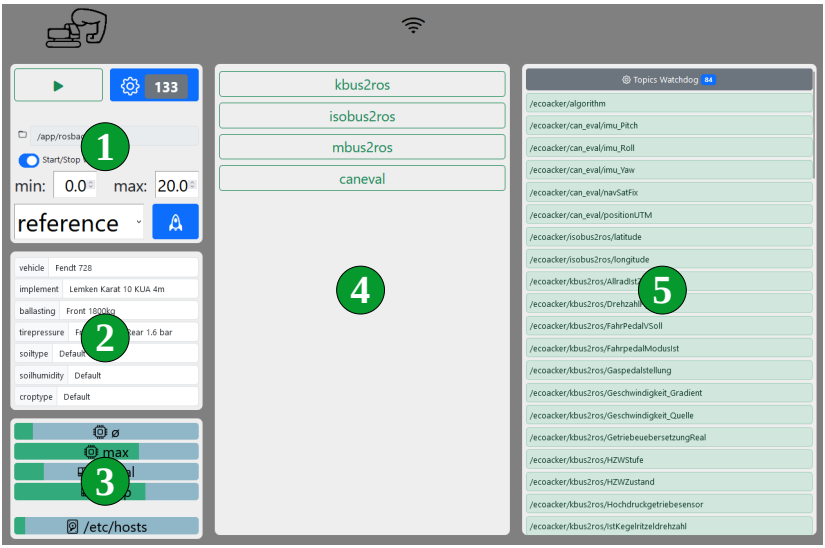

Figure 4.6: Graphical User Interface (GUI). ① Recording Configuration ② Experiment Configuration ③ System Load Monitoring ④ Node Supervision ⑤ Topic Supervision.

In the first section of the interface, the recording process is supervised. Signals to be recorded can be selected from the available ROS2 topics published on the network. The recording process can be started manually, or automatic trigger signals can be used. Experiment-specific information can be entered in the second section of the interface. This information is automatically saved to a protocol along with the recorded sensor signals. In the third section, the IPC's hardware status is monitored to detect insufficient storage space or excessive CPU utilization at an early stage. In the fourth section in the center of the interface, the nodes are launched and supervised. If a node crashes, the operator is visually notified. The supervisory framework can also monitor ROS2 topics by subscribing to them and observing the message frequency

on each topic, as visualized in the fifth section on the right. If a monitored topic does not send messages, the operator is visually notified, regardless of whether a hardware error, for example, a faulty CAN communication, a sensor fault, or a software error, causes the issue. Here, the interface color changes to grey (ready to record), green (recording without error), or red if a node crashes or a monitored topic is no longer received.

To access the tractor's internal sensors, a C++ CAN-ROS2 bridge was developed to decode signals from the tractor's CAN buses and publish them as ROS2 messages. The bridge utilizes a .dbc file to decode the data stream from each connected CAN and publish it as standard ROS2 Float64 messages. Hereby, all other packages can directly subscribe to the ROS2 topics without decoding each signal themselves. Furthermore, the bridge enables the transmission of ROS2 messages to the CAN network, which are then sent according to the information in the .dbc file.

Table 4.1 lists the signals that were read from the internal CAN buses of the tractor. Hereby, one node established access to the ECU bus, whereas another one established access to the ISOBUS. For control access, only the cruise control speed and the engine rotating speed were implemented on the ECU Bus.

Signal	**Symbol**	**Unit**	**Source**
Tractive Force	F_T	N	ECU Bus
Theoretical Speed	v_theo	km/h	ECU Bus
Operating Speed	v	km/h	ECU Bus
Pitch Angle	β	deg	ECU Bus
Engine Rotating Speed	n	1/min	ECU Bus
Fuel Rate	B	l/h	ECU Bus
Engine Torque	T	%	ECU Bus
Longitude	long	deg	ISOBUS
Latitude	lat	deg	ISOBUS

Table 4.1: Overview of CAN signals used for data acquisition.

The theoretical speed v_theo is calculated by the rotating speed of the rear axle and the circumference stored for the respective tires, while the operating speed v refers to the speed above ground, calculated by the ECU from the derived GNSS positions.

The tractor does not provide the option to directly measure the draft forces at the front and rear implement connection interfaces.

Using the mass of the front weight m_{weight}, the draft force at the front interface $F_{x,\text{front}}$ is estimated from the slope angle δ. By assuming a parallel orientation between machine and ground surface, the slope angle is calculated as the negative of the value of the measured pitch measurement β (see Figure 3.4).

$$F_{x,\text{front}} = m_{\text{weight}} \cdot g \cdot \sin(\delta) = m_{\text{weight}} \cdot g \cdot \sin(-\beta) \tag{4.1}$$

The draft force of the rear implement interface $F_{x,\text{rear}}$ is calculated from the total tractive force signal tractor F_{T}, the estimated front draft force $F_{x,\text{front}}$, and the longitudinal component of the tractor weight.

$$F_{x,\text{rear}} = F_{\text{T}} - F_{x,\text{front}} - m_{\text{tractor}} \cdot g \cdot \sin(-\beta) \tag{4.2}$$

Since the tractive force signal calculated by the transmission control unit is based on drivetrain power measurements, its accuracy is limited because the vehicle's rolling resistance must be accounted for. The approach was chosen since no more accurate equivalent measurement options are available in the test setup.

4.2 Experiment Design

The evaluation of field tests has the problem that generating a reference measurement requires an additional pass under the same environmental conditions. During tillage, the machine interacts with the soil, altering its behaviour, which is why a second pass at the same positions would yield invalid results. Since fields are usually tilled in parallel lanes, nearby measuring points from neighboring lanes are available. Therefore, the evaluation of prediction accuracy from one point to the closest point in the neighboring lane was chosen, as this ensures that the soil has not yet been processed. It is therefore assumed that the soil does not change significantly at directly adjacent points as proposed in Chapter 3.2.

The experimental design considers the effect that an increase in the number of evaluated reference lanes also means the distance between points in parallel

lanes, which are compared against each other, increases. Hereby, changes in the influence of spatially correlated environmental conditions cannot be avoided. Therefore, the number of reference lanes should be kept as low as possible. In both the accuracy and optimization analyses, the reference lanes were generated for comparison with the tractor's automatic transmission control (TMS). This approach means that only one degree of freedom, the cruise control speed, needs to be varied to generate the reference lanes, instead of separately varying the controllable parameters of engine speed and operating speed. This has no negative impact on the accuracy evaluation of the draft force demand, as it depends solely on speed. However, when evaluating the accuracy of the powertrain model, it must be noted that the evaluation based on this reference is limited to the typical control range of the automatic transmission. It is hereby assumed that the transmission control system selects advantageous combinations of engine speed and operating speed.

4.2.1 Prediction Accuracy Analysis

As described in Section 4.1.1, the prediction accuracy experiment was conducted using a Fendt 728 with a Lemken Karat 10 KUA. Five fields with dry, loamy soils were selected in southern Bavaria to analyze the prediction accuracy of the proposed method. Each field was divided into blocks with the same working depth. Within each block, the cruise control speed was systematically varied lane-wise. The full parameter spectrum is listed in Table 4.2. The settings remained constant within each lane to minimize the number of acceleration and deceleration events in the dataset.

Table 4.2: Parameter ranges of the prediction accuracy experiment.

Parameter	Unit	Range
Working Depth	cm	6, 10, 16
Cruise Control Speed	km/h	6, 9, 12, 15

It is worth noting that the theoretical speed setpoint results in lower actual operating speeds due to slippage effects. Working depth was measured manually after one lane of each working depth had been processed.

Figure 4.7 visualizes the design of the experiment. The fields were numbered in the order in which they were processed.

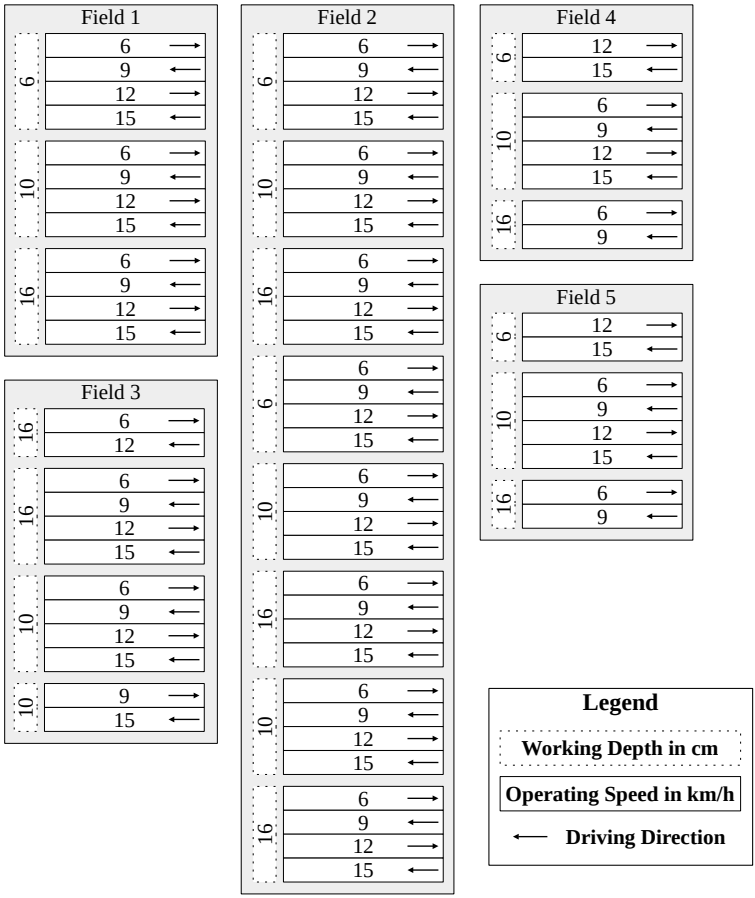

Figure 4.7: Schematic overview of the main experiment.

The Figure visualizes the working depth, operating speed, and direction used in the experiments for the individual lanes driven. To avoid disturbances by additional soil compaction, the blocks were organized between the tramlines. Due to the varying field sizes, not all iterations of the experiment could be

conducted on each field. Only fields 1 and 2 include complete blocks of all combinations, whereas field 3, in theory, contains all iterations, but the 16 cm block is split due to the field layout and tramline design. Fields 4 and 5 contain only parts of the iterations due to an insufficient size.

4.2.2 Process Load Model Validation

This experiment was conducted to ensure that the process load model works independently of the tractor in varying environmental conditions. Therefore, the Lemken Karat 10 KUA from the main experiment was paired with a Fendt 724. A test field in southern Bavaria was chosen. The soil was loamy but moist, and the field had a constant inclination. At the farmer's request, only a constant depth could be used. The reason behind this is that changes in depth would require a second pass for subsequent uniform cultivation. This was avoided for agronomic reasons. Therefore, a single tillage process with a fixed working depth of 17 cm was chosen. The cruise control speed was varied across three levels: 5 km/h, 10 km/h, and 15 km/h.

Table 4.3: Parameter ranges of the process load validation experiment.

Parameter	Unit	Range
Working Depth	cm	17
Cruise Control Speed	km/h	5, 10, 15

Due to the surface inclination, the measured blocks were oriented along the slope, one downhill and one uphill. In the two blocks, the operating speed was varied as visualized in Figure 4.8.

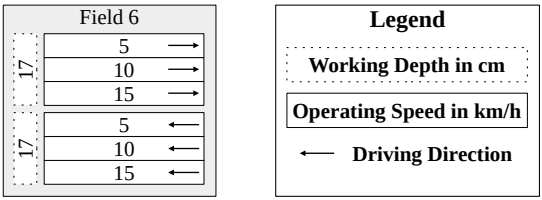

Figure 4.8: Schematic overview of the process load model validation experiment.

4.2.3 Drivetrain Model Validation

This experiment was conducted on dry sandy soils in the region of Schleswig-Holstein, Germany using the Fendt 728 from the main experiment with a Köckerling Allrounder 600 as described in Section 4.1.1. During the experiments, the working depth and speed were varied within specified levels listed in Table 4.4.

Table 4.4: Parameter ranges of the drivetrain model validation experiment.

Parameter	Unit	Range
Working Depth	cm	6, 8, 10
Cruise Control Speed	km/h	5, 7.5, 10, 16

As in the previous experiments, a field was also cultivated with a block-by-block adjustment of working depth and a systematic variation in the cruise control speed. The experiment plan is visualized in Figure 4.9.

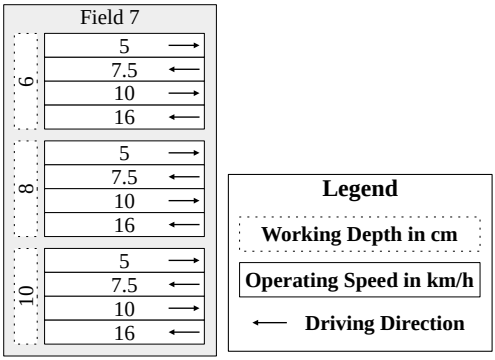

Figure 4.9: Schematic overview of the drivetrain model validation experiment.

In total, three blocks of all evaluated speed configurations were recorded, with varying working depths per block.

4.2.4 Optimization Analysis

As proof of concept for the approach's functionality, the prediction algorithm was used to determine whether such an architecture can optimize the state of a tractor-implement combination. Therefore, the machine combination of the main experiment, the Fendt 728 with the Lemken Karat 10 KUA, was chosen.

The different steps of the optimization approach and the state prediction model were implemented in ROS2 as separate nodes, the process load prediction model in the implement module, and the drivetrain state model in the tractor module. Additionally, a separate optimizer node was implemented to request and evaluate various prediction inputs and outputs.

Communication with the implement and tractor modules was established via request-response. Figure 4.10 visualizes the implementation of the optimization scheme.

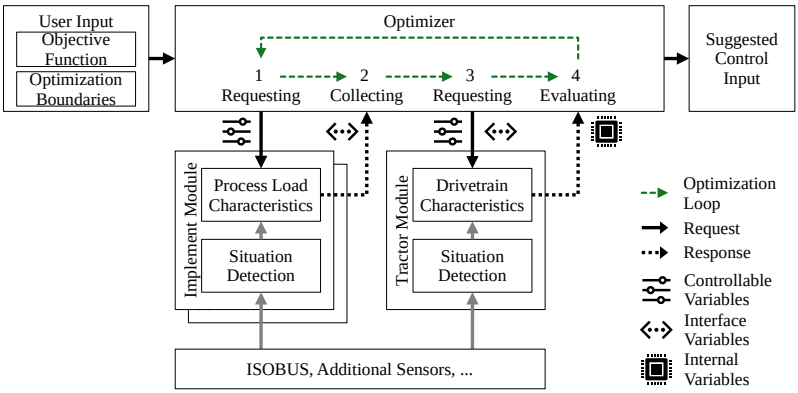

Figure 4.10: Implementation of the optimization approach.

Each optimization loop consists of four steps. In the first step (1. Requesting), the optimizer selects speeds from within the range defined by the optimization boundaries. These settings are then sent to the implements nodes, which respond with the respective loads at the interfaces. After collecting this information from all mounted implements (2. Collecting), the optimizer node sends a request to the tractor node (3. Requesting), which computes the

resulting fuel rate and returns a validity flag indicating whether the predicted fuel rate exceeds the fuel rates in the training dataset. This allows for the identification of operating points that exceed the tractor's capabilities. In the final step, the optimizer node evaluates the predicted states based on the defined objective function (4. Evaluating). It selects and sets the optimal state as the new suggested control input for the machine combination. After this, the next optimization loop restarts at the first step.

In the optimization experiment, the ASAE D497.7-based draft force model was selected as the process load model. Following the proposed state-optimization approach, boundary conditions were established to ensure process quality. Process quality during tillage depends heavily on working depth and varies across the different tillage tasks along the process chain. For stubble cultivation, for example, the optimal working depth depends on the amount and type of organic matter at the surface, and therefore depths of up to 20 cm are standard. However, shallower depths are associated with lower energy use and are therefore preferable. [5]

This means that, for energy-efficiency optimization, the working depth is set to the minimum depth that still yields acceptable process quality. Following the proposed approach, the working depth is therefore treated as an equality constraint. To showcase the algorithm's theoretical functionality, two different depth levels were selected and evaluated.

$$t_1 = 5 \text{ cm} \tag{4.3}$$

$$t_2 = 10 \text{ cm} \tag{4.4}$$

Furthermore, during the initial reference passes, the operator observed inadequate surface smoothing at very low speeds. This speed constraint was set as a boundary constraint, since no negative impact of high speeds was observed.

$$4 \text{ km/h} \leq v \leq 18 \text{ km/h} \tag{4.5}$$

The maximization of productivity with respect to energy usage for the task (Equation (3.35)) was selected as the optimization objective. As the control input, the adaptation of the operating speed and engine rotational speed was chosen.

$$\hat{\vec{\omega}} = \begin{pmatrix} v \\ n \end{pmatrix} \tag{4.6}$$

The operating range of possible operating speeds was sampled in between 4 and 18 km/h (Equation (4.5)) in steps of 0.5 km/h, whereas the possible engine rotational speeds were evaluated in between 800 and 2500 1/min in steps of 100 1/min. Therefore, 29 speed settings and 18 discrete engine speed settings are evaluated per second, i.e., a total of 522 possible machine states.

Because the training dataset includes only operating points selected by the internal drivetrain control, the additional degree of freedom afforded by independent selection of engine and operating speeds is not present in the training data. Therefore, prediction errors can arise due to extrapolation. Also, no precautions were taken to avoid selecting operating points that could cause the tractor to stall, for example, due to excessive torque.

The experiment was designed to avoid comparing the direct performance of a reference driver, as the latter's abilities depend on his level of knowledge and can therefore vary from driver to driver, and environmental influences also play a role. Such an analysis would consequently require a large number of reference drives with different drivers to obtain meaningful results while maintaining constant environmental conditions. Due to the spatial dependencies of the environmental influence, this boundary condition is problematic.

Therefore, an alternative approach was chosen to validate whether the algorithm is fundamentally capable of optimizing the operating point. Parallel reference lanes were driven to compare the algorithm's capabilities to the result of static control inputs. Figure 4.11 visualizes the experiment design. For the references, the automatic transmission control TMS of the tractor was activated using reference speeds of 4 km/h, 8 km/h, and full throttle using the cruise control. It is worth noting that the machine's actual speed is lower than the theoretical speed of the cruise control due to wheel slip. When generating the reference lanes, it is assumed that the transmission control selects efficient combinations of engine speed and gear ratio to achieve the specified speed control speed. In total, two full iterations per depth setting were evaluated.

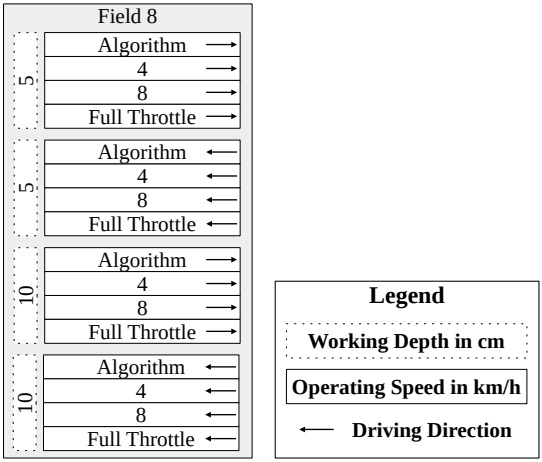

Figure 4.11: Schematic overview of the optimization experiment.

4.3 Data Processing

The datasets from the experiments contain sensor signals at different frequencies, measurements taken during turning maneuvers, and pronounced fluctuations in the measured values. A data processing pipeline was developed to adequately prepare training and test datasets. The pipeline is visualized in Figure 4.12.

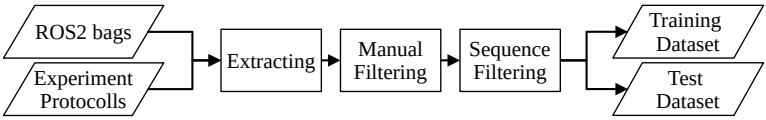

Figure 4.12: Overview of the data processing pipeline.

In the extraction step, the messages in the ROS2 bags are sampled at 10 Hz using their recorded timestamps. This means that, for each specified time interval, only one synchronized sensor signal remains. Additional information, such as the working depth, which was manually measured by the operator, was automatically derived from the experiment protocols and added to the dataset as supplementary information.

Since the parametrization approach requires spatial proximity between points, the GNSS antenna's Longitudinal and Latitudinal coordinates are transformed into the Universal Transverse Mercator (UTM) projection to simplify calculations using meters as the distance unit, with coordinates x_{UTM} and y_{UTM}. In this coordinate system, global latitude and longitude coordinates are assigned to zones, with positions specified in meters along the x- and y-axes. The distortion of perspective introduced by the zones leads to deviations when comparing points that are far apart. For the measuring points in the field, this effect is negligible due to the small distances inbetween. [109]. The UTM projection has the advantage that, by specifying the positions in meters, distance calculations are simplified.

In the manual filtering step, the data is visualized in a custom Bokeh [110] interface to detect missing or invalid sensor signals and filter out invalid data points, such as data collected during dynamic work in headland areas or during machine standstill. The user interface is visualized in Figure 4.13. The recorded signals are spatially visualized. The interface allows selection of points using various spatial selection tools.

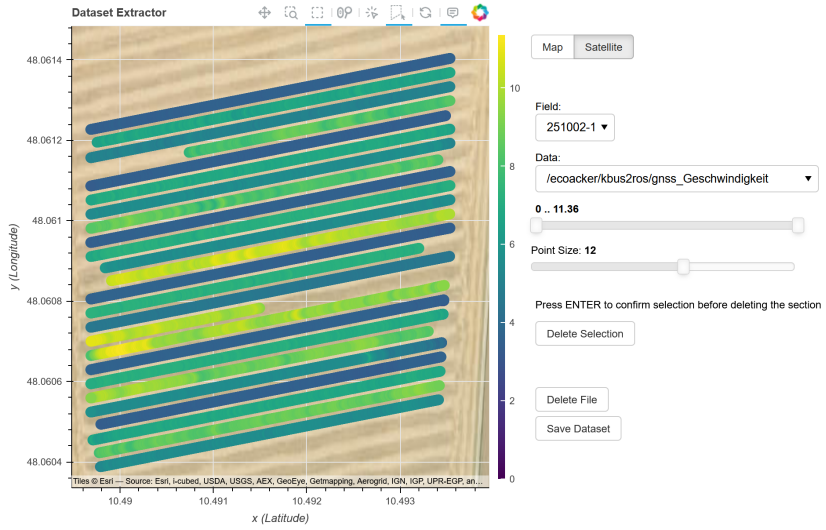

Figure 4.13: Graphical user interface for data filtering.

After the manual processing, the resulting dataset is filtered to reduce sensor noise. A time-slot-based rolling mean filter is applied to all recorded input signals x, given the number of sampled datapoints for the requested filtering interval N. The resulting filtered value $\tilde{x}$ for position n in the dataset is computed as follows.

$$\tilde{x}_n = \frac{1}{N} \sum_{k=0}^{N-1} x_{n-k} \tag{4.7}$$

As a result, a dataset is derived with only valid entries and reduced sensor noise.

Both the neural networks in the ANN-based draft model and the drivetrain model require training data. Therefore, at the end of data processing, four fields from the main experiment were selected as training data, whereas one recorded field was removed from the dataset for independent testing.

4.3.1 Process Load Model Parametrization

The proposed models for predicting process load during operation require parametrization or training to be used for a specific task. This procedure is described below.

ASAE Model The draft model derived by adapting the ASAE D497.7 standard, as described in detail in Section 3.2.1, requires a parameter set for use with a specific agricultural task. ASAE D497.7 lists parameter sets for various implements [30]. It should be noted that the parameter sets for primary and secondary cultivation with a cultivator differ little in their results when used as an online parameterized model [35].

For the experiments, the parameters for a field cultivator in secondary tillage ($a_0 = 32$, $a_1 = 1.9$, $a_2 = 0$) from ASAE D497.7 were used [30, p. 5]. Equation (4.8) shows the parametrized relationship.

$$F_x = c_{\mathrm{s,pl}} \cdot (32 + 1.9 \cdot v) + m_{\mathrm{imp}} \cdot g \cdot sin(\delta) \tag{4.8}$$

ANN Model The second process load model, presented in Section 3.2.1, extracts process load characteristics from reference measurements using an ANN. For the training procedure, pairs of spatially close measurements are required to ensure similar situational influences. Therefore, the positions of the data points must be evaluated for each point in the dataset. The point of interaction of the implement deviates from the tractor's GNSS sensor position, and no separate GNSS antenna was used on the implement. Since adjacent lanes were not always driven in the same direction, the position of the cultivator was calculated using the direction of travel and the distance between the GNSS antenna and the center beam of the implement.

This process is visualized in Figure 4.14 with a top-down view on the tractor-implement combination. The standard coordinate frame is hereby given by the coordinate origin O_{tractor}, whereas the origin to be calculated is denoted as $O_{\text{cultivator}}$.

The direction of each point γ_i is calculated from the filtered trajectory points (0 and 1 in the Figure) using the respective Easting coordinates x_{UTM}, and Northing coordinates y_{UTM}.

$$\gamma_i = \arctan\left(\frac{y_{\text{UTM},i} - y_{\text{UTM},i-1}}{x_{\text{UTM},i} - x_{\text{UTM},i-1}}\right) \tag{4.9}$$

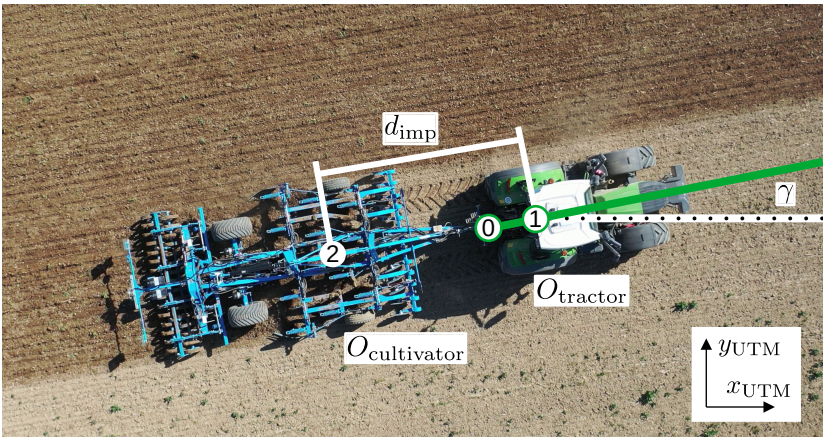

Figure 4.14: Implement location calculation.

As the interaction point, the center beam of the cultivator is chosen. Given the distance d_{imp} between the rear axle of the tractor and the center beam, the UTM coordinates can be adjusted to focus on the implement's position.

$$x_{\text{UTM,imp},i} = x_{\text{UTM,tractor},i} - d_{\text{imp}} \cdot cos\,(\gamma_i) \tag{4.10}$$

$$y_{\text{UTM,imp},i} = y_{\text{UTM,tractor},i} - d_{\text{imp}} \cdot sin\,(\gamma_i) \tag{4.11}$$

With the corrected positions, the dataset was further processed to extract spatially correlated features. Therefore, for each point in the dataset, points in directly neighboring lanes were selected and stored in a central dataset. Due to variations in working depth across some fields, these invalid neighbor associations were removed from the evaluation. This was done for both the training and test datasets. The training dataset consisted of 76,394 data points, and the test dataset comprised 20,050 entries.

Figure 4.15 visualizes the assigned variables at the respective inputs and outputs of the network for the evaluated use-case of the process-load model.

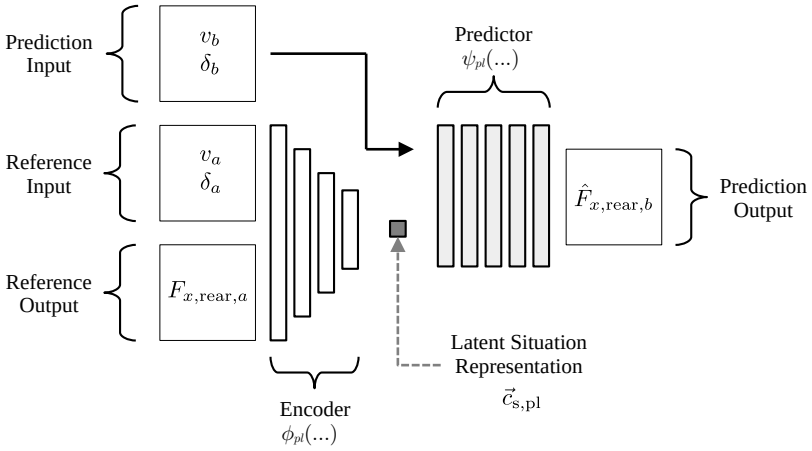

Figure 4.15: Illustration of the ANN-based process load prediction with corresponding variables (adapted from [129]).

Since the cultivator only requires draft power and there are no additional drives, such as the PTO, the operating speed v was selected as the relevant controllable parameter for the forecast. In addition, the slope gradient δ was included in the estimates as an environmental parameter. The reference input parameters comprise the same variables, with the values from the measured reference point. The slope inclination is included in both input vectors because it influences the power requirement and changes with the direction of travel, and thus does not need to be the same for neighboring points. The measured draft force of the reference point $F_{x,\mathrm{rear},a}$ was entered as the reference output. Overall, the neural network outputs the draft force demand at the target point $\hat{F}_{x,\mathrm{rear},b}$.

The neural network architecture was implemented in PyTorch. For the latent situation representation, a size of one was selected to achieve maximum compression of the information content and ensure interoperability of the extracted information.

As shown in Figure 4.15, the encoder network can systematically reduce layer sizes and, consequently, the information content across subsequent layers. A steady compression parameter was used to gradually reduce layer size until the bottleneck, to evaluate whether this could further improve information extraction. The implementation halves the layer size in each additional encoder layer, with a minimum of one neuron per layer. The steady compression hyperparameter was introduced after the initial published approach in [129].

The architecture was optimized in a grid search using a batch size of 1024. The mean average error (MAE) was selected as the loss function for the training procedure, and the input data was standardized. A hyperparameter search was performed using five-fold cross-validation to increase generalizability and avoid overfitting to parts of the data set. The folds were divided into groups of the same lane to avoid mixing measurement points that followed each other in quick succession and were therefore very similar across folds.

As described in the basics of this method, the neural network is trained using different data set divisions, and the prediction errors across the divisions are calculated. This means that division-specific effects that could cause overfitting are less significant. To speed up the search, early stopping with a patience of 10 and a maximum of 100 training epochs was used. The hyperparameter search space and the final network architectures are listed in Table 4.5.

Table 4.5: Process load model: Hyperparameter search space.

Parameter	Search Space	Selection
Encoder Layers	3, 4, 5, 6, 7	5
Encoder Layer Size	32, 64, 128, 256, 512	64
Predictor Layers	3, 4, 5, 6, 7	6
Predictor Layer Size	128, 256, 512, 1024	512
Learning Rate	$10^{-5}, 10^{-4}, \ldots, 10^{-1}$	10^{-4}
Steady Compression	True, False	True

Because the final architecture included the compression parameter, the selected network, and therefore also the results, differ from those published in [129]. The final architecture had an MAE of 2.4 kN with a standard deviation of 5.6 kN across the five folds. The best architecture without steady compression yielded an MAE of 2.5 kN.

4.3.2 Drivetrain Model Parametrization

The drivetrain model was implemented to take the operating speed v, the engine speed n, the loads at the front and rear connecting interfaces, and the slope as inputs. The engine speed was specified directly as input rather than the rotational speeds of the rear and front PTO shafts, since no PTO power was transmitted. This simplifies the model by eliminating the possibility of different transmission ratios between the engine speed and the PTO shaft speed. For PTO-powered implements, the actual transmission ratio should be considered.

Since no sensors are available to measure individual wheel loads and traction forces, the tractive effects at each wheel cannot be detected separately. As the presented approach for detecting environmental conditions and predicting possible system states assumes spatially and temporally constant soil properties, the tractor's traction behavior is described using a reduced-order representation. Based on the reported linear relationship between front and rear axle traction coefficients [9], it is assumed that the overall traction behavior of the vehicle can be approximated by an equivalent representative wheel model. The influence of changes in weight distribution on the front and rear

axles caused by the transmission of vertical forces from the implements is hereby neglected.

The reduced-order representation yields the following equation, which simplifies the vehicle's tractive behavior from Equation (3.27) into a single equation for the entire vehicle.

$$\frac{F_\mathrm{T}}{F_\mathrm{G}} = 1 - e^{-c_{\mathrm{s,dt}} \cdot s} \tag{4.12}$$

The tractive force F_T is hereby calculated by summing up the forces in the x-direction of the implements together with the weight forces of the tractor.

$$F_\mathrm{T} = F_{x,\mathrm{front}} + F_{x,\mathrm{rear}} + m_\mathrm{tractor} \cdot g \cdot \sin(\delta) \tag{4.13}$$

$$F_\mathrm{G} = m_\mathrm{tractor} \cdot g \cdot \cos(\delta) \tag{4.14}$$

This model is incorporated in the drivetrain model described in Figure 3.6 in Chapter 3. The input and output parameters of the model are visualized in Figure 4.16. Here, the traction model is used to extract the traction parameter c_dt, which represents the current traction characteristics. This parameter is calculated from the measured reference point.

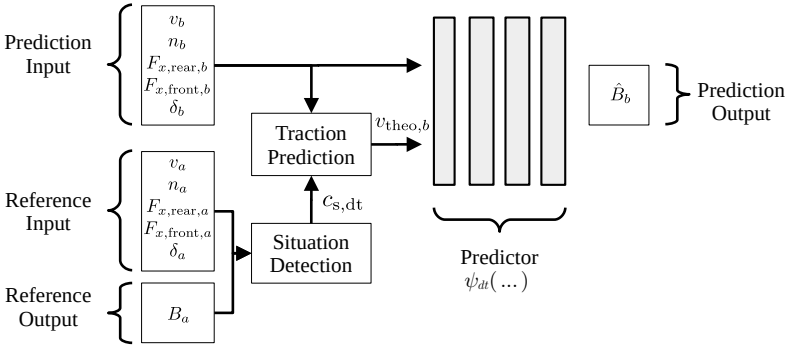

Figure 4.16: Illustration of the drivetrain prediction model with corresponding variables.

The prediction input is then combined with the situational parameter to estimate the slip rate and, consequently, the tractor's theoretical speed. This input, together with the implement loads, is the neural network's input vector, yielding a prediction of the fuel rate $\hat{B}$ at the target point. Because the traction model is separated as a module before the neural network, the

training process does not require neighbor points like the process-load model, since the traction model derives the theoretical speed without being trained on data. Therefore, the network architecture is simpler, and the training process is straightforward.

The training dataset consisted of 56,717 datapoints, whereas the separate testing dataset included 13,060 datapoints. As with the process load model, the training input data was standardized before training.

The network architecture was optimized using a grid search with the parameter space specified in Table 4.6.

Table 4.6: Drivetrain model: Hyperparameter search space.

Parameter	Search Space	Selection
Layers	1, 2, ..., 10	3
Layer Size	8, 16, 32, ..., 2048	1024
Learning Rate	10^{-6}, 10^{-5}, ..., 10^{-1}	10^{-5}

Similar to the process load model, the search was conducted with early stopping and a patience of 10 to minimize overfitting and speed up the search. The MAE was selected as the loss function. Five-fold cross-validation with a lane-wise grouping scheme was performed to ensure the generalization capabilities of the network.

The final network had an MAE of 0.57 l/h with a standard deviation of 0.11 l/h across the five folds.

5 Results

The results are presented in alignment with the experimental structure, beginning with the prediction accuracy and transferability analysis and ending with the optimization analysis.

5.1 Prediction Accuracy Analysis

In the following, the results of the main prediction accuracy experiment (Section 4.2.1) are described. The results are based on the data in the test field, which was not included in the training procedure.

Figure 5.1 visualizes the procedure used to evaluate the prediction accuracy. The evaluation is based on selecting two state measurements with different control inputs, each measured under the same environment and process conditions. According to the proposed method in Section 3.2, the first state is used as a reference to detect current situational influences. This extracted information is used, together with the input of the target state, to predict the output of the target state. In the final step, the prediction's accuracy is evaluated by comparing the predicted output with the target state's measured output.

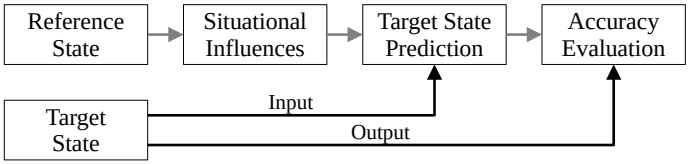

Figure 5.1: Visualization of the prediction accuracy evaluation method.

To assess potential changes in the environment's influence within the field, the results were evaluated using the scheme shown in Figure 5.2. In accordance with the experiment design in Section 4.2, the parallel lanes of the field allow a comparison of measurements with different control inputs. Hereby, each measured state in each lane serves as a reference state for detecting situational influences. Assuming similar situational conditions for spatially close points, this information is then used to predict the state of the closest position on each parallel target lane. As these states were generated with different control inputs and also measured in the experiment, the prediction accuracy can be evaluated. Due to the different speed settings and the fixed measurement sampling rate, the number of measurements per lane varies.

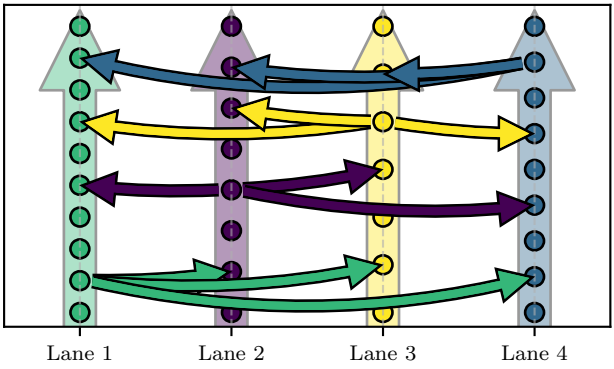

Figure 5.2: Evaluation procedure: Each point acts as a reference measurement for predicting the states of the respective closest points in the adjacent lanes. These cross-lane correspondences enable a direct comparison of states recorded under different control inputs.

In the following, this evaluation procedure is first applied to the process load model, using the reference state to detect the situational draft force parameter. Together with this context, the controllable variables from the target state are used as input to predict the respective interface variables.
In the second step, the drivetrain model is evaluated separately. The situational traction parameter is derived from the reference state, and the controllable variables from the target state are paired with the interface variables as the input to predict the internal variables.
In the last iteration, the two models are combined. The interface variables pre-

dicted by the process load model are directly used as inputs to the drivetrain model to evaluate the accuracy of the entire prediction pipeline.

According to the proposed point-based evaluation scheme presented in Figure 5.2, errors are calculated using neighboring points as references and prediction targets. For interpretability, the mean absolute error (MAE) and the mean absolute percentage error (MAPE) were chosen as the standard evaluation metric. Since the prediction targets vary across the evaluated models, the predictions are denoted as $\hat{y}$, whereas the ground truth is denoted as y.

$$\mathrm{MAE} = \frac{1}{n} \cdot \sum_{i=1}^{n} |y_i - \hat{y}_i| \tag{5.1}$$

$$\mathrm{MAPE} = \frac{100\%}{n} \cdot \sum_{i=1}^{n} \left| \frac{y_i - \hat{y}_i}{y_i} \right| \tag{5.2}$$

Because of the target- and reference-point-based evaluation scheme, variations in the number of measurements across lanes must be accounted for. To ensure that each combination contributes equally to the overall evaluation, the error metrics are first computed separately for each combination and then averaged across all combinations. This procedure is referred to as macroaveraging [111]. Given a total number of combinations m, we obtain the macroaveraged metrics $\overline{\mathrm{MAE}}$ and $\overline{\mathrm{MAPE}}$.

$$\overline{\mathrm{MAE}} = \frac{1}{m} \cdot \sum_{j=1}^{m} \mathrm{MAE}_j \tag{5.3}$$

$$\overline{\mathrm{MAPE}} = \frac{1}{m} \cdot \sum_{j=1}^{m} \mathrm{MAPE}_j \tag{5.4}$$

This approach compensates for the effect of varying numbers of measurements in the different target/reference speed groupings and avoids overemphasizing combinations with slow speeds and, therefore, more measurement points.

5.1.1 Process Load Model

To analyze the characteristic increase in draft force with increasing operating speed, the prediction model based on the ASAE D497.7 standard is evaluated for varying values of the situational parameter $c_{s,pl}$. The approach yields characteristic lines that show the increase in draft force for a given soil type and working depth. This relationship is visualized by dashed grey lines in Figure 5.3 alongside the measured data points. To illustrate the distribution of the measurements, the points are grouped into bins and visualized by color, with each bin showing the number of measurement points. For the illustration, it is assumed that the soil type remains constant across the field and that no slopes are present. Therefore, this form of representation must be treated with caution.

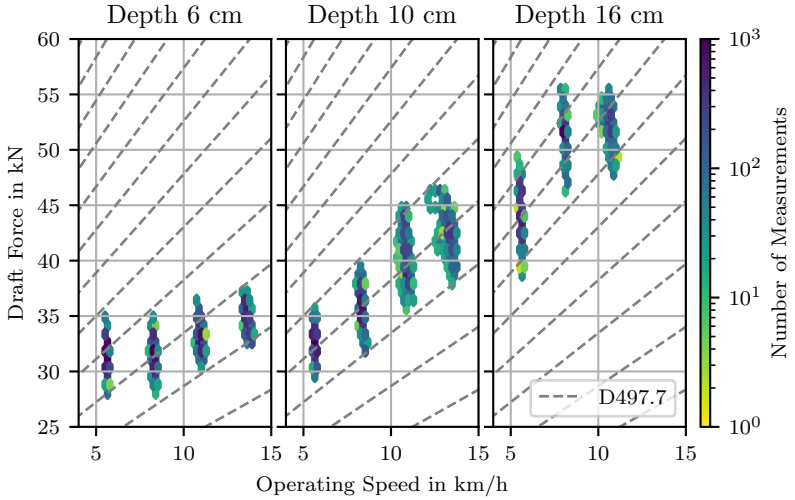

Figure 5.3: Draft force measurements in comparison to ASAE D497.7.

Depth changes lead to significant variations in draft forces. Furthermore, the increase in force with increasing operating speeds is apparent. It can also be seen that there is a difference in the set point speeds described in Chapter 4 to the actual speeds on the x-axis. This is because the reference and target speeds set in the cruise control are theoretical and, therefore, subject to slippage and machine power limitations. The resulting operating speeds

are, thus, lower. The points for the 15 km/h pass at a 16 cm depth align with those of the 12 km/h lane because the required power at the selected speed exceeded the tractor's maximum power output, resulting in a speed decrease. The variance in each lane is high, with fluctuations of up to 10.8 kN in individual rows. This variance includes not only situational changes along the lane but also sensor noise, thereby limiting overall prediction accuracy. Compared with the behavior proposed by ASAE D497.7, at a working depth of 6 cm, the increase in draft force is lower than predicted by the model. At greater depths, the model aligns with the measured data.

Using the reference/target point-based evaluation scheme proposed in Figure 5.1 and Figure 5.2, in total, a $\overline{\text{MAE}}$ of 2.6 kN (7.2 %) was calculated for the ASAE D497.7 model. Figure 5.4 visualizes the prediction error distributions, both absolute (5.4a) and percentage errors (5.4b). To compensate for varying

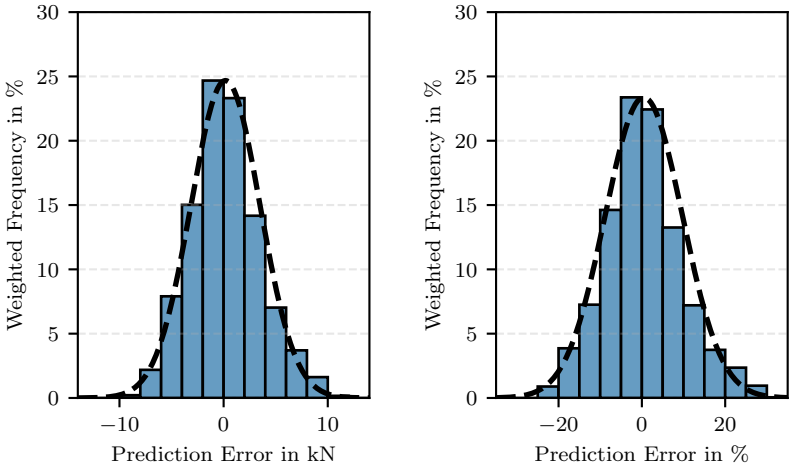

(a) ASAE error distribution.

(b) ASAE percentage error distribution.

Figure 5.4: ASAE model: Draft force prediction error histograms. The blue bars visualize the empirical data, and the dashed black line resembles the fitted normal distribution.

numbers of data points across different target/reference speed combinations in the histogram, each sample is weighted by the inverse of the number of samples in its respective combination.

$$w_i = \frac{1}{n_j} \tag{5.5}$$

Therefore, each evaluated combination contributes equally to the distributions visualized in the histograms.

The histograms suggest that the empirical distributions are similar in shape to the fitted normal distributions and are approximately symmetric around the mean. The distributions show a mean of 0.2 kN and a standard deviation of 3.3 kN, and a mean of 0.4 % with a standard deviation of 9.3 %, respectively. No systematic errors were identified.

The high dispersion of the results is also due to strong fluctuations in draft force measurements. Although the field has homogeneous conditions, the force value fluctuates in the individual lanes as previously noted in Figure 5.3. This aligns with the tillage experiments in [32], where changes of over 10 kN were occasionally measured within a few meters in some areas of a field, suggesting a high variation in draft measurements can occur even at spatially close positions. The use of a reference point to parameterize the prediction model is also susceptible to these local fluctuations, since the reference point may be located at the opposite extreme of the variation, thereby introducing additional prediction errors.

Overall, the ASAE-based model achieved a coefficient of determination of $R^2 = 0.767$, indicating that it explains the fundamental draft force characteristics, but significant deviations remain.

Figure 5.5 shows the average prediction results for the ASAE model for each combination of the reference and target speed settings. The reference point used for the prediction is here on the x-axis, whereas the target is on the y-axis. At the working depth of 16 cm, the values for the 15 km/h lane aligned with those for the 12 km/h lane because the tractor reached its maximum power output. These points were therefore excluded from the evaluation.

As previously described for the data visualized in Figure 5.3, the increase in draft force is overestimated for the lanes with 6 cm working depth with the ASAE D497.7 model. This is particularly evident in the results for the reference speed setting of 6 km/h. As the prediction target speed increases, the prediction error rises. However, the errors do not shift the overall error distribution. Draft values at high speeds are overestimated based on a low-speed reference point, but also lead to underestimation when the reference

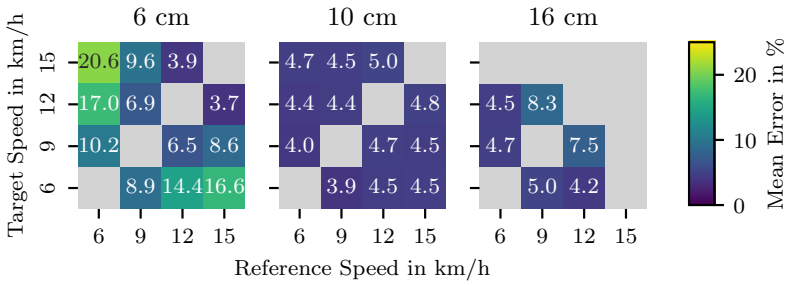

Figure 5.5: ASAE model: Draft force prediction error for different working depths.

and target speeds change. For a working depth of 10 cm, the errors remain relatively stable, with a mean absolute error of 5 %. At a depth of 16 cm, higher errors were measured for both combinations of 9 and 12 km/h reference and target speeds.

Figure 5.6 visualizes the distributions of prediction errors for the ANN model with a $\overline{\text{MAE}}$ of 2.5 kN (6.5 %). The model achieved a slightly higher coefficient of determination of $R^2 = 0.807$.

As with the ASAE model, the empirical ANN-based model error distributions are similar in shape to the fitted normal distributions and approximately symmetric around the mean. The distributions show a mean of -0.3 kN and a standard deviation of 3.1 kN, and -0.6 % with a standard deviation of 8.1 %, respectively. Apart from the slight negative bias, no systematic errors were identified in the prediction distribution.

Figure 5.7 visualizes the prediction errors for each reference and target speed combination. In contrast to the systematic errors in the ASAE model at low working depths, no clear trend is evident in the data. In some cases, for example, at a depth of 10 cm, a reference speed of 12 km/h, and a target speed of 6 km/h, outliers occur. These outliers occur at all specified working depths without a systematic pattern. In the depth of 10 cm, the prediction errors are worse than those of the ASAE-based model with a maximum MAE of 13.3 %. The reason for this could be specific characteristics of the training data set, but the “black box” behavior of the neural network makes an in-depth analysis difficult.

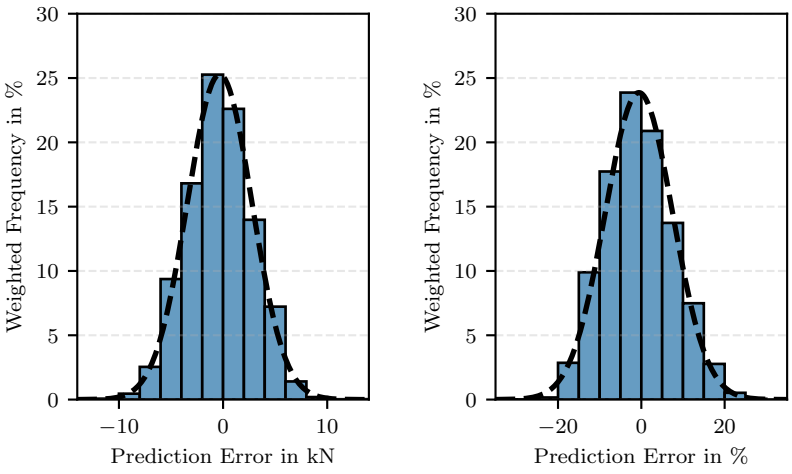

(a) ANN error distribution.

(b) ANN percentage error distribution.

Figure 5.6: ANN model: Draft force prediction error histograms. The blue bars visualize the empirical data, and the dashed black line resembles the fitted normal distribution.

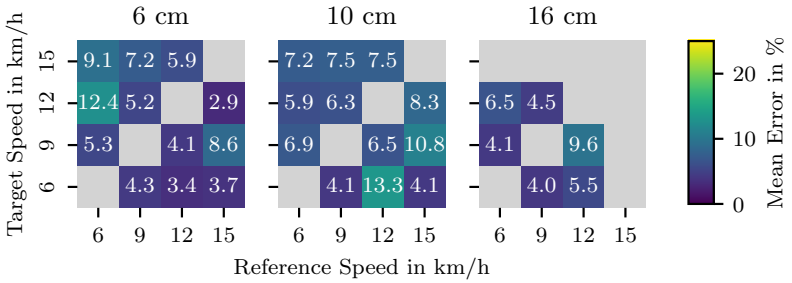

Figure 5.7: ANN model: Draft force prediction error for different working depths.

Different prediction accuracies can result from varying variance or from systematic errors in the prediction models. Figure 5.8 visualizes these characteristics by plotting the distributions of the prediction results for a working depth of 6 cm.

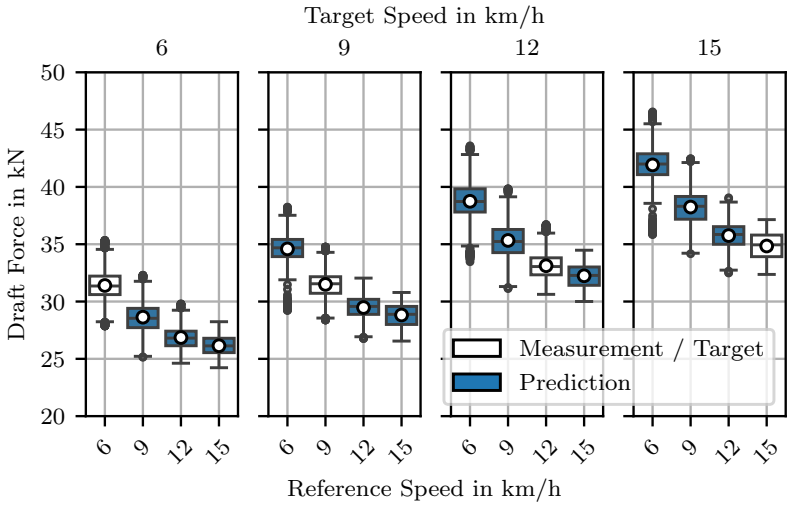

Figure 5.8: Draft force prediction results for the ASAE-model at a working depth of 6 cm. The white boxes resemble the distribution of the prediction targets, whereas the blue boxes resemble the prediction result from the respective reference speed lane.

Here, for each target speed (visualized at the top), the distributions of draft force measurements are shown as white boxes. Furthermore, the distributions of predictions based on each reference speed are visualized as blue boxes. Henceforth, in the left plot for the 6 km/h target speed, the distribution of measurements for the 6 km/h lane is shown alongside the distributions of the predictions based on reference speeds of 9 km/h, 12 km/h, and 15 km/h.

A pattern can be observed: the higher the reference speed, the lower the predicted values, and the greater the deviation of the predicted distribution from the target distribution. The model therefore overestimates the increase in draft forces for an increase in operating speed, which is consistent with the findings of Figure 5.3. Since the ASAE model assumes a linear relationship between operating speed and resulting draft force, at a small working depth, the slope is too steep. Therefore, the average errors listed in the tables above are not due to changes in variance but rather to systematic prediction errors.

Figure 5.9 visualizes the same for the ANN-based draft force prediction model. Here, no such systematic pattern is observed, but rather an increase in the

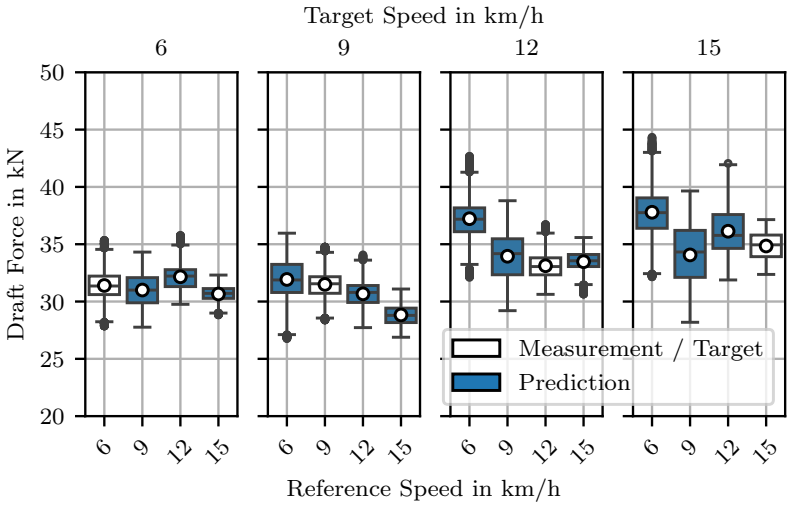

Figure 5.9: Draft force prediction results for the ANN-model at a working depth of 6 cm. The white boxes resemble the distribution of the prediction targets, whereas the blue boxes resemble the prediction result from the respective reference speed lane.

variance of the predicted values. Both models show a general tendency for predicted forces to increase with target speed, as indicated by the mean predictions across target velocities.

Since the ANN-based approach stores the extracted situation parameter in a dimensionally reduced latent form, the correlations of the latent parameter with the working depth were analysed. The Spearman Rank Correlation Coefficient r_s was calculated to describe the relationship between the latent variable and the working depth [112].

$$r_s = 0.73 \tag{5.6}$$

A monotonically increasing relationship is observed.

The stored latent parameter is visualized for the recorded measurement positions in Figure 5.10. The blocks with different working depths can be visually distinguished from each other, as their average values differ: 4.2 for the block with 16 cm working depth at the top, 2.9 for the block with 10 cm, and 2.6 for the block with 6 cm working depth at the bottom.

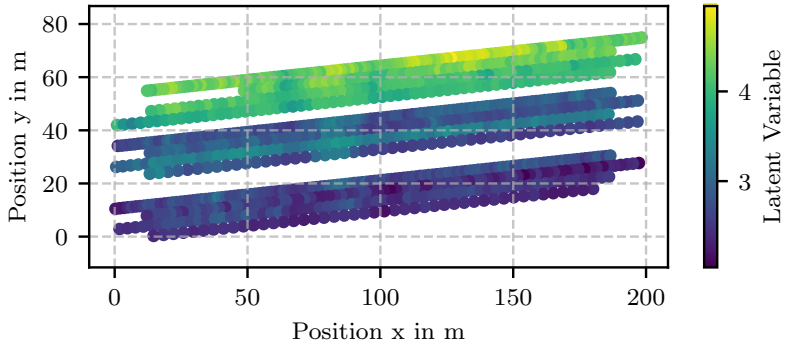

Figure 5.10: Spatial representation of the latent parameter. Working depths: Top 16 cm, middle 10 cm, bottom 6 cm.

This indicates that the extracted parameters are correlated with situational parameters. The high correlation coefficients suggest that the extracted latent parameters reflect the situational conditions.

However, the algorithm requires a training input in which a reference point is available for each prediction input. The similarity between the two inputs must be ensured to enable information extraction. For example, neighboring points in the training data set must have similar situation parameters and not contain any reconfigurations.

The study did not examine the neural networks' extrapolation behavior or the approach's transferability to other situations or implements. Due to the test fields' spatial proximity, the method's transferability to other regions and soil types cannot be guaranteed.

5.1.2 Drivetrain Model

Since the drivetrain model includes a traction model, the respective characteristics are evaluated. Figure 5.11 visualizes the measured slip rates along with the traction force. Furthermore, the grey lines visualize the proposed traction model. Similar to the process load visualization, this graphic assumes a zero slope.

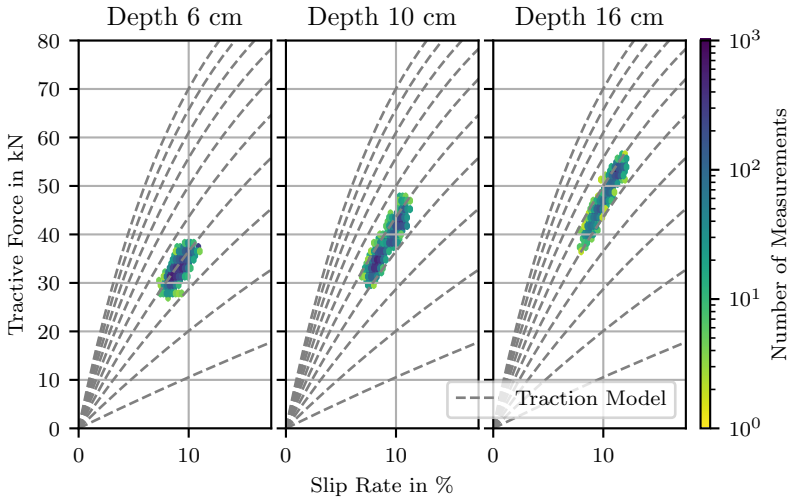

Figure 5.11: Traction measurements for different working depths.

Overall, slip was measured at 7-12.5 %. In this range, the proposed traction model aligns with the measurements. However, a shift in the measured points relative to the model curves is noticeable. When comparing the measurement points at the same slip values, it is evident that at a depth of 6 cm, this slip occurs at significantly lower traction forces than at 16 cm. This could be due to a change in weight distribution between the rear and front axles caused by the introduction of vertical forces.

The results yield a $\overline{\text{MAE}}$ of 0.5 l/h and a $\overline{\text{MAPE}}$ of 1.8 %. Figure 5.12 visualizes the distribution of the drivetrain model for the combination of the traction model with the neural network. The drivetrain model yielded an R^2 of 0.997, indicating that it captures nearly all of the variation in the test data.

The empirical error measurements follow the shape of the fitted normal distributions. The distributions exhibit a mean of -0.02 l/h and a standard deviation of 0.07 l/h, and a mean of 0.05 % with a standard deviation of 2.2 %, respectively.

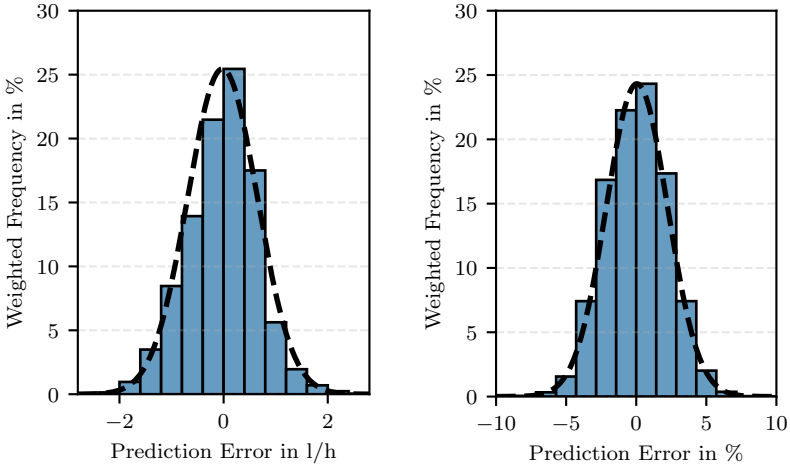

(a) Absolute error distribution.

(b) Percentage error distribution.

Figure 5.12: Drivetrain model: Fuel rate prediction error histograms. The blue bars visualize the empirical data, and the dashed black line resembles the fitted normal distribution.

The errors lie in a significantly narrower range than in the process load model. This can be attributed to the lower influence of fluctuating environmental conditions.

Figure 5.13 visualizes the results of the prediction accuracy of the drivetrain model for the individual reference and target speed settings. Across the whole experiment, a maximum MAPE of 2.5 % was observed.

No clear trends or outliers are observable, and the overall prediction accuracy is significantly better than that of the process load model. This can be explained by the fact that, after accounting for traction effects and environmental influences, the impact of highly variable influences is significantly lower than when modeling direct interaction with the ground.

The dataset was recorded using standard transmission control, with the cruise control speed as the control input. Therefore, it is not possible to make any statements about accuracy across the full range of possible control inputs, given the degree of freedom introduced by the independent variation in engine and operating speed. An evaluation of this characteristic would require additional test series with greater variation.

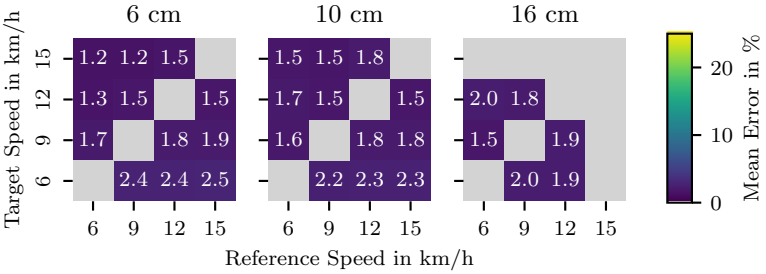

Figure 5.13: Drivetrain model: Fuel rate prediction error for different working depths.

5.1.3 Combined Process Load and Drivetrain Model

In the following, the results for the complete state prediction process are analyzed. The process load model's prediction output is used as input to the drivetrain model. As a result, the fuel rate prediction error is evaluated along the whole prediction pipeline.

Figure 5.14 visualizes the prediction errors for the combination of the ASAE-based draft model with the drivetrain model.

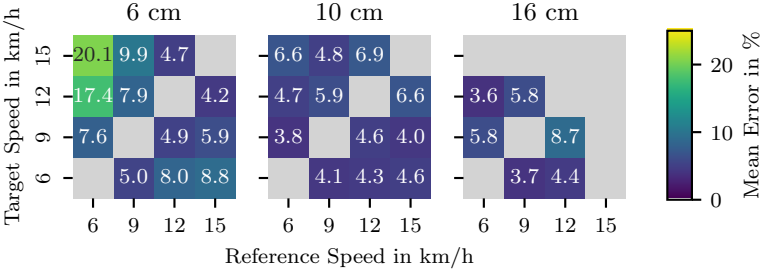

Figure 5.14: ASAE model combined with drivetrain model: Fuel rate prediction error for different working depths.

In total, a $\overline{\text{MAE}}$ of 2.2 l/h (6.7 %) was achieved. The results align with the modules' individual prediction errors. Since the process load model's data is passed to the drivetrain model, the outcome depends heavily on the process load model's prediction error. This can be seen at the 6 cm depth setting at low reference speeds, where the highest errors occur at the same target/reference speed combinations as in the process load model.

Figure 5.15 visualizes the same for the combination of the ANN-based process load model with the drivetrain model.

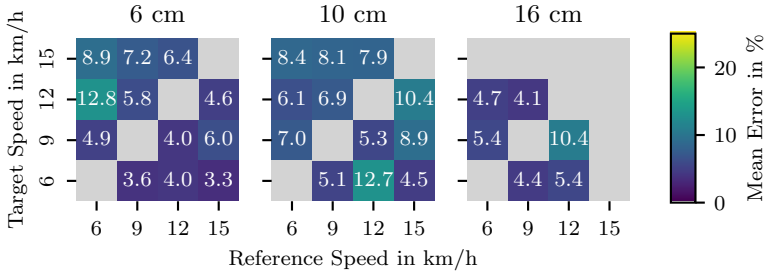

Figure 5.15: ANN model combined with drivetrain model: Fuel rate prediction error for different working depths.

A $\overline{\text{MAE}}$ of 2.2 l/h (6.6 %) was observed. Again, the errors align with those of the process load model used in the first step of the prediction pipeline, as evidenced by the outliers at the 10 cm depth level.

In some cases, the combined model for both process load models yielded a lower average prediction error than the process load model alone. The histograms for the combined model are in the appendix in Chapter A.1.

The data also allows visualization of productivity with respect to energy usage (Equation (3.35)), evaluated in ha/l. Figure 5.16 provides insights into the best operating points, in relation to the driven operating speed. Hereby, it should be noted that the experiments were conducted with the automatic transmission control activated. Efficiency decreases with increasing working depth. This is in line with expectations, as an increase in working depth is accompanied by higher energy requirements and, consequently, greater fuel consumption. At the same time, the most efficient operating point of

the machine combination changes. With increased depth, the lower-speed operating points become more efficient than higher-speed settings.

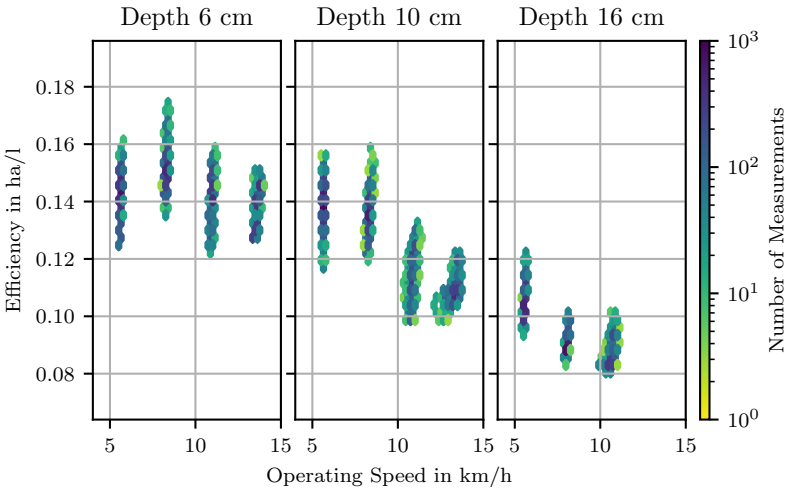

Figure 5.16: Efficiency measurements for different working depths.

At the same time, the overall measured efficiency varies across each lane, which can be attributed to environmental changes during single passes and measurement noise. The highest variation was observed in the low-depth passes at a working depth of 6 cm, with changes of 0.04 ha/l along the lane. Optima that are not addressed by the control strategy's characteristics are not visible in the visualization because, instead of the two degrees of freedom of motor speed and operating speed, the transmission control eliminates the degree of freedom for independent motor speed control.

5.2 Process Load Model Validation

In the following, the results of the process load model validation experiment (Section 4.2.2) are described. To evaluate the prediction model's transferability to other conditions, these experiments were conducted with the Lemken Karat 10 KUA on another tractor, a Fendt 724, at a different location and under

different operating conditions. The field had a steady inclination in driving direction between one and two degrees. Therefore, the evaluation is separated into the two driving directions.

Figure 5.17 visualizes the measured draft forces together with the ASAE D497.7 model.

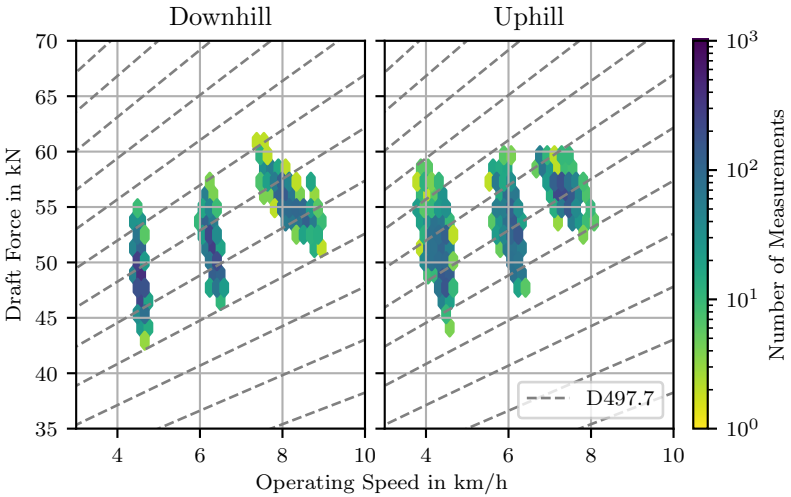

Figure 5.17: Process load model validation: Draft force measurements in comparison to ASAE D497.7.

Although the individual lanes have the same theoretical target speed, the measured operating speeds at the uphill pass are lower than those at the downhill pass due to increased slippage. The maximum speed in the uphill pass is also lower than that in the downhill pass due to the higher force demand, as both reach the tractor's maximum power output.

Due to the constant working depth but the higher inclinations, the evaluation was performed direction-wise. Firstly, the ASAE model was evaluated for the downhill and uphill passes. Figure 5.18 visualizes the results.

The $\overline{\text{MAPE}}$ of 4.7 % and the maximum MAPE of 5.5 % indicate that the process load model is usable across both connected tractors. No patterns are recognizable that were evident in the main experiment. This can be explained by the

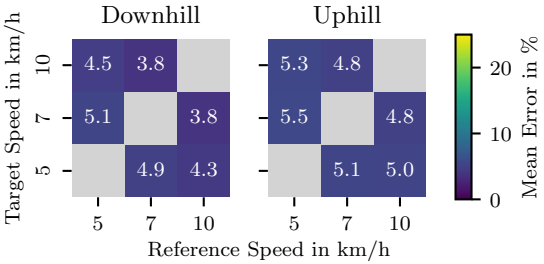

Figure 5.18: ASAE model: Draft force prediction error for different working depths.

deeper working depth and the appearance of error patterns at significantly lower depth levels in the main experiment.

Figure 5.19 visualizes the results of the ANN model. In average, a $\overline{\text{MAPE}}$ of 5.0 % was measured.

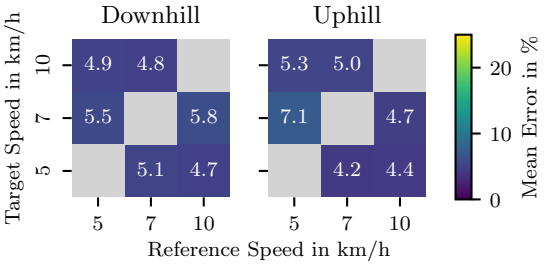

Figure 5.19: ANN model: Draft force prediction error for different working depths.

The highest MAPE of 7.1 % was observed in the uphill pass at a reference speed of 5.0 km/h. This is significantly lower than the maximum MAPE observed in the main experiment, which was 13.3 %.

Compared with the main experiment, both the mean and maximum errors are lower. This suggests that, even though the entire training dataset was recorded in a spatially close setting on the same day, the model can generate valid and generalizable predictions for other situational conditions.

5.3 Drivetrain Model Validation

In the following, the results of the drivetrain model validation experiment (Section 4.2.3) are discussed. Here, as described in Section 4.1.1, the drivetrain model for the Fendt 728, derived and parametrized in the main experiment in combination with a Lemken Karat 10 KUA, is evaluated on data collected with a Köckerling Allrounder 600 to validate the usability in combination with other implements.

Figure 5.20 visualizes the traction measurements of the transferability experiment.

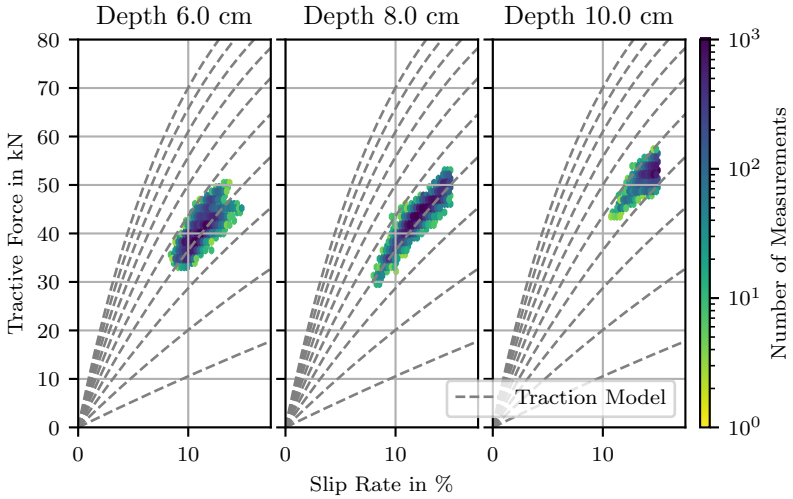

Figure 5.20: Transfer experiments: Traction measurements.

These tests revealed greater variation in traction conditions, reflected in a broader spread of tractive force values for the same slip rates. Here too, the variations in the slip range are comparatively slight, regardless of the selected working depth. Nevertheless, a comparison with the proposed traction model shows that the measured data behaves similarly to the model.

The results of the prediction accuracies of transferability experiments of the drivetrain model are visualized in Figure 5.21. The experiment yields slightly

higher average errors than the main experiment, with an $\overline{\text{MAPE}}$ of 2.9 % as compared to 1.8 %.

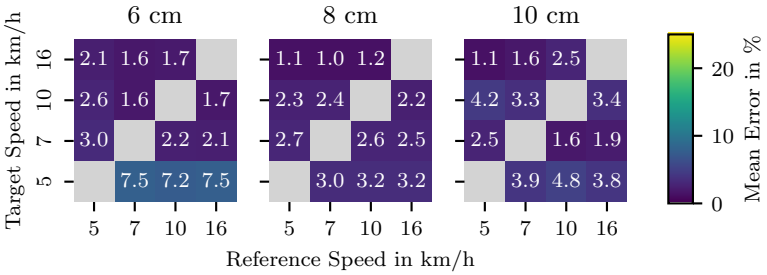

Figure 5.21: Drivetrain model: Fuel rate prediction error for different working depths.

The results for the target speed of 5 km/h performed worse than those for the other target speeds, with an MAPE of 4.9 % compared to 2.2 %. This can be explained by the fact that the training dataset contained only data from theoretical target speeds of 6 km/h or higher. This, together with the lower draft force demand of the light cultivator, means the neural network must extrapolate to lower power demands. From this, it can be concluded that the method's accuracy depends on whether the entire operating range is included in the training dataset. Using data from different locations with varying environmental conditions and process settings during training could improve the neural network's generalizability.

5.4 Impact of Prediction Accuracy on Optimization

The accuracy of the prediction models was analyzed in the previous chapters. Since the predictions serve as a basis for identifying promising operating points, the influence of prediction errors on the optimization is analyzed.

In Figures 5.4, 5.6, and 5.12, no systematic bias was observed in the analysis of the error distributions of the process load model and the powertrain model. The prediction errors were found to be symmetrically distributed, but with a standard deviation of 9.3 % as in the ASAE-based draft model, the scatter of the prediction errors is evident.

For optimization, the gradient of the objective function is the decisive factor. The observable objective functions presented in Chapter 3.3 relate speed, a controllable variable and thus an input parameter of the prediction, to the fuel consumption, an internal variable, and therefore a prediction output. A dispersion of the predicted values, therefore, also leads to a dispersion of the objective function. Given no discernible bias, the optimization process can still converge to the optimal operating point. However, variance in the prediction errors introduces noise into the gradient and therefore delays convergence, but does not prevent the optimization from proceeding.

At shallow working depths, an overestimation of the draft force gradient with regard to changes in operating speed was observed with the ASAE-based draft force model, as in Figures 5.3 and 5.8. This systematic overestimation impairs optimization. However, the gradient sign is correct, as indicated by the overall analysis. Provided that the optimization step size is sufficiently small, this does not prevent optimization.

5.5 Optimization Analysis

In the following, the results of the optimization experiment (Section 4.2.4) are described.

At each optimization iteration, the algorithm predicts the outcome across the entire optimization space, hence all predefined combinations of engine rotations and operating speeds. Figure 5.22 visualizes this in one of the optimization passes at a working depth of 5 cm. For each reference measurement along the lane, the optimization space is evaluated, and the average is computed for each controllable variable combination. To consider the overall efficiency, the representation also includes the area below the minimum speed set by the speed boundary condition. Naturally, by averaging the predictions for each reference measurement along the lane, this illustration assumes constant situational influences. As described in the optimization scheme in Chapter 4.2.4, operating points with predicted fuel rates exceeding the maximum fuel rate in the training dataset are considered invalid and are therefore removed from the illustration.

An efficiency optimum can be observed at approximately 1000 1/min and 4.5 km/h.

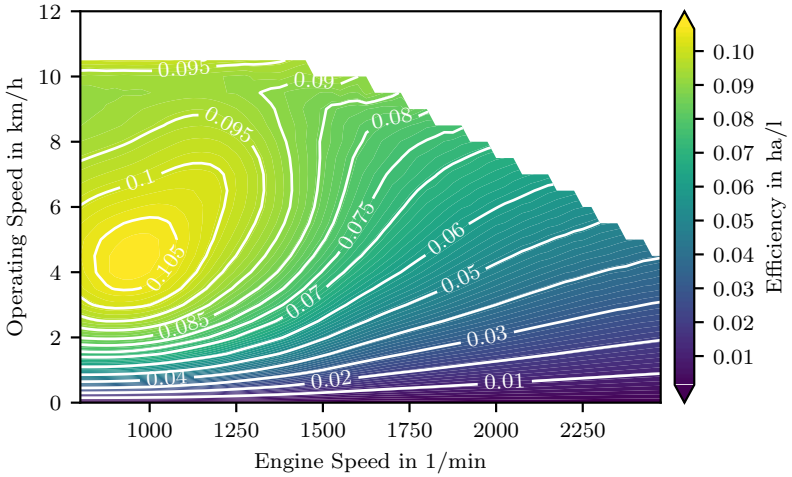

Figure 5.22: Efficiency contour plot for a working depth of 5 cm.

Not all operating points of the characteristic map are included in the training dataset, which was recorded only with the automatic transmission control. This means that in borderline areas, such as when low engine speeds are combined with high operating speeds, the algorithm extrapolates. From a control engineering perspective, not all of the predicted operating points can be reached, as issues relevant to control, such as compliance with the limit force characteristic curve, are not considered.

In the optimization experiments, the algorithm's optimization capabilities were compared with those of various static reference control inputs as described in Figure 4.11. In the following, the results of these experiments are discussed. Here, the average efficiency of the lane driven by the optimizer is compared with that of parallel lanes in proximity with static input settings.

Figure 5.23 visualizes the results of the optimization experiment. In the illustration, each setting is distinguished by color. At a depth of 10 cm, the highest efficiency here occurs at relatively slow speeds. Therefore, the 4.0 km/h lanes were the best of the baselines. However, in the first iteration, the algorithm outperformed all baselines with efficiency increases between 1.3 % to 23.1 %. In the second iteration, the 4 km/h lane achieved the same

efficiency as the algorithm, whereas the result compared to the full-throttle pass was 20.9 %.

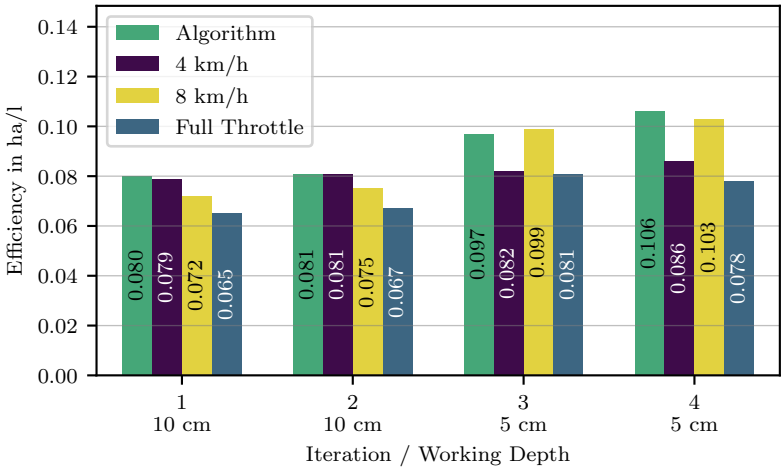

Figure 5.23: Optimization results: Average efficiency of the algorithm compared to static control inputs in parallel lines across four experimental iterations, two with 10 cm working depth and two with 5 cm working depth.

In the shallower depth setting of 5 cm, the overall measured efficiencies are higher than in the deeper setting. This can be explained by the significantly lower draft force demand of the cultivator. However, the efficiency changes heavily depend on the actual setpoint. The reference speed of 4 km/h showed only minor efficiency gains, whereas the 8 km/h pass increased average efficiency by 37 % compared to the deeper depth setting.

The best baselines were the 8.0 km/h lanes, showing that the optimal operating point with the automatic transmission control shifts to higher speeds at shallower depths, which aligns well with the expected decrease in power demand at lower depths. In this setting, the algorithm achieved relative efficiency changes from -2.0 % to 19.8 % and 2.9 % to 35.9 %, respectively. The poorer performance compared to the reference lane of 8.0 km/h can be explained by the optimization limitation due to the requirement for an expected improvement of 3 % before approval of a change in operating point.

Overall, the algorithm increased efficiency by an average of 13.6 % as compared to the reference lanes. During the investigation of the results, it was determined that the algorithm also approaches operating points that an automatic transmission control would avoid. For example, no distance is maintained from the engine's limit force characteristic curve, which could cause the engine to stall. However, this did not occur during the tests and could be avoided by specifying additional limit parameters to prevent unsuitable operating points.

6 Summary

In this work, an approach for adaptively predicting and optimizing possible states of agricultural tractor-implement combinations during operation was developed. The approach extracts information about the machine combination's current situation and predicts possible machine states. Field tests demonstrated the approach's potential to optimize the efficiency of agricultural fieldwork while accounting for constraints imposed by other process targets.

A literature review on the current state of automation in agricultural fieldwork showed that, while much research has been conducted, the main challenge is balancing multiple process objectives, such as quality and efficiency. Without a method for recording the process quality of every step of the production cycle, it is difficult to draw conclusions about the resulting harvest yield. For this reason, holistic optimization of the process is challenging to automate since the overall process objective is not measurable during operation. The proposed approach circumvents this problem by predicting the effects of a control input on the machine state. The prediction model adaptively recognizes the operating situation of the machine combination and incorporates it into the prediction. The algorithm is divided into two parts. First, the process load resulting from the control specification is predicted, and then the tractor's resulting internal state is predicted. As a result, observable productivity indicators can be calculated, leaving it to the operator to decide whether the results are consistent with process targets that cannot yet be monitored. Optimization constraints are introduced to incorporate these decisions into an automatic optimization. Field tests were conducted to evaluate the predictive accuracy of the proposed method. The algorithm's prediction error was determined by driving in parallel lanes, detecting the situation at each point, and predicting the state of directly adjacent points with different control inputs. In separate field tests, the model's transferability to other machine combinations was demonstrated. The proposed automatic optimization approach was elaborated and yielded average efficiency increases of 13.6 %.

6.1 Scientific Contribution

In this chapter, the research questions formulated in Section 2.3 are answered based on the discussed results.

How can the operational state of an agricultural tractor-implement combination be described?

In Section 3.1, the influences on the machine condition were categorized and classified into influences due to changing environmental conditions, process-specific settings such as the configuration of the working tools on the implement, and finally, the controllable parameters with which the machine condition can be actively influenced. A uniform description for the state of agricultural tractor-implement combinations is derived. The description is based on separating process-specific load characteristics from tractor drivetrain characteristics to account for different tractor-implement combinations.

How can the load of an agricultural implement be predicted, considering the interaction with the environment?

Since the load of agricultural implements depends heavily on the interaction with the environment, an approach to parameterize prediction models using spatially close measured points is introduced in Section 3.2. This approach is demonstrated in Section 3.2.1 on the one hand with an approach derived from the ASAE D497.7 standard and, on the other hand, with a purely data-based approach. Experiments were conducted to evaluate the process load models' predictive accuracy, and both models demonstrated their functionality with average prediction errors of 7.2 % and 6.5 %, respectively. In the transferability analysis, the models' usability, transferability, and independence of the connected tractor were verified.

How can artificial neural networks be used to estimate the internal state of a tractor drivetrain based on the load of the attached implements?

In Section 3.2.2, a method was presented to combine a tractor traction model with an artificial neural network to estimate drivetrain characteristics. With this approach, internal machine variables can be calculated from the loads applied by the attached implements. In the experiments, the model's prediction accuracy was determined. An average prediction error of 1.8 % was measured, and the transferability and independence of the connected implement were

verified. The results show that the model accurately predicts the drivetrain's internal state.

How can the operating point of a tractor-implement combination be optimized under agronomic constraints?

The last research question is answered with the constrained optimization approach described in Section 3.3. This approach simplifies the optimization problem by introducing process constraints that prevent negative impacts on harvest yield. In the experiments described in Chapter 4, the optimization approach demonstrated its applicability with an average efficiency improvement of 13.6 %.

By answering the research questions, the research hypothesis

«*The prediction of system states enables optimizing the operating point of an agricultural tractor-implement combination.*»

can be confirmed.

6.2 Continuing Approaches

The approach provides the fundamentals for an assistance system that helps farmers optimize the efficiency of their fieldwork. A next step to improve the prediction accuracy could be the research of more advanced filtering techniques to better detect and estimate the process load demand. More precisely, the detailed handling of the noisy draft force measurements can be mentioned.

The method provides the basis for numerous possible further research activities. One possibility, for example, is to include additional feedback on PTO torque so that implements with different power supplies can also be accounted for, since the approach has only been tested with draft-powered implements.

Furthermore, the included prediction models could be improved. The process load model depends on draft force measurements, which in turn depend on sensor availability and accuracy. The same is true for the traction model in the drivetrain model. Improving sensor availability, for example, by using single-wheel load measurements, could pave the way for a more accurate

representation of the physical machine behavior in the prediction model. Furthmermore, during this work, the extrapolation behavior of the artificial neural networks was identified as a challenge. In the future, this could be improved by deploying physics-based models.

The approach of using neural networks to extract latent representations of the environment's behavior warrants further research. One interesting aspect here would be the analysis of the correlation between the latent variables' values and the measured parameters, such as soil type and moisture. If such a correlation could be verified, the method could be deployed to help farmers understand the characteristic behaviour of their fields.

Further research activities are also possible in the area of combination with automatic process monitoring. Here, for example, the implement could automatically and dynamically report additional optimization constraints to the optimizer. The algorithm currently requires measured values to parameterize the integrated models. Another research approach could be to predict the efficiency of a processing step by forecasting the environment's influence using external data, such as precipitation and soil maps.

A Appendix

This investigation is part of the *EcoAcker* research project. The project is supported by funds of the Federal Ministry of Agriculture, Food and Regional Identity (BMLEH) based on a decision of the Parliament of the Federal Republic of Germany via the Federal Office for Agriculture and Food (BLE) under the research and innovation programme for climate protection in agriculture.

A.1 Figures

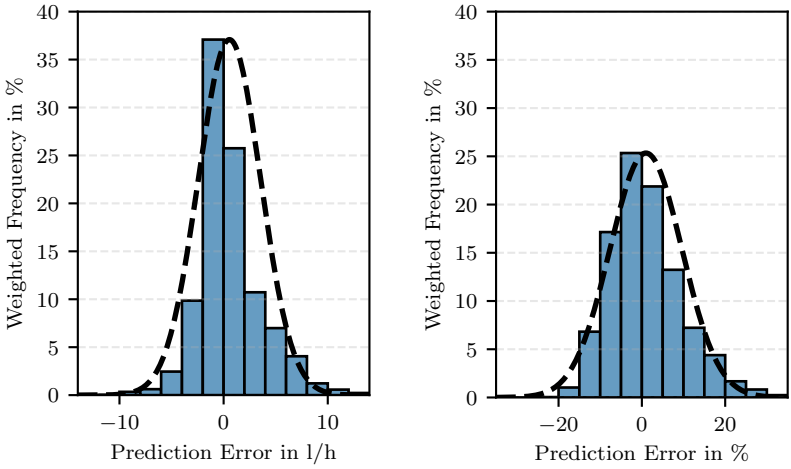

(a) ASAE error distribution.

(b) ASAE percentage error distribution.

Figure A.1: Main experiment: ASAE-based process load model combined with drivetrain model fuel rate prediction error histograms.

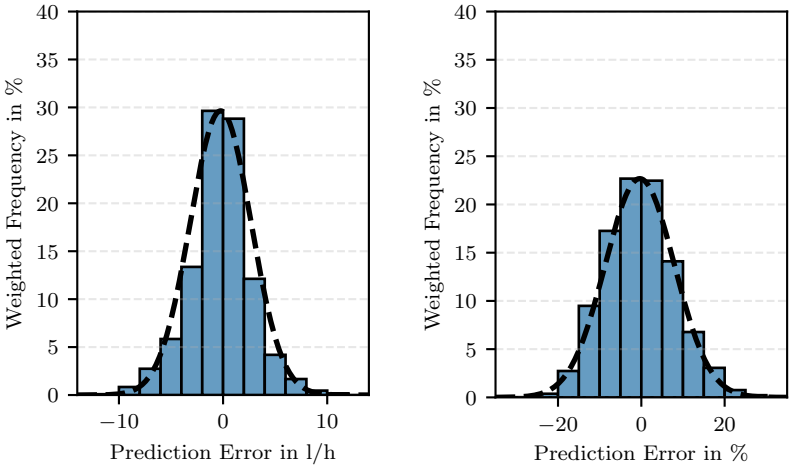

(a) ANN error distribution.

(b) ANN percentage error distribution.

Figure A.2: Main experiment: ANN-based process load model combined with drivetrain model fuel rate prediction error histograms.

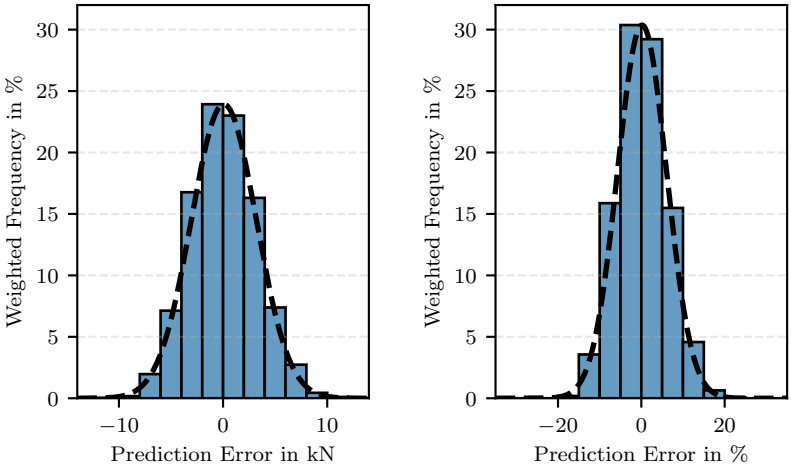

(a) ASAE error distribution.

(b) ASAE percentage error distribution.

Figure A.3: Process load transferability experiment: ASAE model draft force prediction error histograms.

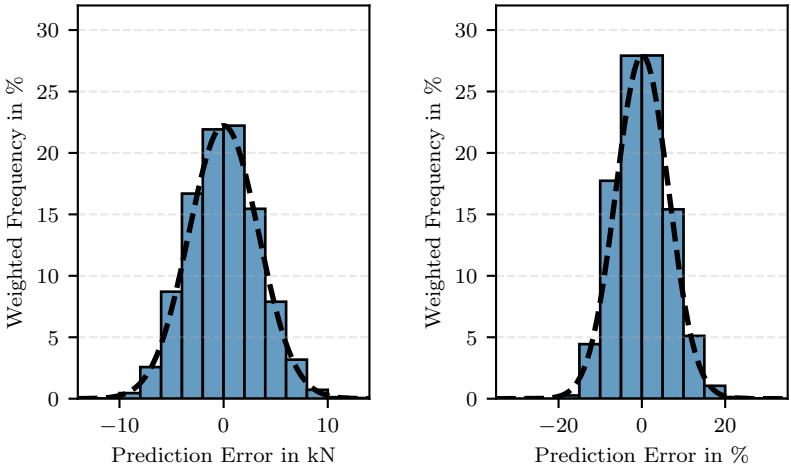

(a) ANN error distribution.

(b) ANN percentage error distribution.

Figure A.4: Process load transferability experiment: ANN model draft force prediction error histograms.

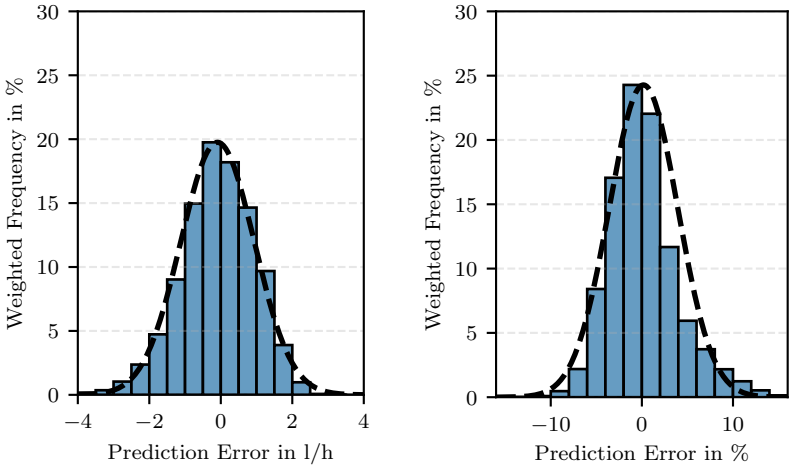

(a) Error distribution.

(b) Percentage error distribution.

Figure A.5: Drivetrain transferability experiment: Fuel rate prediction error histograms.

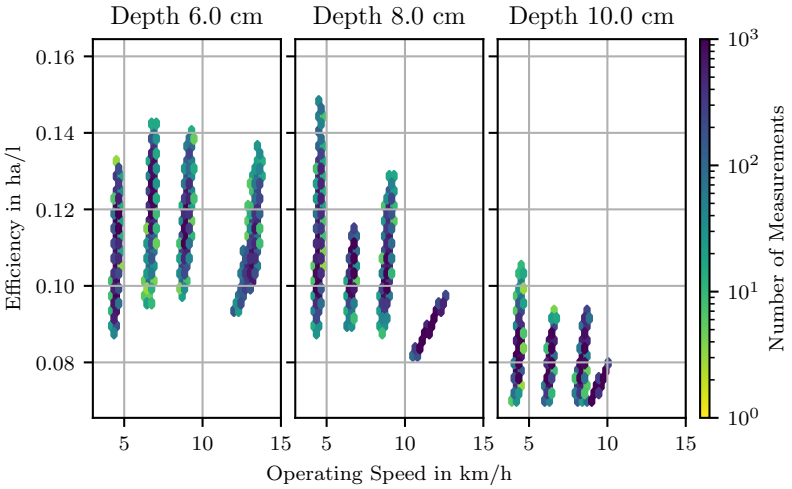

Figure A.6: Efficiency measurements during the drivetrain transferability experiment.

A.2 Tables

In the following, the technical details of the machines used in the experiment are described.

Table A.1: Technical details of the tractors used in the experiments [113], [114].

Manufacturer Model	Fendt 728 Vario Gen7	Fendt 724 Vario Gen6
Model Year	2022	2011
Maximum Power	223 kW	181 kW
Engine Displacement	7527 cm^3	6056 cm^3
Rated Speed	1700 1/min	2100 1/min
Transmission	TA 190	ML 180
Total Width	2650 mm	2550 mm
Total Length	5516 mm	5240 mm
Wheel Distance	2900 mm	2783 mm
Weight (Empty)	8750 kg	7980 kg

Table A.2: Technical details of the implements used in the experiments [115]–[117].

Manufacturer Model	Lemken Karat 10 KUA	Köckerling Allrounder 600
Working Width	4 m	6 m
Weight	4200 kg	4600 kg
Beam Count	3	4
Number of Tines	13	36
Line Distance	31 cm	16.67 cm
Required Power	140-280 PS	180 PS
Mounting Type	Semi-mounted	Semi-mounted

List of Figures

2.1 Illustrations of the forces acting on a tire (inspired by [10], [37]). 12
2.2 Visualization of an artificial neuron (inspired by [60]). . . . 15
2.3 Cross-validation example for five folds (inspired by [63]). . . 18
2.4 Visualization of an autoencoder. 20
2.5 3-layer model for automation of agricultural fieldwork by Schmidt [80]. 23

3.1 Illustration of the state description. 30
3.2 Illustration of the prediction architecture (adapted from [125]). 33
3.3 Clustering of spatially close measurement locations in a field (adapted from [129]). 35
3.4 Schematic representation of the coordinate system definition. 36
3.5 ANN-based architecture for process load prediction (adapted from [129]). 41
3.6 Schematic representation of the drivetrain prediction model. 44
3.7 Visual inspection of the result for fixed working depth of 8 cm and variation of operating speed with a cultivator. 47
3.8 Types of Optimization Constraints. The gray space resembles invalid operating points due to active process constraints, whereas the green space resembles valid ones (adapted from [125]). 48
3.9 Conceptual representation of the optimization procedure. . 50

4.1 Overview of the experiments and corresponding machine combinations. 54
4.2 Primary combination: Fendt 728 with Lemken Karat 10 KUA. 55
4.3 Process load model validation: Fendt 724 with Lemken Karat 10 KUA (adapted from [125]). 55
4.4 Drivetrain model validation: Fendt 728 with Köckerling Allrounder 600. 56

4.5 Visualization of the software setup. 57
4.6 Graphical User Interface (GUI). ① Recording Configuration ② Experiment Configuration ③ System Load Monitoring ④ Node Supervision ⑤ Topic Supervision. 58
4.7 Schematic overview of the main experiment. 62
4.8 Schematic overview of the process load model validation experiment. 63
4.9 Schematic overview of the drivetrain model validation experiment. 64
4.10 Implementation of the optimization approach. 65
4.11 Schematic overview of the optimization experiment. 68
4.12 Overview of the data processing pipeline. 68
4.13 Graphical user interface for data filtering. 69
4.14 Implement location calculation. 71
4.15 Illustration of the ANN-based process load prediction with corresponding variables (adapted from [129]). 72
4.16 Illustration of the drivetrain prediction model with corresponding variables. 75

5.1 Visualization of the prediction accuracy evaluation method. 77
5.2 Evaluation procedure: Each point acts as a reference measurement for predicting the states of the respective closest points in the adjacent lanes. These cross-lane correspondences enable a direct comparison of states recorded under different control inputs. 78
5.3 Draft force measurements in comparison to ASAE D497.7. . 80
5.4 ASAE model: Draft force prediction error histograms. The blue bars visualize the empirical data, and the dashed black line resembles the fitted normal distribution. 81
5.5 ASAE model: Draft force prediction error for different working depths. 83
5.6 ANN model: Draft force prediction error histograms. The blue bars visualize the empirical data, and the dashed black line resembles the fitted normal distribution. 84
5.7 ANN model: Draft force prediction error for different working depths. 84

5.8 Draft force prediction results for the ASAE-model at a working depth of 6 cm. The white boxes resemble the distribution of the prediction targets, whereas the blue boxes resemble the prediction result from the respective reference speed lane. 85
5.9 Draft force prediction results for the ANN-model at a working depth of 6 cm. The white boxes resemble the distribution of the prediction targets, whereas the blue boxes resemble the prediction result from the respective reference speed lane. . 86
5.10 Spatial representation of the latent parameter. Working depths: Top 16 cm, middle 10 cm, bottom 6 cm. 87
5.11 Traction measurements for different working depths. 88
5.12 Drivetrain model: Fuel rate prediction error histograms. The blue bars visualize the empirical data, and the dashed black line resembles the fitted normal distribution. 89
5.13 Drivetrain model: Fuel rate prediction error for different working depths. 90
5.14 ASAE model combined with drivetrain model: Fuel rate prediction error for different working depths. 90
5.15 ANN model combined with drivetrain model: Fuel rate prediction error for different working depths. 91
5.16 Efficiency measurements for different working depths. . . . 92
5.17 Process load model validation: Draft force measurements in comparison to ASAE D497.7. 93
5.18 ASAE model: Draft force prediction error for different working depths. 94
5.19 ANN model: Draft force prediction error for different working depths. 94
5.20 Transfer experiments: Traction measurements. 95
5.21 Drivetrain model: Fuel rate prediction error for different working depths. 96
5.22 Efficiency contour plot for a working depth of 5 cm. 98
5.23 Optimization results: Average efficiency of the algorithm compared to static control inputs in parallel lines across four experimental iterations, two with 10 cm working depth and two with 5 cm working depth. 99

A.1 Main experiment: ASAE-based process load model combined with drivetrain model fuel rate prediction error histograms. 105

A.2 Main experiment: ANN-based process load model combined with drivetrain model fuel rate prediction error histograms. 106
A.3 Process load transferability experiment: ASAE model draft force prediction error histograms. 106
A.4 Process load transferability experiment: ANN model draft force prediction error histograms. 107
A.5 Drivetrain transferability experiment: Fuel rate prediction error histograms. 107
A.6 Efficiency measurements during the drivetrain transferability experiment. 108

List of Tables

2.1 Standardized tractor implement interfaces for power transfer [9], [13]–[15]. 8

3.1 Flow-effort depition of energy exchange [98]. 31
3.2 Interface Measurements on the ISOBUS [22]. 42

4.1 Overview of CAN signals used for data acquisition. 59
4.2 Parameter ranges of the prediction accuracy experiment. . . 61
4.3 Parameter ranges of the process load validation experiment. 63
4.4 Parameter ranges of the drivetrain model validation experiment. 64
4.5 Process load model: Hyperparameter search space. 74
4.6 Drivetrain model: Hyperparameter search space. 76

A.1 Technical details of the tractors used in the experiments [113], [114]. 109
A.2 Technical details of the implements used in the experiments [115]–[117]. 109

Bibliography

[1] Kuratorium für Technik und Bauwesen in der Landwirtschaft e.V. (KTBL), *Faustzahlen für die Landwirtschaft*, 15th ed. Darmstadt: KTBL, 2018, ISBN: 978-3-945088-59-3.

[2] H. Eckel *et al.*, "Verwendung erneuerbarer Antriebsenergien in landwirtschaftlichen Maschinen", Kuratorium für Technik und Bauwesen in der Landwirtschaft e.V. (KTBL), Darmstadt, KTBL Sonderveröffentlichung 12643, 2023.

[3] Europäisches Parlament und Rat der Europäischen Union, *Verordnung (EU) 2021/1119 des Europäischen Parlaments und des Rates vom 30. Juni 2021 zur Schaffung des Rahmens für die Verwirklichung der Klimaneutralität und zur Änderung der Verordnungen (EG) Nr. 401/2009 und (EU) 2018/1999 („Europäisches Klimagesetz")*, Jun. 2021.

[4] Bundesrepublik Deutschland, *Bundes-Klimaschutzgesetz vom 12. Dezember 2019 (BGBl. I S. 2513)*, 2019.

[5] K. Köller and O. Hensel, Eds., *Verfahrenstechnik in der Pflanzenproduktion*, UTB 5198, Stuttgart: Verlag Eugen Ulmer, 2019, ISBN: 978-3-8252-5198-7. DOI: 10.36198/9783838551982.

[6] M. Geimer, R. Stirnimann, and K. Renius, "Motoren und Getriebe bei Traktoren", *Jahrbuch Agrartechnik 2021*, vol. 33, in collab. with Universitätsbibliothek Braunschweig, 2022, Publisher: Institut für Mobile Maschinen und Nutzfahrzeuge. DOI: 10.24355/DBBS.084-202202030943-0.

[7] R. Stirnimann, C. Birkmann, and K. Renius, "Motoren und Getriebe bei Traktoren", *Jahrbuch Agrartechnik 2024*, vol. 36, in collab. with Universitätsbibliothek Braunschweig, 2025, Publisher: Institut für Mobile Maschinen und Nutzfahrzeuge. DOI: 10.24355/DBBS.084-202502071037-0.

[8] R. Stirnimann, K. Renius, and M. Geimer, "Motoren und Getriebe bei Traktoren", *Jahrbuch Agrartechnik 2022*, vol. 33, in collab. with Universitätsbibliothek Braunschweig, 2023, Publisher: Institut für Mobile Maschinen und Nutzfahrzeuge. DOI: 10.24355/DBBS.084-202301130821-0.

[9] K.-T. Renius, *Fundamentals of Tractor Design*. Springer International Publishing, 2020, ISBN: 978-3-030-32803-0. DOI: 10.1007/978-3-030-32804-7.

[10] M. Geimer, *Mobile working machines*. Warrendale, Pennsylvania (USA): SAE International, 2020, ISBN: 978-0-7680-9432-9. DOI: 10.4271/9780768094329.

[11] W. J. Chancellor and N. C. Thai, "Automatic control of tractor transmission ratio and engine speed", *Transactions of the ASAE*, vol. 27, no. 3, pp. 642–646, 1984, ISSN: 2151-0059. DOI: 10.13031/2013.32843.

[12] M. Schrock *et al.*, "A device for aiding gear selection in agricultural tractors", *Transactions of the ASAE*, vol. 29, no. 5, pp. 1232–1236, 1986, ISSN: 2151-0059. DOI: 10.13031/2013.30301.

[13] "Tractors and machinery for agriculture and forestry - electrical high-power interface 700 v DC / 480 v AC part 2: Physical interface", Standard ISO 23316-2, Sep. 2023, Version: 1.

[14] "Agricultural tractors - front-mounted equipment - part 3: Power take-off: General specifications and location", Standard ISO 8759-3, Nov. 2018, Version: 1.

[15] "Agricultural tractors - front-mounted equipment - part 4: Three-point linkage", Standard ISO 8759-4, Nov. 2018, Version: 1.

[16] H. Auernhammer, *Elektronik in Traktoren und Maschinen: Einsatzgebiete, Funktion, Entwicklungstendenzen*, 2., überarb. Aufl. München Wien Zürich: BLV-Verl.-Ges, 1991, ISBN: 978-3-405-14307-7.

[17] "Tractors and machinery for agriculture and forestry — serial control and communications data network part 1: General standard for mobile data communication", Standard ISO 11783-1, Dec. 2017, Version: 2.

[18] A. Munack, *CIGR Handbook of Agricultural Engineering: Information Technology*. American Society of Agricultural Engineers, 2006, ISBN: 1-892769-54-9.

[19] R. Freimann, *Automation mobiler Arbeitsmaschinen: Gerät steuert Traktor* (Fortschrittberichte VDI 14, Landtechnik, Lebensmitteltechnik / Verein Deutscher Ingenieure 116). Düsseldorf: VDI-Verl, 2004, ISBN: 978-3-18-311614-0.

[20] W. Holtmann, "Fahrbericht TIM mit Deutz-Fahr und Krone", *profi*, no. 12, pp. 90–92, Dec. 2021.

[21] F. Berning, "Herstellerverbund 3a: AgXeed, AmazoneAutoTill und claas autonomy", *profi*, no. 10, Oct. 2023.

[22] "ISOBUS data dictionary", [Online]. Available: https://www.isobus.net/ (visited on 07/27/2024).

[23] "AEF ISOBUS database", [Online]. Available: https://www.aef-isobus-database.org/ (visited on 07/27/2024).

[24] "Tractors and machinery for agriculture and forestry — serial control and communications data network part 9: Tractor ECU", Standard ISO 11783-9, Feb. 1, 2012, Version: 2.

[25] E. McKyes, *Soil cutting and tillage* (Developments in agricultural engineering 7). Amsterdam ; New York: Elsevier, 1985, ISBN: 978-0-444-42548-5.

[26] G. Getzlaff, "Vergleichende Untersuchungen über die Kräfte an Normpflugkörpern", *Grundlagen der Landtechnik - Konstrukteurhefte*, vol. 5, 1953.

[27] R. Reich, "Bodenwiderstand und Arbeitseffekt eines Grubberwerkzeugs", *Grundlagen der Landtechnik*, vol. 27, no. 4, 1977, ISSN: 0017-4920.

[28] W. P. Gorjatschkin, *Theorie des Pfluges: Grundlagen zu einer systematischen Berechnung der Pflüge*, 3 vols. Moskau: Industrie-Verlag, 1927.

[29] T. Harrigan and C. Rotz, "Draft relationships for tillage and seeding equipment", *Applied engineering in agriculture*, vol. 11, pp. 773–783, Nov. 1, 1995. DOI: 10.13031/2013.25801.

[30] "Agricultural machinery management data", American Society of Agricultural and Biological Engineers (ASABE), St. Joseph, MI, Standard ASAE D497.7, 2011.

[31] K. Hank and P. Wagner, "Überprüfung und Verwendung von Zugkraftwerten aus der Bodenbearbeitung", in *Land- und Ernährungswirtschaft im Wandel: Aufgaben und Herausforderungen für die Agrar- und Umweltinformatik, Referate der 26. GIL Jahrestagung*, ser. LNI, vol. P-78, Potsdam, Germany: GI, Mar. 2006, pp. 97–100.

[32] B. Schutte, *Bestimmung von Bodenunterschieden durch Zugkraftmessungen bei der Bodenbearbeitung* (Forschungsbericht Agrartechnik des Arbeitskreises Forschung und Lehre der Max-Eyth-Gesellschaft Agrartechnik im VDI (VDI-MEG) 429), Dissertation: Universität Hohenheim. 2005.

[33] B. Schutte and H. D. Kutzbach, "Positionsbezogene Erfassung von Zugkraftwerten", *agricultural engineering.eu*, vol. 58, no. 6, pp. 376–377, Dec. 15, 2003, Number: 6, ISSN: 2943-5641. DOI: 10.15150/lt.2003.1536.

[34] "Agricultural machinery management data", American Society of Agricultural Engineers (ASAE), St. Joseph, MI, USA, Standard ASAE D497.4, 2003.

[35] P. Rößler, T. Kautzmann, and M. Geimer, "Online parametrierbare Traktor-Gerätemodelle", *LANDTECHNIK*, vol. 67, pp. 247–250, Aug. 27, 2012, Number: 4, ISSN: 2700-7898. DOI: 10.15150/lt.2012.303.

[36] T. Bögel, *Identifikation von Form- und Einstellparametern passiver, keilförmiger Arbeitsorgane zur Optimierung der Wechselwirkung von Arbeitsfunktion und Zugkraftbedarf*, Dissertation: TU Dresden. Wiesbaden: Springer Fachmedien Wiesbaden, 2022. DOI: 10.1007/978-3-658-37029-9.

[37] K. T. Renius, *Traktoren: Technik und ihre Anwendung* (Wissen für die Praxis), 2., durchges. Aufl. München: BLV-Verl.-Ges. [u.a.], 1987, 191 pp., ISBN: 978-3-405-13146-3.

[38] M. Schreiber and H. D. Kutzbach, "Comparison of different zero-slip definitions and a proposal to standardize tire traction performance", *Journal of Terramechanics*, vol. 44, no. 1, pp. 75–79, Jan. 1, 2007, ISSN: 0022-4898. DOI: 10.1016/j.jterra.2006.03.003.

[39] H. Pacejka, *Tyre and Vehicle Dynamics*, 2nd ed. Butterworth-Heinemann, 2006, ISBN: 978-0-08-054333-8.

[40] A. Kobelski, P. Osinenko, and S. Streif, "A method of online traction parameter identification and mapping", *IFAC-PapersOnLine*, 21st IFAC World Congress, vol. 53, no. 2, Jan. 1, 2020, ISSN: 2405-8963. DOI: 10.1016/j.ifacol.2020.12.909.

[41] M. Bekker, *Theory of Land Locomotion: The Mechanics of Vehicle Mobility*. University of Michigan Press, 1956.

[42] M. G. Bekker, "Practical aid to off-road tire evaluation with bevameter techniques", *SAE Transactions*, vol. 83, pp. 3395–3401, 1974, Publisher: SAE International, ISSN: 0096-736X.

[43] M. Schreiber and H. Kutzbach, "Influence of soil and tire parameters on traction", *Research in Agricultural Engineering*, vol. 54, Jan. 1, 2008. DOI: 10.17221/3105-RAE.

[44] M. Schreiber, *Kraftstoffverbrauch beim Einsatz von Ackerschleppern im besonderen Hinblick auf die CO2-Emissionen*, Dissertation: Universität Hohenheim. 2006.

[45] A. Meiners, S. Böttinger, and N. Regazzi, "Triebkraft/Schlupf-Verhalten von Ackerschlepperreifen – praxisnahe Messung und Simulation mit dem Hohenheimer Maschinenmodell", *LANDTECHNIK*, Bd. 75 Nr. 1 (2020), Jan. 23, 2020, Publisher: LANDTECHNIK. DOI: 10.15150/LT.2020.3226.

[46] R. D. Wismer and H. J. Luth, "Off-road traction prediction for wheeled vehicles", *Journal of Terramechanics*, vol. 10, no. 2, pp. 49–61, Jan. 1, 1973, ISSN: 0022-4898. DOI: 10.1016/0022-4898(73)90014-1.

[47] "Soil cone penetrometer", American Society of Agricultural and Biological Engineers (ASABE), St. Joseph, MI, USA, Standard ASAE S313.3, 2014.

[48] "Procedures for using and reporting data obtained with the soil cone penetrometer", American Society of Agricultural and Biological Engineers (ASABE), Standard ASAE EP542.1, 2019.

[49] W. Brixius, "Traction prediction equations for bias ply tires", ASAE, St. Joseph, MI, USA, ASAE paper No. 87-1622, 1987.

[50] S. A. Al-Hamed and A. A. Al-Janobi, "A program for predicting tractor performance in visual c++", *Computers and Electronics in Agriculture*, vol. 31, no. 2, pp. 137–149, Apr. 1, 2001, ISSN: 0168-1699. DOI: 10.1016/S0168-1699(00)00177-0.

[51] F. Zoz and R. Grisso, "Traction and tractor performance", *ASAE Distinguish. Ser.*, vol. 27, Tractor Design 2003.

[52] M. J. Dwyer, "Prediction of drawbar test performance", *Journal of Terramechanics*, Special Issue: Terramechanics, mobility and unconventional vehicles, vol. 24, no. 2, pp. 169–177, Jan. 1, 1987, ISSN: 0022-4898. DOI: 10.1016/0022-4898(87)90007-3.

[53] B. Pichlmaier, *Traktionsmanagement für Traktoren*, Dissertation: Technische Universität München. Technische Universität München, 2012.

[54] M. Peeters *et al.*, "Integrated wheel load measurement for tractors", in *Land.Technik AgEng 2017*, VDI Verlag, 2017, pp. 423–430, ISBN: 978-3-18-102300-6. DOI: 10.51202/9783181023006-423.

[55] James H. Taylor *et al.*, "Multipass behavior of a pneumatic tire in tilled soils", *Transactions of the ASAE*, vol. 25, no. 5, pp. 1229–1231, 1982, Number: 5, ISSN: 2151-0059. DOI: 10.13031/2013.33702.

[56] I. Holm, "Multi-pass behaviour of pneumatic tires", *Journal of Terramechanics*, vol. 6, no. 3, pp. 47–71, Jan. 1969, ISSN: 00224898. DOI: 10.1016/0022-4898(69)90128-1.

[57] I. Holm, *Das Verhalten von Reifen beim mehrmaligen Überfahren einer Spur auf nachgiebigem Boden und der Einfluss auf die Konzeption mehrachsiger Fahrzeuge* (Fortschrittberichte der VDI Zeitschriften 14), Dissertation: Technische Universität München. Düsseldorf: VDI Verlag, 1972, vol. 17.

[58] A. Azizi *et al.*, "Classification of soil aggregates: A novel approach based on deep learning", *Soil and Tillage Research*, vol. 199, p. 104 586, May 2020, ISSN: 01671987. DOI: 10.1016/j.still.2020.104586.

[59] S. Kujawa and G. Niedbała, "Artificial neural networks in agriculture", *Agriculture*, vol. 11, no. 6, Jun. 2021, Publisher: Multidisciplinary Digital Publishing Institute (MDPI), ISSN: 2077-0472. DOI: 10.3390/agriculture11060497.

[60] I. N. da Silva *et al.*, *Artificial Neural Networks*. Cham: Springer International Publishing, 2017, ISBN: 978-3-319-43161-1. DOI: 10.1007/978-3-319-43162-8.

[61] R. Rojas, "The backpropagation algorithm", in *Neural Networks*. Berlin, Heidelberg: Springer Berlin Heidelberg, 1996, pp. 149–182, ISBN: 978-3-540-60505-8. DOI: 10.1007/978-3-642-61068-4_7.

[62] I. Goodfellow, Y. Bengio, and A. Courville, *Deep Learning*. The MIT Press, 2016, ISBN: 978-0-262-03561-3.

[63] J. Allgaier and R. Pryss, "Cross-validation visualized: A narrative guide to advanced methods", *Machine Learning and Knowledge Extraction*, vol. 6, no. 2, pp. 1378–1388, Jun. 2024, Publisher: Multidisciplinary Digital Publishing Institute (MDPI), ISSN: 2504-4990. DOI: 10.3390/make6020065.

[64] J. Bergstra and Y. Bengio, "Random search for hyper-parameter optimization", *Journal of Machine Learning Research*, vol. 13, no. 10, pp. 281–305, 2012.

[65] L. Li *et al.*, "Hyperband: A novel bandit-based approach to hyperparameter optimization", *Journal of Machine Learning Research*, vol. 18, no. 185, pp. 1–52, 2018.

[66] H. Fröhlich and A. Zell, "Efficient parameter selection for support vector machines in classification and regression via model-based global optimization", presented at the Proceedings of the International Joint Conference on Neural Networks, vol. 3, Jan. 1, 2005, pp. 1431–1436, ISBN: 978-0-7803-9048-5. DOI: 10.1109/IJCNN.2005.1556085.

[67] A. Géron, *Hands-On Machine Learning with Scikit-Learn and TensorFlow: Concepts, Tools, and Techniques to Build Intelligent Systems*, 1st. O'Reilly Media, Inc., 2017, ISBN: 978-1-4919-6229-9.

[68] M. A. Kramer, "Nonlinear principal component analysis using autoassociative neural networks", *AIChE Journal*, vol. 37, no. 2, pp. 233–243, Feb. 1991, ISSN: 0001-1541, 1547-5905. DOI: 10.1002/aic.690370209.

[69] K. Cho *et al.*, *Learning phrase representations using RNN encoder-decoder for statistical machine translation*, Sep. 3, 2014. DOI: 10.48550/arXiv.1406.1078.

[70] I. Sutskever, O. Vinyals, and Q. V. Le, *Sequence to sequence learning with neural networks*, Dec. 14, 2014. DOI: 10.48550/arXiv.1409.3215.

[71] I. D. Mienye and T. G. Swart, "Deep autoencoder neural networks: A comprehensive review and new perspectives", *Archives of Computational Methods in Engineering*, Mar. 15, 2025, ISSN: 1886-1784. DOI: 10.1007/s11831-025-10260-5.

[72] I. C. Ays, *Development of a CO2e quantification method and of solutions for reducing the greenhouse gas emissions of construction machines* (Karlsruher Schriftenreihe Fahrzeugsystemtechnik), Dissertation: Karlsruher Institut für Technologie. KIT Scientific Publishing, 2021, vol. 87, ISBN: 978-3-7315-1033-8. DOI: 10.5445/KSP/1000118868.

[73] H. Wilmer, "Reifendruck-verstellanlagen im vergleich", *profi*, no. 3, pp. 14–27, Mar. 2022.

[74] S. Zikeli and S. Gruber, "Reduced tillage and no-till in organic farming systems, germany—status quo, potentials and challenges", *Agriculture*, vol. 7, no. 4, p. 35, Apr. 2017, Number: 4 Publisher: Multidisciplinary Digital Publishing Institute, ISSN: 2077-0472. DOI: 10.3390/agriculture7040035.

[75] M. Werling, *Optimale aktive Fahreingriffe: für Sicherheits- und Komfortsysteme in Fahrzeugen*. De Gruyter Oldenbourg, Jul. 24, 2017, ISBN: 978-3-11-053192-3. DOI: 10.1515/9783110531923.

[76] E. Donges, "Fahrerverhaltensmodelle", in *Handbuch Fahrerassistenzsysteme: Grundlagen, Komponenten und Systeme für aktive Sicherheit und Komfort*, H. Winner, S. Hakuli, and G. Wolf, Eds., Wiesbaden: Vieweg+Teubner, 2009, pp. 15–23, ISBN: 978-3-8348-9977-4. DOI: 10.1007/978-3-8348-9977-4_3.

[77] SAE International, "Taxonomy and definitions for terms related to driving automation systems for on-road motor vehicles", SAE International, SAE Recommended Practice J3016_202104, Apr. 2021.

[78] N. Streitberger, F. Balbach, and E. Nacke, "Vom manuellen Fahren zur vollen Autonomie: Ein Ansatz zur systematischen Definition verschiedener Stufen der Automation in der Landtechnik", presented at the Land.Technik 2018, ser. VDI-Berichte, vol. 2332, Leinfelden-Echterdingen: VDI Verlag GmbH, 2018, pp. 213–221, ISBN: 978-3-18-092332-1.

[79] M. Schmidt, *Maschinelle Beurteilung agronomischer Arbeitsqualität als Grundlage für die Verhaltensgenerierung automatisierter Landmaschinen* (Forschungsbericht Agrartechnik des Fachausschusses Forschung und Lehre der Max-Eyth-Gesellschaft Agrartechnik im VDI (VDI-MEG) 630), Dissertation: Technische Universität Berlin. Düren: Shaker Verlag, 2023, 239 pp., ISBN: 978-3-8440-8945-5.

[80] M. Schmidt, "Description of the operator's tasks with a tractor-implement combination as a basis for further automation developments in agricultural engineering", *LANDTECHNIK*, Bd. 75 Nr. 3 (2020), Sep. 16, 2020, Publisher: LANDTECHNIK. DOI: 10.15150/LT.2020.3243.

[81] K. Möller and W. Schultze, Eds., *Produktivität von Dienstleistungen*, Wiesbaden: Springer Fachmedien Wiesbaden, 2014, ISBN: 978-3-658-04085-7. DOI: 10.1007/978-3-658-04086-4.

[82] P. G. D. Scherer, "Methodik zur Bewertung der Energieeffizienz von mobilen Arbeitsmaschinen", Dissertation, Karlsruher Institut für Technologie, Karlsruhe, 2017. DOI: 10.5445/IR/1000066047.

[83] P. Riegler-Nurscher *et al.*, "A system for online control of a rotary harrow using soil roughness detection based on stereo vision", presented at the AgEng 2017, 2017.

[84] P. Riegler-Nurscher, "Mobile vision system for estimation of soil and plant properties", Dissertation, Technische Universität Wien, 2021. DOI: 10.34726/hss.2021.85680.

[85] A. Meiners, *Potentialbewertung effizienzsteigernder Technologien bei Landmaschinen in Verfahrensketten mit Körnerfruchternte* (Forschungsbericht Agrartechnik des Arbeitskreises Forschung und Lehre der Max-Eyth-Gesellschaft Agrartechnik im VDI (VDI-MEG) 632), Dissertation: Universität Hohenheim. Düren: Shaker Verlag, 2023, ISBN: 978-3-8440-9030-7.

[86] S. Denker and L. Volk, "Dieseleffizienz in der Landwirtschaft", *LANDTECHNIK*, vol. 62, no. 4, pp. 220–221, Aug. 27, 2007, ISSN: 2700-7898. DOI: 10.15150/lt.2007.987.

[87] "DLG Prüfbericht CEMOS TRAKTOR (Softwareversion 6.12.6 vom 1. Mai 2020)", DLG TestService GmbH, Groß-Umstadt, Prüfbericht 7096, 2020.

[88] B. Li *et al.*, "Automatic gear-shifting strategy for fuel saving by tractors based on real-time identification of draught force characteristics", *Biosystems Engineering*, vol. 193, pp. 46–61, May 1, 2020, ISSN: 1537-5110. DOI: 10.1016/j.biosystemseng.2020.02.008.

[89] T. Kautzmann *et al.*, "Holistic optimization of tractor management organic computing in off-highway machines", presented at the LANDTECHNIK AgEng, 2011, pp. 275–280.

[90] O. Degrell and T. Feuerstein, ""DLG-PowerMixTM" - Ein praxisorientierter Traktorentest", presented at the Tagung Landtechnik 2003, ser. VDI Berichte, vol. 1798, Hannover: VDI Verlag GmbH, 2003, pp. 339–345, ISBN: 3-18-091798-9.

[91] T. Kautzmann and M. Geimer, "A novel approach for holistic optimization of mobile machine managements", *Proceedings of the 12th Scandinavian International Conference on Fluid Power (SICFP'11), Tampere, Finland, May 18-20, 2011*, 2011, ISBN: 9789521525179.

[92] T. Kautzmann, *Die mobile Arbeitsmaschine als komplexes System* (Karlsruher Schriftenreihe Fahrzeugsystemtechnik), Dissertation: Karlsruher Institut für Technologie. Karlsruhe: KIT Scientific Publishing, 2013, vol. 23, ISBN: 978-3-7315-0187-9. DOI: 10.5445/KSP/1000039390.

[93] S. Becker *et al.*, "Machine Learning for Process Automation of Mobile Machines in Field Applications", in *Land.Technik AgEng 2019 : Hannover, Nov. 8th + 9th 2019 : 77th International Conference on Agricultural Engineering*, ISSN: 0083-5560, 2019, ISBN: 978-3-18-092361-1.

[94] J. Boysen, L. Zender, and A. Stein, "Modeling the soil-machine response of secondary tillage: A deep learning approach", *Smart Agricultural Technology*, vol. 6, Dec. 1, 2023, ISSN: 2772-3755. DOI: 10.1016/j.atech.2023.100363.

[95] J. Boysen, S. Bökle, and A. Stein, "AI-assisted tractor control for secondary tillage", *Smart Agricultural Technology*, vol. 12, Dec. 1, 2025, ISSN: 2772-3755. DOI: 10.1016/j.atech.2025.101294.

[96] S. Steinhaus, *Methodik zur Bewertung und Erfassung der Effektivität und Effizienz von landwirtschaftlichen Verfahren und Prozessen* (Forschungsberichte aus dem Institut für mobile Maschinen und Nutzfahrzeuge), Dissertation: Technische Universität Braunschweig. Düren: Shaker Verlag, 2022, ISBN: 978-3-8440-8421-4.

[97] S. Steinhaus and L. Frerichs, "A novel approach to determine the soil aggregate size distribution from high-resolution 3d point clouds", presented at the LAND.TECHNIK 2020, ser. VDI Berichte, vol. 2374, VDI Wissensforum GmbH, 2020, pp. 361–368, ISBN: 978-3-18-102374-7. DOI: 10.51202/9783181023747-361.

[98] R. Isermann, *Mechatronische Systeme*. Berlin, Heidelberg: Springer Berlin Heidelberg, 2008, ISBN: 978-3-540-32336-5. DOI: 10.1007/978-3-540-32512-3.

[99] BRIDGESTONE EUROPE NV/SA. "Haben Ihre Traktorreifen den idealen Schlupf?", [Online]. Available: https://www.bridgestone-agriculture.de/haben-ihre-traktorreifen-den-idealen-schlupf (visited on 06/11/2025).

[100] BRIDGESTONE EUROPE NV/SA. "Sie möchten alles über Schlupf bei Traktorreifen wissen?", [Online]. Available: https://www.firestone-agriculture.de/blog/sie-m%C3%B6chten-alles-%C3%BCber-schlupf-bei-traktorreifen-wissen (visited on 06/11/2025).

[101] Michelin Suisse SA. "Verbesserung der Traktion und Auswahl der geeigneten Traktorreifen", [Online]. Available: https://business.michelin.ch/de/hilfe-ratgeber/landmaschinen/reifenwahl-verbesserung-traktion (visited on 06/11/2025).

[102] Maxam Tire. "MAXAM TIRE ON OPTIMIZED TRACTION IN AG APPLICATIONS", [Online]. Available: https://maxamtire.com/maxam-tire-on-optimized-traction-in-ag-applications/ (visited on 06/12/2025).

[103] DLG TestService GmbH, "DLG test report MAXAM AGRIXTRA XL", DLG TestService GmbH, Groß-Umstadt, DLG Test Report 7491, 2024.

[104] J. R. R. A. Martins and A. Ning, *Engineering Design Optimization*, 1st ed. Cambridge University Press, Nov. 18, 2021, ISBN: 978-1-108-98064-7. DOI: 10.1017/9781108980647.

[105] *Verrechnungssätze für Baden-Württemberg 2019-2020*, 27th ed. Maschinenring Baden-Württemberg, Jan. 2019.

[106] AGCO GmbH. "Fendt 700 Vario Gen 7 Broschüre", [Online]. Available: https://dam.agcocorp.com/content/dam/multisite/fendt/marketing/multi-region/documents/marketing-material/brochures/tractors/700-vario-gen7/de/Fendt700VarioGen7_DE_web.pdf (visited on 11/24/2025).

[107] Y. Maruyama, S. Kato, and T. Azumi, "Exploring the performance of ROS2", in *Proceedings of the 13th International Conference on Embedded Software*, ser. EMSOFT '16, New York, NY, USA: Association for Computing Machinery, Oct. 1, 2016, pp. 1–10, ISBN: 978-1-4503-4485-2. DOI: 10.1145/2968478.2968502.

[108] S. Macenski *et al.*, "Robot operating system 2: Design, architecture, and uses in the wild", *Science Robotics*, vol. 7, no. 66, 2022. DOI: 10.1126/scirobotics.abm6074.

[109] J. P. Snyder, "Map projections: A working manual", U.S. Government Printing Office, 1395, 1987, ISSN: 2330-7102 Publication Title: Professional Paper. DOI: 10.3133/pp1395.

[110] Bokeh Development Team, *Bokeh: Python library for interactive visualization*, 2018.

[111] C. D. Manning, P. Raghavan, and H. Schütze, *An Introduction to Information Retrieval*. Cambridge: Cambridge University Press, 2008, ISBN: 978-0-521-86571-5.

[112] Y. Dodge, *The Concise Encyclopedia of Statistics*. New York: Springer-Verlag, 2008, ISBN: 978-0-387-31742-7.

[113] AGCO GmbH. "Fendt 700 Vario Gen6 | Technische Daten", [Online]. Available: https://api.fendt.com/techdata/DE/de/1153736/Fendt-700-Vario-Gen6 (visited on 06/02/2025).

[114] AGCO GmbH. "Fendt 700 Vario Gen7 | Technische Daten", [Online]. Available: https://api.fendt.com/techdata/DE/de/1152593/Fendt-700-Vario-Gen7 (visited on 06/02/2025).

[115] LEMKEN GmbH & Co. KG. "Broschüre Intensiv-Grubber Karat 10", [Online]. Available: https://lemken.com/fileadmin/a_Webseite/00_Produkte/_Prospekte/De/Karat_10u12_de.pdf.

[116] LEMKEN GmbH & Co. KG. "Intensivgrubber Karat 10", [Online]. Available: https://lemken.com/de-de/landmaschinen/bodenbearbeitung/stoppelbearbeitung/karat-10 (visited on 06/02/2025).

[117] Landmaschinenfabrik Köckerling GmbH & Co. KG. "Broschüre Allrounder -profiline- 600/750", [Online]. Available: https://www.koeckerling.de/fileadmin/container_elements/pdf/deutsch/prospekte/Bodenbearbeitung/Grubber/Allrounder_profiline_600_750/1170_Allrounder_profiline_DE.pdf (visited on 06/02/2025).

Own Publications

[118] S. Becker, B. Kazenwadel, and M. Geimer, "Automation and optimization of working speed and depth in agricultural soil tillage with a model predictive control based on machine learning", presented at the LANDTECHNIK 2022, ser. VDI-Berichte, vol. 2395, Online: VDI Verlag, Feb. 2022, pp. 55–64, ISBN: 978-3-18-092395-6.

[119] L. Michiels *et al.*, "Real-time localization for mobile machines by fusing barometric altitude measurements with surface profiles", in *25th International Conference on Information Fusion (FUSION)*, Linköping, Sweden: IEEE, Jul. 2022, ISBN: 978-1-7377497-2-1. DOI: 10.23919/FUSION49751.2022.9841393.

[120] B. Kazenwadel, S. Becker, and M. Geimer, "Measurement Data Recording and Preprocessing for Training Data Generation using ROS", in *8th International Conference on Machine Control & Guidance, Online, 17th-18th November 2022.*, Nov. 2022, ISBN: 978-83-7493-234-9. DOI: 10.37190/MCG2022.

[121] B. Kazenwadel and M. Geimer, "Real-Time Prediction of Efficient Operating Points in Quasi-Stationary Agricultural Processes with Hydraulic Implements", presented at the ASME/BATH Symposium on Fluid Power and Motion Control (FPMC 2023), Sarasota, FL, USA, Oct. 2023. DOI: 10.1115/FPMC2023-111383.

[122] B. Kazenwadel *et al.*, "Aligning process quality and efficiency in agricultural soil tillage", *at - Automatisierungstechnik*, vol. 71, no. 11, pp. 979–986, Nov. 2023, Publisher: De Gruyter, ISSN: 2196-677X. DOI: 10.1515/auto-2023-0042.

[123] B. Kazenwadel *et al.*, "Data-driven algorithms for predicting energy-efficient operating points in agricultural soil tillage", in *Land.Technik AgEng 2023*, ISSN: 0083-5560, Nov. 2023, pp. 519–528, ISBN: 978-3-18-092427-4. DOI: 10.51202/9783181024270.

[124] L. Michiels *et al.*, *MobimaSkidRoads Dataset*, 2023. DOI: 10.35097/1750.

[125] B. Kazenwadel *et al.*, "Operating point optimization of agricultural tractor–implement combinations as constraint optimization problem", *Eng*, vol. 6, no. 2, Feb. 2025, Publisher: Multidisciplinary Digital Publishing Institute (MDPI), ISSN: 2673-4117. DOI: 10.3390/eng6020027.

[126] Z. Wang *et al.*, "LiDAR-based tree detection and parameterization for SLAM in autonomous forestry machinery", in *2025 5th International Conference on Computer, Control and Robotics (ICCCR)*, May 2025. DOI: 10.1109/ICCCR65461.2025.11072654.

[127] N. Bargen-Herzog *et al.*, "Parametrierung eines Halmstrukturmodells für Miscanthus anhand von 4-Punkt-Biegeversuchen", *agricultural-engineering.eu*, vol. 80, no. 4, Oct. 2025, ISSN: 2943-5641. DOI: 10.15150/ae.2025.3343.

[128] M. Graf *et al.*, “Image-based measurement of aggregate size distribution using machine learning algorithms”, in *2025 IEEE Conference on AgriFood Electronics (CAFE)*, Montevideo, Uruguay: IEEE, Oct. 2025, pp. 1–5, ISBN: 979-8-3315-8892-2. DOI: 10.1109/CAFE66884.2025.11547643.

[129] B. Kazenwadel, M. Graf, and M. Geimer, “Adaptive machine modeling using neural networks to encode spatially correlated measurements”, in *2025 IEEE Conference on AgriFood Electronics (CAFE)*, Montevideo, Uruguay: IEEE, Oct. 2025, pp. 1–5, ISBN: 979-8-3315-8892-2. DOI: 10.1109/CAFE66884.2025.11547583.